

Foreign  
Broadcast  
Information  
Service



A N N I V E R S A R Y  
1 9 4 1 - 1 9 9 1

# ***JPRS Report***

# **Science & Technology**

***China***

19980203 303

DISTRIBUTION STATEMENT A

Approved for public release;  
Distribution Unlimited

DMIC QUALITY INSPECTED 2

REPRODUCED BY  
U.S. DEPARTMENT OF COMMERCE  
NATIONAL TECHNICAL  
INFORMATION SERVICE  
SPRINGFIELD, VA 22161

# Science & Technology China

JPRS-CST-91-021

## CONTENTS

22 October 1991

### AEROSPACE

Preliminary Study of Rocket-Ramjet-Rocket Concept for HTOL Space Plane [Wang Shusheng; YUHAN XUEBAO, No 3, Jul 91] .....	1
Additional Details on Aircraft-Engine High-Altitude Simulation Test Station [HANGKONG ZHISHI, No 7, Jul 91] .....	6
Satellite Reentry and Recovery [Lu Zhangfu; SHIJIE DAODAN YU HANGTIAN, No 6, Jun 91] .....	7

### ADVANCED MATERIALS

Advanced Graphite Composite Fabricated, Analyzed, Compared with German Product [Zhang Zhiqian, Chen Erlong, et al.; HARBIN GONGYE DAXUE XUEBAO, Jun 91] .....	11
High-Temperature Silicon-Nitride Ceramic Developed [Jia Baoliang; JIEFANG RIBAO, 20 Jul 91] .....	15

### COMPUTERS

Fujian Public Security Officials Distribute New MPS-Developed Anti-Computer-Virus Software [Huang Shichi; FUJIAN RIBAO, 6 Sep 91] .....	16
Neural-Net-Based Handwritten-Chinese-Character Recognition System Certified [Han Yun, Ge Cuiping; JISUANJI SHIJIE, 7 Aug 91] .....	16
Sida-863A Spoken-Word Recognition System Unveiled [Du Yachun; JISUANJI SHIJIE, 21 Aug 91] ....	16
Fiber-Optic Computer Network Built at Yumen Oil Field [Chen Nan; JISUANJI SHIJIE, 21 Aug 91] ..	16
Petroleum Institute Computing Center Gets Convex C120 Minisupercomputer [Yun Hai; JISUANJI SHIJIE, 4 Sep 91] .....	17

### FACTORY AUTOMATION, ROBOTICS

New Flexible Manufacturing Cell Developed [KEJI RIBAO, 24 Aug 91] .....	18
---	----

### LASERS, SENSORS, OPTICS

Ganbala Radar Station Built by Air Force Unit [You Cheng; SICHUAN RIBAO, 18 Jun 91] .....	19
Airborne SAR Remote Sensing System Used To Survey Flood Damage [Yue Ziqiang; KEJI RIBAO, 30 Jul 91] .....	19
33fs Pulse Generation Via Mixed Dye Saturable Absorber [Lin Weizhu, Qiu Zhiren, et al.; ZHONGGUO JIGUANG, No 7, Jul 91] .....	19
First Fully Mobile, High-Accuracy CW Tracking Radar System Unveiled [Wang Junhong; ZHONGGUO DIANZI BAO, 2 Aug 91] .....	20
Central China University Develops 10kW-Class CO <sub>2</sub> Laser [ZHONGGUO DIANZI BAO, 4 Aug 91] .....	20
Radar-Oriented Bulk Acoustic Wave Delay Line Developed [ZHONGGUO DIANZI BAO, 4 Aug 91] ...	20
300,000-Pixel Frame-Transfer CCD System Unveiled [Yang Yasheng; ZHONGGUO DIANZI BAO, 11 Aug 91] .....	20
Dual-Wavelength Nd:YAL Laser Unveiled [Yang Yongtian, Yang Zhaoliang; ZHONGGUO KEXUE BAO, 30 Aug 91] .....	22
Shanghai Scientist Develops State-of-the-Art Liquid-Crystal Light Valve [ZHONGGUO JISHU SHICHANG BAO, 4 Sep 91] .....	22
Stimulated Raman Scattering in Single-Mode Fiber and the Walkoff Between Pumping and Raman-Stokes Pulses [Fan Liming, Wang Shijie, et al.; GUANGXUE XUEBAO, Jun 91] .....	23
Coming Ten Years of Environmental Remote Sensing in China [Chen Shupeng; HUANJING YAOGAN, No 3, Aug 91] .....	27

## MICROELECTRONICS

CAS Optoelectronics Institute Develops Chip-Fabrication Optical Equipment [Deng Xianchun, Zheng Tianfen; KEJI RIBAO, 5 Aug 91]	29
Silicon-Gate CMOS PLL Frequency-Synthesizer IC Developed [Yao Jingping; ZHONGGUO DIANZI BAO, 11 Aug 91]	29
Motorola To Invest \$200-400 Million in Tianjin in Next Decade [JISUANJI SHIJIE, 14 Aug 91]	29
Electroluminescent Flat Panel Display Developed [Jia Jinlin; ZHONGGUO KEXUE BAO, 27 Aug 91]	29
Status of IC R&D Described [Wang Yangyuan; ZHONGGUO DIANZI BAO, 6 Sep 91]	29

## SUPERCONDUCTIVITY

R&D of High-Tc Superconducting Devices [Zhou Lian; WULI, No 6, Jun 91]	31
Deposition of Superconducting Nb Films, Preparation of Nb/Al-AlO <sub>x</sub> /Nb Josephson Junctions [Xu Jianhong, Cai Anjiang, et al.; DIWEN YU CHAODAO, No 2, May 91]	31
Study of RF SQUIDS at Liquid-Nitrogen Temperature [Zhang Chaoping, Wang Haiyan, et al.; DIWEN YU CHAODAO, No 2, May 91]	35

## TELECOMMUNICATIONS R&D

Reports on Fiber Optic Communications	41
Shanghai Gets First State-of-the-Art Optical Cable Production Line [Zhang Zhiyuan; JIEFANG RIBAO, 27 Jul 91]	41
Shanghai Institutes Develop Fiber Packing Jelly [JIEFANG RIBAO, 31 Jul 91]	41
Fiber-Optic-Cable, DMW, ISDN Projects Described [Wang Hanlin; KEJI RIBAO, 27 Aug 91]	41
Nanjing-Wuhan Line Formally Operational [Xin You; JISUANJI SHIJIE, 4 Sep 91]	41
Construction Begun on Xian Domestic Satcom Earth Station [Zhou Zhengqing; SHAANXI RIBAO, 30 Jul 91]	42
ISDN Digital/Analog Transmission System Developed [ZHONGGUO DIANZI BAO, 2 Aug 91]	42
Shandong Imports Digital Transmission System From Germany's SEL [Yu Yu; ZHONGGUO DIANZI BAO, 9 Aug 91]	43
HDTV Included in MMEI's 10-Year R&D Goals for TV Industry [Xie Shixin; JINGJI RIBAO, 26 Aug 91]	43
Jiangsu Long-Distance Telephone Network's First High-Capacity DMW Trunkline Operational [Jin Yuqi; DIANXIN JISHU, No 8, Aug 91]	43
Survey of Domestic Public Packet-Switching Networks [Gao Xingzhong; JISUANJI SHIJIE, 10 Jul 91]	43
Fast Acquisition of Inbound Signal Under Low Signal-to-Noise Ratio Condition in RDSS System [Ye Fei, Lu Wenfu; ZHONGGUO KONGJIAN KEXUE JISHU, No 3, Jun 91]	49

## PHYSICS

Lanzhou Heavy-Ion Accelerator Physics Experiments Terminals Certified [Song Wenjie; LANZHOU KEJI QINGBAO, No 1, Feb 91]	50
Design Calculations for Improved ECR Ion Source [Xu Yongxing, Liu Zhanwen, et al.; GAONENG WULI YU HE WULI, No 4, Apr 91]	50
Experimental Terminal of Large Area Ionization Chamber at HIRFL Accelerator [Feng Enpu, Zhu Yongtai, et al.; GAONENG WULI YU HE WULI, May 91]	54

## **Preliminary Study of Rocket-Ramjet-Rocket Concept for HTOL Space Plane**

91FE0821B Beijing YUHAN XUEBAO [JOURNAL OF CHINESE SOCIETY OF ASTRONAUTICS] in Chinese No 3, Jul 91 pp 1-7

[Article by Wang Shusheng [3769 2885 5116] of the Third Research Academy, Ministry of Aerospace Industry [MAS]: "Preliminary Study of Rocket-Ramjet-Rocket Concept for HTOL Space Planes"; MS received 25 Dec 90]

[Text]

### **Abstract**

A rocket-ramjet-rocket concept for HTOL/TSTO space plane is introduced. The discussion focuses on the feasibility of the concept and on the propulsion system which has incorporated two key technologies: early ignition and high-altitude oxygen replenishment. Based on the optimized design of the propulsion system, the configuration and dimensions of the space plane and its flight trajectory are presented. The payload ratio obtained from mass calculations is shown to be comparable to state-of-the-art standards.

### **I. Introduction**

Considerable research and development work has been done in the area of HTOL (Horizontal Take-Off and Landing) space-plane design. It is generally agreed that the key technology for a HTOL space plane is the propulsion system. While single stage to orbit (SSTO) is an attractive concept for space-plane design, its implementation requires the development of advanced propulsion systems such as supersonic-combustion ramjet engines and liquefied air circulation systems. The development cost of these systems is very high because they require large and expensive ground test equipment. In order to avoid development difficulties and reduce technical risk, the two stage to orbit (TSTO) design has been proposed as a more practical concept for space planes. A promising propulsion system for the TSTO design is the air turbine ramjet (ATR) engine, but the working medium for the turbine has not been specified. Because of the conflicting design requirements between thrust-to-weight ratio and specific impulse of the engine, it is difficult to achieve good overall engine performance, and the technical risk is high. Although the turbine-ramjet design is a feasible concept, it requires very high thrust-to-weight ratio for the turbine or the turbofan engine; also, matching the mass flow with that of the ramjet engine would be difficult. In 1987, this author led a small research group in a study of the concept of a TSTO space plane. The study shows that the ramjet engine has certain distinct advantages in terms of resolving the conflicting requirements between specific impulse and thrust-to-weight ratio; on the basis of this study, a rocket-ramjet-rocket design concept was proposed. The first stage of this design is a liquid-hydrogen

ramjet engine. A hydrogen-oxygen-hydrocarbon liquid-propellant rocket booster is used to lift the first stage off the ground; the operating time of the booster engine is kept as short as possible in order to extend the cruise Mach-number range of the ramjet engine. The second stage is a liquid-hydrogen/liquid-oxygen engine which injects the space plane into orbit. It is called a rocket-ramjet-rocket space-plane design because it involves sequential operation of the rocket engine, the ramjet engine and the rocket engine.

### **II. Special Features of the Rocket-Ramjet-Rocket Propulsion System**

The second stage of the rocket-ramjet-rocket propulsion system uses a technically mature hydrogen-oxygen rocket engine which is used by all TSTO space planes. The key technology of this propulsion system is the first stage, which uses both rocket engine and ramjet engine. The main advantage of this design is that it is structurally quite simple because the two engines are independently assembled with no direct structural ties; also, aerodynamic effects must be considered only for the design of the ramjet engine. However, use of a booster rocket and the independent structure inevitably leads to higher total lift-off weight. Therefore, the success of this design depends on the ability to reduce the total lift-off weight in order to accommodate a higher payload. To achieve this goal, the following measures have been incorporated in this design:

1. Early ignition of the ramjet engine in order to extend its operating range.

By advancing the ignition time of the ramjet engine so it occurs at high subsonic speed rather than low supersonic speed, one can reduce the fuel consumption of the booster rocket and therefore carry a smaller amount of oxidizer. Typically, ignition of a ramjet engine takes place at  $Ma = 1.5$ , and full operation begins at  $Ma = 2$ . Because of the high thrust-to-weight ratio of a rocket engine, it can accelerate the space plane quickly to a sufficiently high velocity for the ramjet engine to begin operation. On the other hand, because of its low specific impulse, a large amount of propellant is consumed per unit time per unit thrust; this implies that a large amount of liquid oxygen must be consumed to accelerate from  $Ma = 0$  to  $Ma = 2$ , thereby increasing the total lift-off weight. In this design, the ejection effect of the rocket exhaust is used to advance the ignition of the ramjet engine ( $Ma = 0.8$ ), and the propellant supply to the rocket engine is diminished at  $Ma = 1.5$  in order to conserve the amount of oxidizer.

2. High-altitude oxygen replenishment in the ramjet engine in order to reduce the size and weight of its air-inlet.

One of the difficulties of operating a ramjet engine from low to high altitude is the large variation in the required air flow that must pass through the air intake. Even an adjustable air intake provides only a limited amount of adjustment of the intake area. If the intake size or the

capture area is designed based on the high-altitude Mach number, it will be much larger than the required area under low-altitude low-Mach-number conditions. As a result, the space plane will experience large frontal drag and severe spill-over drag at low altitudes. By incorporating high-altitude, high-Mach-number oxygen replenishment in the ramjet engine, it is possible to reduce the air-flow requirement, and consequently the area and weight of the air intake; also, a partial solution to the problem of conflicting air-flow requirement between low- and high-Mach-number conditions can be obtained. The replenished oxygen is supplied by the liquid-oxygen tank of the rocket engine; the supply system is a simple, small tube with a one-way valve.

The advantages of the oxygen-replenishment technique can be summarized as follows:

(1) Reduction in the structural weight of the air intake:

a. Reducing the intake dimensions results in weight reduction.

b. Cooling of the high-velocity, high-temperature gas reduces the heating load on the structure, which in turn reduces weight.

(2) Improvement in engine performance:

a. Reduces the frontal drag and the spill-over drag at low altitude.

b. Partially resolves the difficulty of mis-matched air-flow requirement between the air intake and the combustion chamber (including the tail exhaust) at low and high Mach numbers.

The above two design measures show that the use of a rocket engine in this system not only provides the booster for lift-off, but also extends the operating range of the ramjet engine and reduces its structural weight. In other words, it partially compensates for the effect of low specific impulse of the rocket engine, and fully exploits the superior performance of the ramjet engine.

3. Based on the performance requirements of the ramjet engine, the separation velocity between the two stages is chosen to be Mach 6.5. However, it is possible to extend the separation velocity to Mach 7.0 by injecting water to cool the air flow and to increase thrust. This is used only as a back-up measure in case new containers and new tubings are added to the system.

### III. Verification of the Overall Design Concept

Verification of the design concept is based on an optimized propulsion system. The verification process involves estimating the system performance and weight based on the mission objective, which is to carry a 6-Mg payload to a 500-km low-earth orbit. The engine performance parameters used in the calculation are shown in Table 1.

Table 1. Engine Performance Parameters

	Engine type	Propellant	Specific impulse, s (vacuum/sea level)	Thrust-to-weight ratio	Operating Mach number
Launch-vehicle type	Rocket engine	LH <sub>2</sub> , LO <sub>2</sub> , hydro-carbon	370/345	86.5	0-2
	Ramjet engine	LH <sub>2</sub>	Average 3,500	30	0.8-6.5
Orbiter	Rocket engine	LH <sub>2</sub> , LO <sub>2</sub>	460/367	73.3	6.5-25

For purposes of comparison, weight estimates have been calculated for three TSTO designs: HTO rocket-ramjet-rocket design, VTO rocket-ramjet-rocket design, and VTO rocket-plane design. The calculated results are shown in Table 2.

Table 2 shows that with identical orbiter weight, the total lift-off weight of the rocket plane is 157 Mg and 174 Mg heavier than the HTO and VTO rocket-ramjet-rocket designs, respectively. This is because the carrier vehicle (i.e., launch vehicle) of the rocket plane is 161 Mg and

Table 2. Weight Estimates of Three TSTO Designs

	Total lift-off weight, Mg	Launch-vehicle weight, Mg	Orbiter weight, Mg	Orbiter weight at orbital injection, Mg
HTO rocket-ramjet-rocket design	330	198	132	28
VTO rocket-ramjet-rocket design	313	181	132	28
VTO rocket plane	487	359	128	28.5

178 Mg heavier than that of the other two designs. Prior to stage separation, the rocket plane will consume 150 Mg more propellant than the rocket-ramjet-rocket designs. This includes 120 Mg of extra propellant due to

the lower specific impulse of the rocket engine, and an additional 30 Mg to accelerate this propellant to the ramjet relay velocity.

A comparison of the two rocket-ramjet-rocket designs (HTO versus VTO) shows the following:

1. Since the altitude, velocity and inclination of the two carrier vehicles at stage separation are identical, the initial weight and orbit-injection weight of the two designs are also identical. Therefore, the main difference lies primarily in the carrier vehicle.
2. The trajectory and fuel consumption during ramjet operation are essentially the same for the two designs.
3. The wing area is determined by the ramjet requirements prior to stage separation; therefore, there is little difference between the mass coefficients of the wing designs.
4. The HTO design must have a larger (hence heavier) wing surface to generate sufficient lift for take-off; on the other hand, the lifting surface reduces the required thrust level generated by the rocket booster. Therefore, under the same thrust-to-weight ratio, the fuel consumption required to reach ramjet velocity is smaller for the HTO design than for the VTO design.
5. The landing gear for the HTO design is heavier than that for the VTO design.

The overall weight estimate for the HTO design is 17 Mg higher than that for the VTO design (see Table 2); however, this difference is only 5 percent of the total lift-off weight. Given that the total lift-off weight is approximately the same, the HTO design is a preferred design because it has more flexibility in launch options, requires no cumbersome launch tower, is easier for ground servicing and maintenance, and has lower launch cost.

The selection of thrust-to-weight ratio is based on considerations of limiting the operating time and fuel consumption of the rocket engine, and minimizing the axial load and noise level; the compromised value chosen for the thrust-to-weight ratio is 1.

In summary, the proposed design is a horizontal take-off and landing (HTOL), two stage to orbit (TSTO) rocket-ramjet-rocket design.

#### IV. Overall Configuration

The HTOL/TSTO rocket-ramjet-rocket space plane includes the first-stage carrier vehicle and the second-stage orbiter. During take-off, the orbiter is carried on the back of the aircraft; during landing, each vehicle lands horizontally on its own. The propulsion system of the carrier vehicle consists of eight hydrogen-oxygen-hydrocarbon liquid rocket engines and eight liquid-hydrogen ramjet engines arranged in a parallel array. The propulsion unit of the orbiter consists of four liquid-hydrogen/liquid-oxygen rocket engines.

The external shape of this design is shown in Figure 1. The orbiter is carried by the launch vehicle in piggy-back fashion in order to reduce the overall length of the space plane and to provide favorable conditions for the air intake of the ramjet engines. The fuselage of the aircraft is widened to accommodate the parallel arrays of the rocket engines and ramjet engines. The widened fuselage becomes part of the lifting surface to form an integrated wing-fuselage structure. The eight ramjet engines are installed in a parallel array below the fuselage to take advantage of the pre-compression provided by the forward fuselage and the full expansion provided by the open space of the rear fuselage.

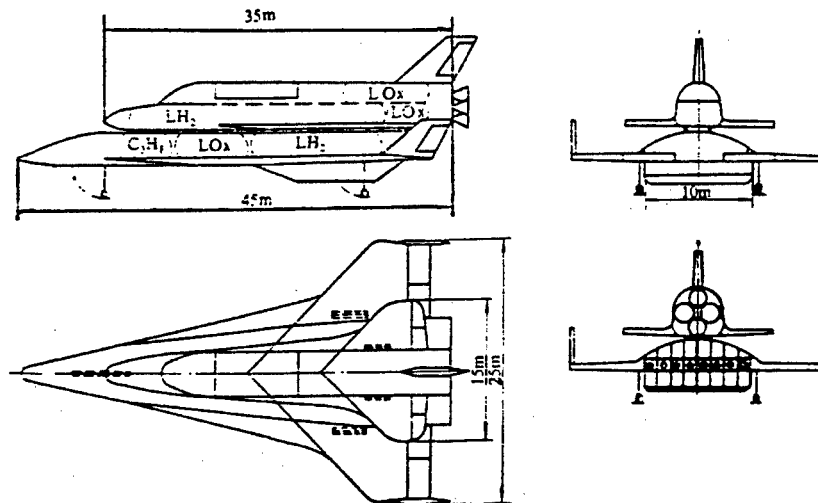


Figure 1. External Shape of the Rocket-Ramjet-Rocket Space Plane

The wing area of the orbiter is determined on the basis of a landing load of  $2.55 \text{ kN/m}^2$ . The wing area of the launch vehicle is determined by a take-off wing load of  $10.79 \text{ kN/m}^2$ , which satisfies the required angle-of-attack condition of the ramjet engine prior to stage separation.

The basic dimensions and weight estimates of this space plane are listed in Table 3. The data in Table 3 shows that the payload ratio is 0.018, which is considered state-of-the-art performance based on use of 1990's technologies.

**Table 3. Basic Technical Data for the HTOL/TSTO Rocket-Ramjet-Rocket Design**

Parameter	Units	Orbiter	Booster vehicle
Payload	Tons	6 (including 2-3 astronauts)	
Take-off weight	Tons	132	198
Orbit-injection weight	Tons	28	
Empty weight	Tons	18.4	78
Climb propellant	Tons	104	111
Landing weight	Tons	25.34	79
Structural weight	Tons	13.4	61.6
Equipment weight	Tons	2.9	3.8
Reserve fuel weight	Tons	0.94	9 (contains 8 tons of fuel for return trip)
Engine weight	Tons	2.1	3.45 (rocket) + 9.15 (ramjet)
Orbiter booster propellant	Tons	2.66	
Length of fuselage	Meters	35	45
Diameter of fuselage	Meters	4.2	
Wing span	Meters	15	25
Wing area	Square meters	97	300
Propulsion system		4 hydrogen-oxygen engines	8 hydrogen-oxygen-hydrocarbon engines, 8 hydrogen ramjet engines

## V. Flight Trajectory

The flight trajectory of the space plane is primarily determined by the mission requirements. Figure 2 shows a schematic of the space-plane trajectory. Figure 3 shows the trajectory of the climb segment and the transfer-orbit segment, as well as changes in weight.

The flight trajectory can be divided into four segments:

### 1. Booster-Propelled Take-Off Segment (Figure 3 a)

In the take-off segment, the space plane is accelerated by the rocket engine to a take-off velocity of 140 m/s; a 2,000-m-long runway is required for take-off. The climb angle at take-off is approximately  $17^\circ$ . The amount of propellant consumed during this segment is approximately 15 tons.

### 2. Rocket-Propelled Climb Segment (Figure 3 a-b-c)

After take-off, the rocket engine continues to accelerate the space plane until it reaches the high subsonic speed of  $Ma = 0.8$ , at which point the ramjet engine is ignited. This design requires that the ramjet engine begin operation as early as possible in order to conserve rocket propellant. At subsonic speeds, the thermal efficiency of the ramjet engine is rather low and only a small thrust is produced; however, the net thrust of the propulsion system is increased because the base drag is eliminated. Ignition of the ramjet engine at subsonic speed is made

possible by the ejection effect of the rocket exhaust on the ramjet engine. Thus, the ramjet engine will begin producing thrust at transonic speed, and at  $Ma = 1.5$ ,  $H = 5 \text{ km}$ , it can produce more than 60 percent of the thrust needed by the space plane. During this period, the ramjet engine and the rocket engine operate simultaneously. In order to conserve propellant, the propellant flow to the rocket engine is reduced at approximately  $Ma = 1.5$ ; at  $Ma = 1.8-2.0$ ,  $H = 9 \text{ km}$ , the rocket engine is shut off, and the ramjet engine completely takes over. Based on preliminary analysis, the maximum inclination of the climb segment for an optimum trajectory is  $28.5^\circ$ , and the propellant consumption is approximately 84 tons.

### 3. Ramjet-Propelled Climb Segment (Figure 3 c-d)

After a velocity of Mach 2, the ramjet engine produces all the thrust needed by the space plane. Its operation continues until  $Ma = 6.5$ ,  $H = 32-37 \text{ km}$ , and with water injection in the engine, it can be further extended to  $Ma = 7$ .

In order to accelerate the space plane to stage-separation velocity as quickly as possible, the ramjet engine should operate at the lowest possible altitude to produce a large specific impulse. Based on advanced technologies available in the 1990's, we have chosen the dynamic pressure of the space plane to be  $q = 70 \text{ kPa}$ , and the load limit of the ramjet engine to be 1 MPa. The altitude-velocity curve corresponding to these two limits is shown in

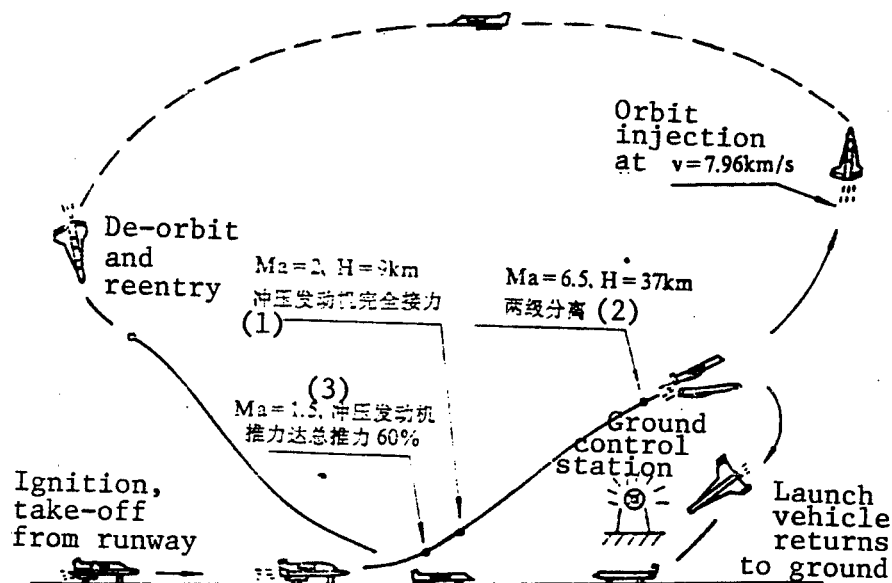


Figure 2. Flight Trajectory of the Space Plane

Key: 1. At  $Ma = 2, H = 9 km$ , all the thrust is provided by the ramjet engine 2. At  $Ma = 6.5, H = 37 km$ , stage separation takes place 3. At  $Ma = 1.5$ , the thrust of ramjet engine reaches 60 percent of the total thrust

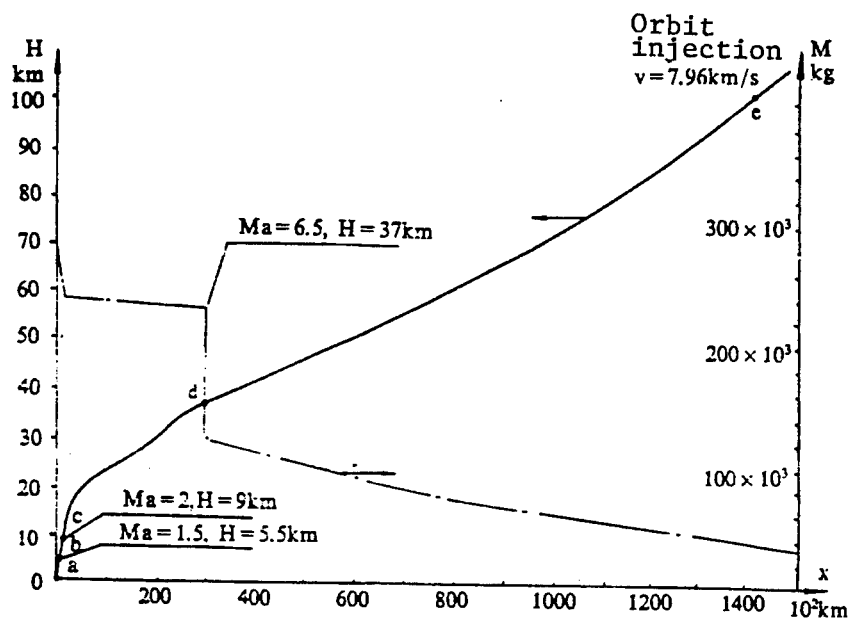


Figure 3. Flight Trajectory of the Climb Segment and the Transfer-Orbit Segment and Corresponding Weight Variation



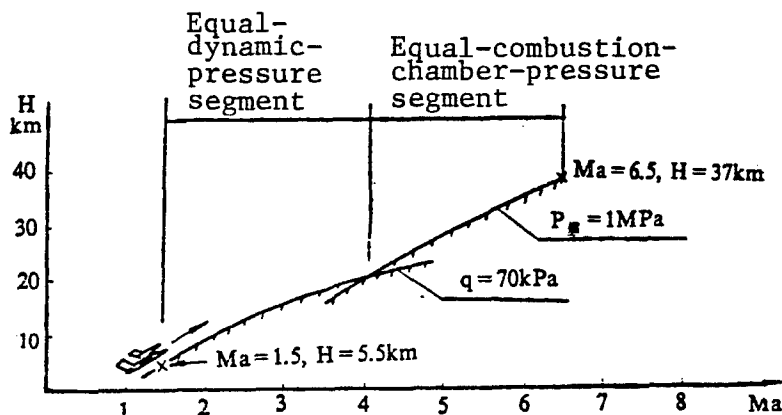


Figure 4. Altitude-Velocity Curve of the Climb Trajectory

Figure 4. It can be seen that for  $Ma \leq 4.1$ , the flight condition is constrained by the dynamic pressure; for  $Ma > 4.1$ , it is constrained by the load in the combustion chamber of the ramjet engine. An ideal acceleration profile would be to follow a curve along the equal dynamic pressure contour and the contour of equal combustion-chamber pressure. The total operation time of the ramjet engine is 250-270 seconds, and the total fuel consumption is 12-13 tons. The ramjet engine has very high thermal efficiency because it uses liquid-hydrogen fuel which has high specific heat, and its products of combustion have lower dissociation rate than hydrocarbon fuel under high-temperature conditions; consequently, the average specific impulse of the engine under normal conditions can be as high as 3,500 sec. Compared with the rocket engine, the ramjet engine can save over 120 tons of propellant, thereby greatly reducing the take-off weight. When the velocity reaches  $Ma = 6.5$ , the ramjet engine is shut off; the carrier vehicle is separated from the orbiter and returns to earth. For the sake of safety during reentry, the ramjet engine is still used to propel the carrier vehicle until it is ready to land.

#### 4. Rocket-Propelled Transfer Orbit Segment (Figure 3 d-e)

When the velocity reaches  $Ma = 6.5$ , the liquid-hydrogen/liquid-oxygen engine on the orbiter is ignited and separates from the carrier vehicle. The orbiter accelerates along an optimum trajectory to enter a  $100 \times 500$  km elliptical orbit; the orbit-injection altitude is 100 km and the injection velocity is 7,961 m/s (absolute velocity). The operation time of the rocket engine is approximately 350 sec, and the propellant consumption is 104 tons. At apogee (altitude = 500 km), an auxiliary motor of the orbiter is activated, which provides an additional velocity increment of 119 m/s to place the orbiter in a 500-km circular orbit.

#### VI. Conclusion

1. In this design, the propulsion system of the first-stage carrier vehicle uses two technically mature and well-proven engines: the liquid-propellant rocket engine and

the ramjet engine. This approach minimizes technical risk, shortens the development cycle and reduces development cost.

2. The key feature of this design is that the ramjet engine operates over a wide Mach-number range, thereby reducing the total take-off weight. This is achieved by using two key technologies: early ignition and high-altitude oxygen replenishment.

3. Verification calculations of the overall design have provided weight estimates of the space plane and have shown the payload ratio to be 0.018. This is considered state-of-the-art performance based on use of 1990's technologies.

#### Additional Details on Aircraft-Engine High-Altitude Simulation Test Station

91FE0821A Beijing HANGKONG ZHISHI  
[AEROSPACE KNOWLEDGE] in Chinese No 7, Jul 91  
pp 2-3

[Unattributed article: "High-Altitude Simulation Test Station' Completed"; cf. earlier brief report in JPRS-CST-91-015, 9 Jul 91 p 5]

[Text] The aircraft engine high-altitude simulation test station was designed by the Aircraft Industry Planning and Design Institute and the Chinese Aircraft Gas Turbine Research Institute; its construction involved more than 200 different organizations and lasted 26 years. The test station is an essential research and experimental facility which provides this country the autonomous capability to develop its aircraft industry. Its total cost is only one-eighth of the cost of similar high-altitude test stations built by other countries.

The high-altitude simulation test station is a high-tech, systems-engineering test facility; it consists of three major sections: the air inlet system, the high-altitude chamber, and the exhaust system, and contains several hundred pieces of heavy equipment. It is capable of simulating the internal and external environment

encountered by aircraft engines, and measuring the engine performance and various parameters under different flight conditions.

In the past, when China did not have a "high-altitude test station," integrated engine tests had to be performed by installing the engine on an aircraft and conducting direct tests in flight. While this method provides realistic data, the range and quantity of test data are limited due to limitations in the actual flight altitude and velocity of the aircraft and the limited amount of test equipment that can be accommodated inside the aircraft. Data at other altitudes and velocities can only be obtained through similarity transformations; the accuracy of the data is therefore relatively poor. In addition, actual flight tests involve higher risks because they are subject to the constraints of weather conditions. These limitations are completely removed when the "high-altitude test station" is used to conduct integrated engine tests. Therefore, the test station is an essential experimental research tool for developing China's aircraft industry. Currently, only Great Britain, the United States, France and the Soviet Union have succeeded in building their own high-altitude test stations.

The "high-altitude simulation test station" is a large, complex and technically sophisticated facility. One of its major pieces of equipment, the exhaust cooling unit, is 81 m long and weighs 1,500 tons; its total amount of heat exchange is equivalent to that of 21 steam locomotives. The core unit of the high-altitude test station, the high-altitude chamber, has been developed for the first time in this country; it is 23 m long and weighs 175 tons; it has 5,600 meters of weld lines which consumed 7.8 tons of weld rods.

During the development of China's "high-altitude test station," a parallel approach of construction, tuning and testing, and actual operation was adopted. Test results of the air-supply station, the air-treatment system, the exhaust system and the high-altitude chamber indicate that the performance of all the major components and subsystems has met or exceeded design requirements.

This facility can be used to conduct tests in nine different areas including adjustment and verification of the altitude and speed characteristics of the engine, performance tests and reliability tests of various components and subsystems, as well as tests for engine improvement and development. It has a sufficiently wide operating range to meet the research and development needs for China's aircraft engines. In 1986, it was used to conduct high-altitude performance tests of China's newly developed aircraft engine, which contributed to the successful certification of the engine design.

#### Satellite Reentry and Recovery

91FE0794A Beijing SHIJIE DAODAN YU HANGTIAN [MISSILES & SPACECRAFT] in Chinese No 6, Jun 91 pp 15-17, 21

[Article by Lu Zhangfu [7120 4545 4395] of the Beijing Institute of Electromechanical Research and Design: "Recovery and Return of Satellites"]

[Text]

#### Abstract

China is one of the few countries in the world that has the capability to recover its satellites. This paper describes the reentry and recovery of China's recoverable satellites; specifically, it gives a description of the heat-protection system of the reentry capsule, the reentry attitude-control system, and the major factors which affect the accuracy of the reentry orbit. The composition of the recovery system, the recovery control and the recovery sequence are described in detail.

#### I. Introduction

Since China launched and recovered its first recoverable satellite on 29 November 1975, it has successfully launched 12 recoverable satellites.

In order for an orbiting satellite to return safely to earth, it must be equipped with a telemetry and control system, an attitude-control system, a retro-rocket engine, a recovery system and a reentry heat-protection system.

A typical recoverable satellite built in this country has a mass ranging approximately from 1,800 to 2,100 kg, and its orbit parameters are: perigee altitude 175-210 km, apogee altitude 404-490 km, period 90-91 minutes, and inclination 57°-68°.

During the orbit pass prior to reentry, the satellite is tracked by ground tracking and control stations as it passes over China; it also receives remote-control commands from the ground, and sends back telemetry signals which contain information on the satellite response to the control commands and reentry-related parameters. When the satellite reaches a pre-determined reentry point, the ground station transmits the following sequence of commands to the satellite: attitude-correction command, module-unlocking command, reentry-capsule spin command, retro-rocket engine ignition command and reentry-capsule despin command. The retro-rocket engine is activated when it is oriented at a pre-determined retro angle; at engine cut-off, the reentry capsule leaves the orbit and re-enters the atmosphere along a ballistic trajectory. When the ballistic coefficient (axial overload coefficient) reaches a certain value, the recovery sequence is initiated by the control system. First, the heat-shield base cover is discarded; then the recovery responder and the recovery beacon are turned on to facilitate monitoring by the ground station. When the reentry capsule falls to a certain altitude, the pilot chute is ejected, thus retracting the braking chute, which in turn retracts the main chute. Finally, the satellite lands safely at a landing site located in southwestern China. Figure 1 shows the reentry and recovery sequence.

#### II. Reentry

In order to change the orbit parameters of an orbiting satellite, it must be given an impulse generated by the

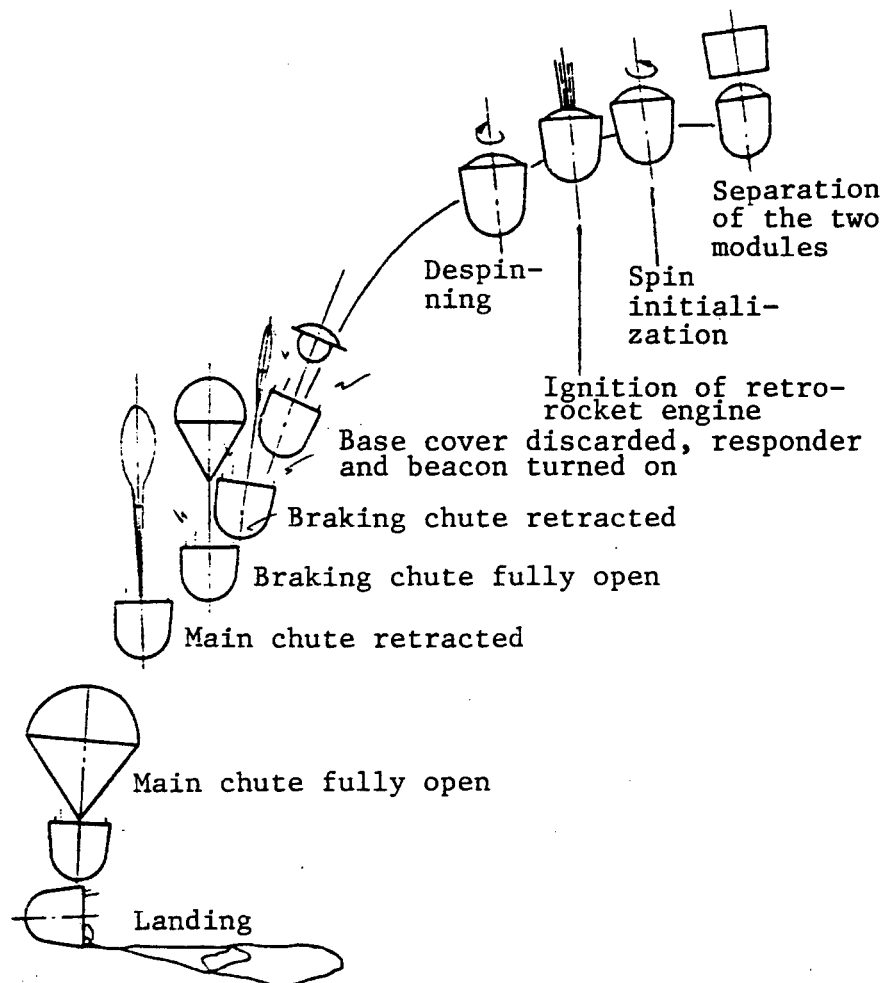


Figure 1. Satellite Reentry and Recovery Sequence

retro-rocket engine; the direction of the impulse is determined by the retro angle of the attitude-control system. Once the rocket engine is shut off, the magnitude and direction of the final velocity vector of the satellite are determined. Thus, the first step in the recovery sequence is to change the satellite orbit by accurately controlling the magnitude and direction of the imparted impulse to ensure that the satellite will land at the designated landing site.

#### (1) Reentry Capsule Heat-Protection System

The heat-protection system is designed to ensure that the satellite will return to earth safely without burning up as it penetrates into the atmosphere. Therefore, in the structural design of the reentry capsule, one must consider not only the environmental conditions during the ascending and orbiting segments of the flight, but particularly the high-pressure and high-temperature (surface temperature can reach several thousand degrees Celsius) conditions encountered by the satellite during reentry.

At the start of reentry, the reentry capsule flies at a high angle of attack. Since the capsule is dynamically stable, as it descends in altitude, the angle of attack will gradually decrease under the action of aerodynamic moments; as a result, the spherical nose section is subject to intense heat load. In the design of the heat-protection system, different materials are used for different parts of the capsule according to the heat load distribution. The spherical nose section is made of magnesium alloy and "XF" composite material; the skirt of the capsule is also made of "XF" composite material to guard against abrasion. The base cover has a silicon rubber coating and a high-temperature insulation structure on the inside because it has a relatively low heat flux, and its surface is in a state of thermal equilibrium with moderate surface temperatures.

#### (2) Reentry Attitude Control

Prior to reentry, it is necessary for the attitude-control system to make a large adjustment to the satellite pitch angle. The attitude-control system uses a horizontal gyro

equipped with a constant-speed program mechanism. When a control command (program control supplemented by remote control) for attitude adjustment is received, the system first cuts off the infrared earth sensor so that the horizontal gyro is now in a free state; it then activates the program mechanism to meet the pitch-angle adjustment requirement. The pitch angle is the retro angle referred to earlier; its magnitude is in the range of  $100^{\circ}$  to  $110^{\circ}$ . For a given total impulse provided by the retro-rocket engine, the magnitude of the retro angle directly affects the de-orbit velocity of the satellite and consequently its landing position. To require that the retro angle remains constant during engine operation, one must address the attitude stability problem. If the attitude control is located on the reentry capsule, then the retro angle can still be controlled even during engine operation. Since the attitude-control system of China's recoverable satellite is located on the instrument module, it can no longer control the retro angle of the reentry module once it is separated from the instrument module (the separation process has negligible effect on the retro angle). For this reason, a spin rocket is used to spin-stabilize the reentry module; the spin velocity is 100 rpm.

However, the reentry capsule remains in a spin-stabilized state even after the retro engine is shut off, thus preventing the angle of attack from decreasing quickly during reentry under the action of aerodynamic moments; this may cause the lateral overload coefficient to exceed the axial overload coefficient. In order to avoid excessive pressure and temperature acting on the skirt section of the reentry capsule, a despinning operation must be initiated after engine cut-off. The purpose of the despinning operation is to reduce the angle of attack during reentry, so that the most severe aerodynamic heating would occur at the spherical nose section, and the lateral overload would be reduced at the expense of the axial overload.

### **(3) Major Factors That Affect the Accuracy of the Reentry Orbit**

The accuracy of the reentry orbit has a significant effect on the operation of the recovery system and the location of the satellite landing point. The major factors that affect the accuracy of the reentry orbit include: errors in the estimated orbit parameters at the end of the orbiting segment, errors in the attitude angles and angular velocities after final attitude adjustment, errors in the total impulse and the direction of the thrust vector of the retro-rocket engine, errors in the predicted aerodynamic coefficients of the reentry capsule and errors in the estimated atmospheric density.

## **III. Recovery**

The recovery system is an important subsystem whose function is to ensure safe landing of the reentry capsule at a moderate speed.

### **(1) Composition of the Recovery System**

The basic components of the recovery system include the recovery chute compartment, the deceleration unit—parachute system, the ejection unit, the control unit, and the position-indication system.

The recovery chute compartment serves not only as a storage unit for the parachute but also as a load-transmitting member between the retro-rocket engine and the reentry capsule; it connects the retro engine to the heat-protection base cover. The ejection tube on the recovery chute compartment is used to eject the base cover and the engine housing.

The deceleration unit—parachute system consists of the pilot chute, the braking chute, the main chute, the rotary joint, the long connecting rope and the roof-shaped rope.

The ejection unit includes the ejection tube, the chute-ejection device, the chute-release bolt and the chord-cutting mechanism.

The control unit includes the acceleration switch, the time-sequence controller, the power distributor, the recovery power supply and the electric cables.

The position indication system includes the responder, the ultra-shortwave beacon and medium-wave beacon, as well as ground measurement and direction-finding equipment.

### **(2) Recovery Control System**

The recovery control system uses an overload time-sequence controller. When the satellite instrument module is separated from the reentry capsule, the controller is activated and sends the following commands through the power distributor: spin-rocket ignition, retro-engine ignition, and despin-rocket ignition; it then closes the circuit to the overload switch, and waits for the switch-over command from the remote controller to break the first starting circuit. When the axial overload coefficient reaches a certain value, the overload switch is closed; the time-sequence controller is again activated, and sends the commands to eject the base cover (also to turn on the responder and the beacons), and to eject and release the parachutes. At the same time, the deceleration unit—parachute system begins operation according to a pre-determined sequence.

### **(3) Ejection of Base Cover**

The recovery system is located inside the sealed reentry capsule. Prior to parachute deployment, it is necessary to first eject the heat-protection cover at the base of the reentry capsule and the housing of the retro-engine. During the ejection process, the reentry capsule is traveling at transonic and supersonic speeds, where a complex region of wake flows exists behind the capsule. If the ejection velocity is too low, the base cover will remain in the wake-flow region and block the parachute from being deployed. For this reason, wind-tunnel tests of the reentry capsule and the detached base cover must first be

conducted at transonic and supersonic speeds to provide test data which can be used in a dynamic analysis to determine the minimum separation velocity such that the ballistic coefficient of the reentry capsule would be greater than or equal to the ballistic coefficient of the base cover.

#### **(4) Deceleration of the Reentry Capsule**

The reentry capsule undergoes rapid deceleration after it enters the atmosphere; at the time of base-cover ejection, its velocity has decreased from hypersonic to transonic or supersonic range. However, aerodynamic drag alone cannot slow down the reentry capsule sufficiently to ensure safe landing. To further reduce its speed, a two-stage parachute system which deploys a braking chute and a main chute in sequence is used. The recovery sequence is as follows:

After ejection of the base cover, a command is issued by the time-sequence controller to activate the chute ejector which ejects the pilot chute into the wake-flow region behind the reentry capsule. The drag force on the pilot chute causes the braking chute to be retracted; after a certain time delay, the pull chord is cut, and the braking chute is fully opened. When the reentry capsule slows down to a stable descending velocity, the time-sequence controller issues a command to release the braking chute by activating the chute-release bolt; at the same time, the drag force acting on the braking chute causes the main

chute to be retracted. After a certain time delay, the pull chord is cut, and the main chute is fully opened. Under the action of the main chute, the reentry capsule slowly descends to the ground.

#### **(5) Position Indication**

When the reentry capsule reaches the air space above the recovery zone, the awaiting search team can determine the position of the reentry capsule based on the responder signals received by the ground radar. Also, the ultra-shortwave beacon signal received by the gyro onboard the recovery aircraft allows it to follow the reentry capsule to its landing spot. If the reentry capsule lands safely on an open field, the recovery crew can proceed to the landing spot and prepare the capsule for transfer by helicopter to a designated location, as shown in Figure 2 [photo not reproduced]. If the capsule lands in a forest, then the search team can use a direction-finding device to locate the capsule by tracking the medium-wave beacon.

#### **IV. Concluding Remarks**

The successful launches and recoveries of China's 12 recoverable satellites have demonstrated that the technology of ballistic recovery of artificial earth satellites in this country has attained a high degree of maturity; currently, this technology is only shared by the United States and the Soviet Union.

**Advanced Graphite Composite Fabricated,  
Analyzed, Compared with German Product**

91FE0745 Harbin HARBIN GONGYE DAXUE  
XUEBAO [JOURNAL OF HARBIN INSTITUTE OF  
TECHNOLOGY] in Chinese No 3, Jun 91 pp 75-80

[Article by Zhang Zhiqian [1728 1807 6197], Chen Erlong [7115 0059 7893], Ren Yulong [0117 5940 7127], and Zhang Wejia [1728 4850 0857] of the Harbin Institute of Technology Chemistry Department: "Research on Advanced Graphite Composite"; manuscript received Nov 1989]

[Text] Abstract: High-performance graphite composite was fabricated as a molded compound from graphite and synthetic resin at a specific temperature and pressure. This project studied the effects of various graphite mixtures, graphite particle size, resin selection, and compounding techniques on the physical and mechanical properties of the composite and did microscopic analysis of fractures in the graphite composite.

Key terms: graphite, graphite composite, graphite slide

Chinese book data classification number: TQ165

**I. Introduction**

Graphite composite is a new industrial material developed during the 1970's. It is prepared by molding a compound composed of graphite and synthetic resin at a specific temperature and pressure. Because it has the electric conductivity, thermal conductivity, and self-lubrication properties of graphite as well as the high bending resistance and impact resistance properties of engineering plastics, it has been widely used in slides in various types of air compressors and vacuum pumps<sup>[1]</sup>.

The birth of graphite composites attracted attention in all countries and many research achievements have been made. Research on graphite composites has developed most quickly in West Germany and the SIT60-100 graphite composite developed there has a bending strength of 60 N/mm<sup>2</sup>, a compressive strength of 100 N/mm<sup>2</sup>, an impact strength of 2.5 J/mm<sup>2</sup> x 10<sup>-3</sup>, and a resistivity of less than 550  $\mu\Omega$ m. China only recently began doing research on graphite composites and we have made definite research achievements, but we have not fully attained the performance indices of the West German graphite composite. To improve the overall performance of our graphite composites, our project

used a resin with powerful bonding capabilities and good heat resistance properties, changed the graphite component ratio, increased the surface bonding of the graphite and resin, and employed other measures to make a graphite composite that attained the performance indices of West Germany's SIT60-100 graphite composite.

**II. Experiments**

**A. Materials**

1. Scaly graphite G<sub>1</sub>: Nanshu, Shandong
2. Artificial graphite G<sub>2</sub>: Harbin Electronic Carbon Institute
3. Phenol-modified diphenyl ether phenol aldehyde resin PF: Harbin Insulating Materials Plant
4. Polyimide PI: Beijing Academy of Sciences Chemistry Institute

**B. Technical process**

The graphite and resin were mixed, placed into a colloid grinder, and refluxed for 30 minutes. They were then removed and the solvent was extracted. After removal of the solvent, the block was broken up in a pulverizer and sifted. It was then molded at a specific temperature.

**C. Sample processing and testing**

The resistivity, Shore hardness, bending strength, compressive strength, and impact strength were processed and tested based on GB1994-2, 4, 7, 8, 9.

**D. Analysis of cross-sectional morphology**

An SIS-60 scanning electron microscope was used to observe and analyze impact fractures in the graphite composite.

**E. Thermal analysis**

TG-DTA analysis was conducted of the PF and PI.

**II. Results and Discussion**

**A. Effects of different types of resin on material properties**

The properties of the graphite composite depended on the type of resin. For specific types and amounts of graphite, there were rather large variations in the compressive strength, as shown in Table 1.

**Table 1. Effects of Resin Type on the Compressive Strength of the Graphite Composite**

Compressive strength (N/mm <sup>2</sup> )	20°C	200°C	Loss rate
G <sub>2</sub> /PF	111	48.0	56.8 percent
G <sub>2</sub> /PI	120	84.5	29.6 percent

Table 1 shows that G<sub>2</sub>/PF and G<sub>2</sub>/PI have approximately the same compressive strength at 20°C. When the temperature was raised to 200°C, however, the compressive

strength of the G<sub>2</sub>/PF dropped from 111 N/mm<sup>2</sup> to 48.0 N/mm<sup>2</sup>, a strength loss rate of 56.8 percent, whereas the compressive strength of the G<sub>2</sub>/PI only dropped from

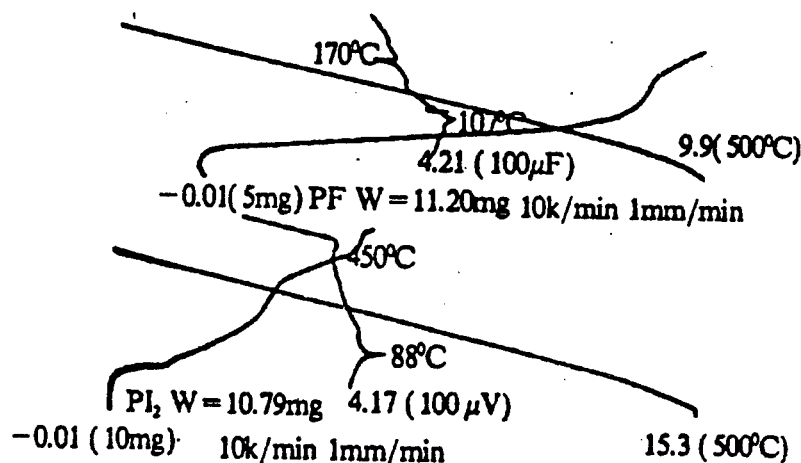


Figure 1. TG-DTA Spectragraph of PF and PI

120 N/mm<sup>2</sup> to 84.5 N/mm<sup>2</sup> a strength loss rate of just 29.6 percent, so there was a substantial difference in the compressive strength loss rates of the two. The main reason for this change was the resin in the graphite composite. Because graphite itself is a material that is resistant to high temperatures, there was almost no change from 20°C to 200°C. The thermal properties of the PF and PI were different, however, as shown in Figure 1. PF had a heat release catabolic peak at 170°C. This heat release catabolic peak was due to fracturing of the ether linkage which caused destruction of the entire cross-linked structure, leading to an abrupt reduction in the compressive strength of the material. With the exception of a small heat absorption effect peak at 88°C, PI was relatively smooth all the way to 450°C and no heat

release catabolic peak was present<sup>[2]</sup>. This shows that the molecular structure of PI had adequate thermal stability. Thus, the high-temperature compressive strength loss ratio of G<sub>2</sub>/PI was relatively low.

#### B. Effects of molding process conditions on material properties

The primary molding process conditions for the graphite composite are molding temperature, pressure, and pressure sustaining time. These three conditions have considerable effects on the properties of the material. Among them, the molding temperature should generally be determined by the solidification temperature of the resin in the graphite composite. The effects of molding pressure and pressure sustaining time on the properties of the material are shown in Table 2.

Table 2. Effect of Molding Process Conditions on G<sub>2</sub>/PI Properties

Property	Process conditions							
	Molding pressure (MPa)				Pressure sustaining time (minutes)			
	3	5	7	9	5	10	20	40
Resistivity (μΩm)	498	502			498	502	504	505
Shore hardness (HS)	30	30			30	30	30	30
Bending strength (N/mm <sup>2</sup> )	63.2	64.1	Internal cracking appears	Total fracturing	63.7	64.2	64.6	65.1
Compressive strength (N/mm <sup>2</sup> )	118	120			117	120	121	123
Impact strength (J/mm <sup>2</sup> x 10 <sup>-3</sup> )	2.47	2.52			2.50	2.52	2.54	2.55

Table 2 shows that at a molding pressure of 3 to 5 MPa, the resistivity and hardness of the material basically remained unchanged while there was a slight increase in the bending strength, compressive strength, and impact strength. The reason is that increased pressure caused greater fluidity of the material and overcame the recoil force created by the escaping gas. However, because the graphite material fractured easily during high-temperature and high-pressure

molding, when the pressure exceeded 5 MPa, the poor infiltration of the resin into the graphite caused the appearance of resinless graphite accumulations within small areas in the material and these graphite accumulations began to slide under the high pressure. They slid toward the surrounding area and diffused, causing destruction of the cross-linked structure of the resin. Less attention should be given diffusion over a limited range while greater attention

should be given to diffusion to the edges of the whole material which causes fracturing of the whole material.

Table 2 shows that the pressure sustaining time had no effect on hardness while there was a slight increase in resistivity, bending strength, compressive strength, and impact strength, although the changes were small. This shows that the resin can solidify within a short period of time. However, one problem arising from a too-short pressure sustaining time is that the graphite composite

fractured easily during processing. To increase productivity, with a prerequisite of not affecting the properties of the material, the molding time should be as short as possible. Thus, a pressure sustaining time of 10 minutes is best.

### C. Effects of graphite particle size on material properties

Graphite of different particle sizes also leads to differences in the various properties of the composite material, as shown in Table 3.

Table 3. Effects of Graphite Particle Size on G<sub>2</sub>/PI Properties

Dimensions (m)	Properties				
	Resistivity	Shore hardness	Bending strength	Compressive strength	Impact strength
	Units				
	$\mu\Omega\text{m}$	HS	N/mm <sup>2</sup>	N/mm <sup>2</sup>	J/mm <sup>2</sup> x 10 <sup>-3</sup>
58.0	480	25	59.1	116	2.45
49.5	484	26	60.5	117	2.47
43.0	497	28	62.8	118	2.50
38.5	502	30	64.2	120	2.53

There were a variety of defects in the lamellar structure of the artificial graphite. During the process of decreasing particle size, destruction began first at the site of defects, so the defects should be gradually reduced in number. On the other hand, when the particle size of the graphite was made smaller, its surface area increased and the bonding capacity with the resin improved. Thus, reducing the size of the graphite particles increases the resistivity, Shore hardness, bending strength, and compressive strength. Only the impact strength tends to decrease. As for the impact strength, consideration must

be given to another important factor, which is that the larger the lamellae of the artificial graphite, the stronger is its capacity for absorbing impact energy. Smaller lamellae have a reduced capacity for absorbing impact energy. This effect is sufficient to eliminate the effects of reductions in the number of defects and the stronger bonding capacity with the resin.

### D. Effects of Changing the Type of Graphite and Amount Used on the Material Properties, As Shown in Table 4.

Table 4. Effect of G<sub>1</sub> and G<sub>2</sub> Component Ratio on Material Properties

Components	Properties				
	Resistivity	Shore hardness	Bending strength	Compressive strength	Impact strength
	Units				
	$\mu\Omega\text{m}$	HS	N/mm <sup>2</sup>	N/mm <sup>2</sup>	J/mm <sup>2</sup> x 10 <sup>-3</sup>
70 percent G <sub>1</sub> /30 percent PI	281	11	45.1	72.3	1.48
42 percent G <sub>1</sub> + 28 percent G <sub>2</sub> /30 percent PI	330	13	46.3	74.2	1.52
21 percent G <sub>1</sub> + 49 percent G <sub>2</sub> /30 percent PI	427	18	49.5	82.5	1.89
70 percent G <sub>2</sub> /30 percent PI	502	30	64.2	120	2.52

Table 4 shows that as the G<sub>2</sub> content was increased, the material's resistivity, Shore hardness, bending strength, compressive strength, and impact strength all increased and the amplitude of the increases was rather large. This was due to the structural characteristics of G<sub>1</sub> and G<sub>2</sub>. Electron microphotography and X-ray scanning of G<sub>1</sub> and G<sub>2</sub> show that the lamellae in G<sub>1</sub> are thin and large and have a smooth

surface while the lamellae of G<sub>2</sub> are not as apparent as in G<sub>1</sub> and have more surface irregularities. The hexagonal graphite structure is relatively complete in G<sub>1</sub>, so the G<sub>1</sub> had good electric conductivity and thermal conductivity properties and thus a lower resistivity. Its crystal growth is excellent along the X-axis and Y-axis while growth along the Z-axis is poorer. Thus, the G<sub>1</sub> has a lamellar structure.



There were more defects in the crystal structure of the  $G_2$  and it had lamellar accumulation defects, carbon lattice chain linkage defects, intercrystalline dislocation and hole defects, and defects from the mixing of contaminant atoms<sup>[3]</sup>. These defects caused the strength and mechanical properties of  $G_1$  to be rather low.  $G_2$  is a compound of crystal form graphite and interlaced crystal carbon. There were some non-graphite structures in the  $G_2$ , so the electric conductivity and thermal conductivity of the  $G_2$  were poor<sup>[4]</sup>. Thus, its resistivity is rather high. The existence of crystalline carbon structures also caused the  $G_2$  to have rather high hardness and mechanical properties. Thus, as the content of  $G_2$  increases, the trend shown in Table 4 appears.

There were also differences in the cross-sectional morphology of the impact fractures of the  $G_1$  and  $G_2$  composites, as shown in Figures 2a and 2b [not reproduced].

The greater the integrity of the graphite structure and the greater the smoothness of its surface, the more difficult it is for the resin to infiltrate.  $G_1$  is in this condition, so lamellar accumulation phenomena appear in Figure 2. When the

material was subjected to shock, because the  $G_1$  separated easily from the PI, what is destroyed was basically the PI cross-link structure, so the  $G_1$ /PI impact strength was rather low. In the  $G_2$ , the  $G_2$  was uniformly distributed and rather strongly bonded to the PI. When it was destroyed by impact, some of the fractures were the  $G_2$  separating from the PI and some were destruction of the  $G_2$  itself. This gives the  $G_2$ /PI higher impact strength.

#### E. The effects of graphite surface processing methods on material properties

Because graphite has a rather smooth surface, the infiltration of the resin is poor and it has a weak bonding capacity with the resin, so the mechanical properties of the graphite composite were rather poor. To improve the condition of the graphite surface and increase infiltration of the resin into the graphite, thereby increasing its bonding with the resin, we used the thermal oxidation method and plasma to treat the surface of the graphite.

The thermal treatment temperature for using the thermal oxidation method to improve the condition of the graphite surface was generally 500°C.

**Table 5. Effect of  $G_1$  Oxidizing Time on  $G_1$ /PI Properties**

Time (hours)	Properties				
	Resistivity	Shore hardness	Bending strength	Compressive strength	Impact strength
	Units				
	$\mu\Omega m$	HS	N/mm <sup>2</sup>	N/mm <sup>2</sup>	J/mm <sup>2</sup> $\times 10^{-3}$
1	340	20	40.6	59.3	1.12
2	374	10	51.1	70.8	1.63
3	412	11	60.7	89.1	2.34
4	457	10	54.5	84.3	2.01

Table 5 shows that as the thermal oxidizing time was increased, the resistivity of the  $G_1$ /PI gradually increased. The reason for this is that thermal oxidation of the graphite caused an increase in the oxidation point of the graphite surface which caused the resistivity of the material to rise. Increasing the oxidation point helped the graphite bond to the resin and increased the material's bending strength, compressive strength, and

impact strength. When the treatment time was too long, however, the oxidation point was further increased and although this helped bonding of the graphite and resin, it caused the strength of the graphite itself to decline, which reduced the mechanical properties of the material.

The results of plasma treatment on the graphite are shown in Figure 6.

**Table 6. Effects of Plasma Treatment of  $G_1$  on  $G_1$ /PI Material Properties**

Power (W)	Properties				
	Resistivity	Shore hardness	Bending strength	Compressive strength	Impact strength
	Units				
	$\mu\Omega m$	HS	N/mm <sup>2</sup>	N/mm <sup>2</sup>	J/mm <sup>2</sup> $\times 10^{-3}$
200	263	10	44.1	62.7	1.22
500	324	10	52.3	78.4	1.83
800	401	10	62.9	94.8	2.25
1,000	573	10	60.5	92.3	2.13

Table 6 shows that as the plasma power was increased, the resistivity of the material gradually increased. When the plasma was acting on the graphite surface, it had considerable kinetic energy and all types of active matter collided with the graphite surface, sculpting it, and the reaction of various types of base groups on its upper surface generated many new active base groups<sup>[5]</sup>. All of these things promote bonding of the graphite and resin, increase the resistivity of the material, and increase the material's bending strength, compressive strength, and impact strength. When the plasma power was excessive, however, although it helped bonding of the graphite and resin, it also caused a reduction in the strength of the graphite itself and reduced the mechanical properties of the material.

### III. Conclusions

1. When  $G_1$  and  $G_2$  are mixed with the resin compound, increasing the  $G_2$  content increases the graphite composite's resistivity, hardness, bending strength, compressive strength, and impact strength.
2. Making the particle size of the graphite smaller increases the graphite composite's bending strength and compressive strength and reduces its impact strength.
3. The normal and high temperature properties of the graphite composite are determined by the type of resin.
4. The properties of the  $G_2$ /PI composite attained the properties of the West German SIT60-100 composite.

Project contact person: Professor Zhang Zhiqian [1728 1807 6197], Harbin Institute of Technology Chemistry Department

### References

- [1] Song Zhengfang [1345 2973 5364], Tanshimo Zhipin De Xingneng Ji Yingyong [Properties and Applications of Carbon Graphite Products], Machinery Industry Press, 1987.
- [2] Rogaylin, M. I. and Chalykh, E. F., Spravochnik po [indecipherable]grafitovym materialym [Handbook of Composite Graphite Materials], 1974.
- [3] Japan Special Report, Shaohe [Showa] 47-44940.
- [4] Rub. Chem. Techn., No 54, 1980 p 42.

### High-Temperature Silicon-Nitride Ceramic Developed

92P60004A Shanghai JIEFANG RIBAO in Chinese  
20 Jul 91 p 1

[Article by Jia Baoliang [6328 1405 5328]: "High-Temperature Silicon-Nitride Ceramic Material Developed in Shanghai"]

[Summary] Scientists from the CAS Shanghai Institute of Silicates for the first time have developed a high-temperature silicon-nitride ceramic able to maintain its strength up to a temperature of 1300°C. Testing conducted yesterday by specialists shows that its overall performance exceeds that of the comparable early-nineties-level international product; it therefore takes a leading place worldwide for such a material.

Developed as a priority project in the State "863" Plan, the new ceramic was exposed to a temperature of over 1200°C for 100 hours. The testing showed that it maintained its strength, while simultaneously keeping a high resistance to oxidation.

**Fujian Public Security Officials Distribute New MPS-Developed Anti-Computer-Virus Software***92P60022 Fuzhou FUJIAN RIBAO in Chinese 6 Sep 91 p 1*

[Article by Huang Shichi [7806 0099 3589]: "New Version of Computer-Virus-Elimination Software Distributed"]

[Summary] On the 2nd [of September], Fujian Province Public Security Department officials held a press conference to report on inspection and control of computer security in the province and to distribute copies of a new version of anti-computer-virus software [V35.01KILL] developed by the Ministry of Public Security (MPS). The new software, which can detect 506 different virus varieties and eradicate 35 different varieties, will effectively eliminate a number of virus varieties and their mutations recently discovered in China.

The officials noted that, in addition to several foreign-created computer viruses that have been introduced into the nation, they have also detected [home-grown] viruses, developed by lawless elements within China, that have attacked computer systems and destroyed data. The officials have determined that computer viruses are beginning to spread and have uncovered cases of computer fraud; they are therefore requiring all provincial government offices, all banking systems, and all civilian offices and firms engaged in the use, manufacture, sales, and/or maintenance of computers to closely cooperate in a new plan for computer security oversight. The new plan involves proper training of employees in computer security measures, promotion of MPS-approved measures [such as use of the new software] and development of new measures to detect and eradicate viruses, enhanced efforts at computer systems security at the management level, and efforts to prevent computer crime.

**Neural-Net-Based Handwritten-Chinese-Character Recognition System Certified***92P60006A Beijing JISUANJI SHIJIE [CHINA COMPUTERWORLD] in Chinese No 30, 7 Aug 91 p 1*

[Article by Han Yun [7281 0061] and Ge Cuiping [5514 5050 5493]: "New Breakthrough in Chinese Character Recognition: Artificial Neural-Network System Introduced"]

[Summary] At the request of the State S&T Commission, the Chinese Academy of Sciences (CAS) Division of Technical Science has certified the "handwritten-Chinese-character recognition method and system" developed as a State "863" High-Tech Plan project by the CAS Institute of Automation. This state-of-the-art system, based on over 8,000 identical artificial-neural-network elements, can recognize 3,050 different Chinese characters with an accuracy of 70-80 percent and an average speed of 45 characters per minute. The system runs on a 386 microcomputer.

**Sida-863A Spoken-Word Recognition System Unveiled***92P60006B Beijing JISUANJI SHIJIE [CHINA COMPUTERWORLD] in Chinese No 32, 21 Aug 91 p 1*

[Article by Du Yachun [2629 7161 2504]: "Nation's First Integrated General-Purpose Spoken-Word System Unveiled"]

[Summary] The "Sida-863A spoken-word system" jointly developed by the Beijing Sida [Star] Technology Development Center and Harbin Institute of Technology as a State "863 High-Tech Plan" priority project was certified by the State S&T Commission's High Technology Office on 9 August in Beijing. The Sida-863A (or Star-863A) system runs under any of a number of PC Chinese-character operating systems (such as CCDOS, Xishan DOS, and Great Wall DOS).

Tested with Chinese monosyllables spoken by selected individuals, the system had a one-time recognition accuracy of 87 percent in a quiet environment (background noise of 50 dB) and 86.9 percent in a noisy environment (background noise of 64 dB). When the system was permitted three revisions of a candidate sound, recognition accuracy increased to 97.6 percent and 93.7 percent in a quiet environment and noisy environment, respectively. The system's recognition accuracy for the four tones was 99.9 percent and 95 percent in the quiet and noise environments, respectively. Recognition speed is real-time. Tested with political, S&T, literary and fictional texts supplied and spoken by members of the research group, the system had a pinyin-to-Chinese-character conversion accuracy of 98.5 percent; for any type of text read aloud by the test group, the system had a pinyin-to-Chinese-character conversion accuracy of 87.7 percent. When specialized S&T texts alone were read aloud, the system had a spoken-word-to-Chinese-character conversion accuracy of 76.6 percent (in a noisy environment). Accuracy was 80 percent for news reports (in a quiet environment) and 89.4 percent for political-commentary texts (in a quiet environment).

**Fiber-Optic Computer Network Built at Yumen Oil Field***92P60006C Beijing JISUANJI SHIJIE [CHINA COMPUTERWORLD] in Chinese No 32, 21 Aug 91 p 7*

[Article by Chen Nan [7115 2809]: "Yumen Oil Field Completes Construction of Fiber-Optic Computer Communications Network"]

[Summary] The Chinese petroleum industry's first fiber-optic computer communications network has been completed at the Yumen Oil Field. The 2.5-km-long fiber-optic cable connects the oil field management's [previously existing] LAN with the oil field's computing center, equipped with a MicroVAX II host; specifically,

three previous networks—a 3+ net, a Novell net, and a DECnet—have now been interlinked via the fiber-optic cable. Equipment for the fiber-optic computer network includes FCN-3n optical terminals produced by the Chengdu Modern Electronics Plant and domestically manufactured fiber-optic cable. Transmission rate is 20 Mbps.

**Petroleum Institute Computing Center Gets Convex C120 Minisupercomputer**

*92P60006D Beijing JISUANJI SHIJIE [CHINA COMPUTERWORLD] in Chinese No 34, 4 Sep 91 p 2*

[Article by Yun Hai [0061 3189]: "Convex C120 Minisupercomputer Linked Into RIPER LAN"]

[Summary] Having the special approval of U.S. President Bush, a Convex C120 minisupercomputer was

linked into the RIPER Ethernet local area network (LAN) of the Petroleum Exploration and Development Scientific Research Institute's Computing Center on 22 August and put into formal operation. To be used for oil-reserves simulation and geophysical exploration, this is the fifth such computer imported by China to date. The others are used for weather forecasting research, scientific computation, and petroleum studies. The transaction was handled through the U.S. firm Convex Computer Company's overall China agent, Hong Kong Geotech Ltd.

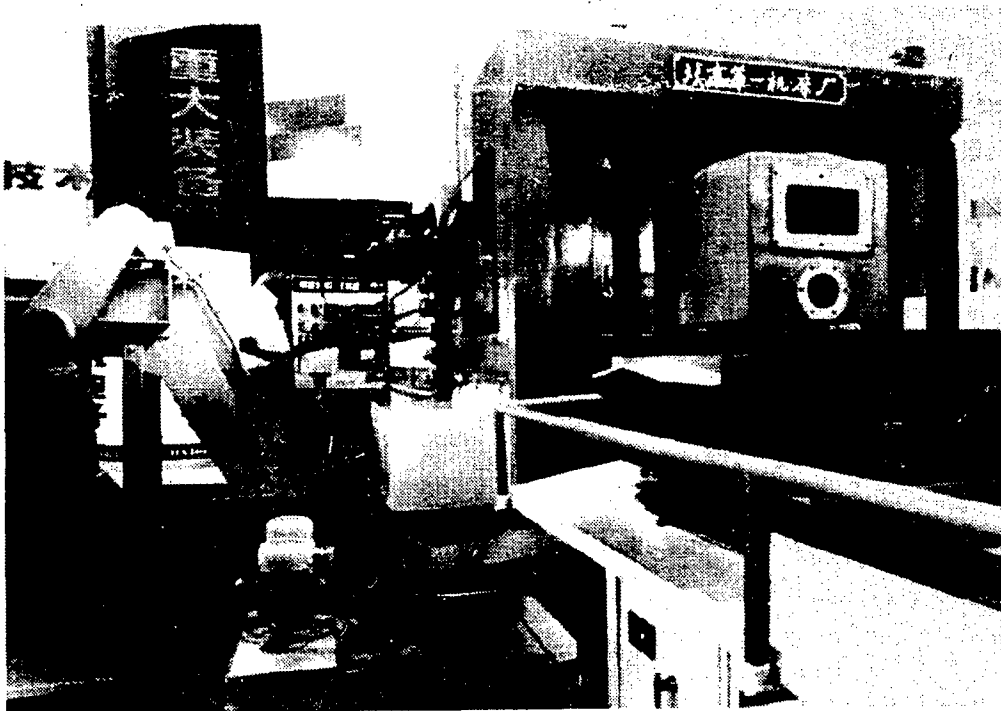
The C120 has an integrated vector/scalar operational structure, with a 64-bit word length, a peak operating speed of 16 MFLOPS, on-board memory of 256 Mbytes, and 1,000 Mbytes of disk memory.

**New Flexible Manufacturing Cell Developed**

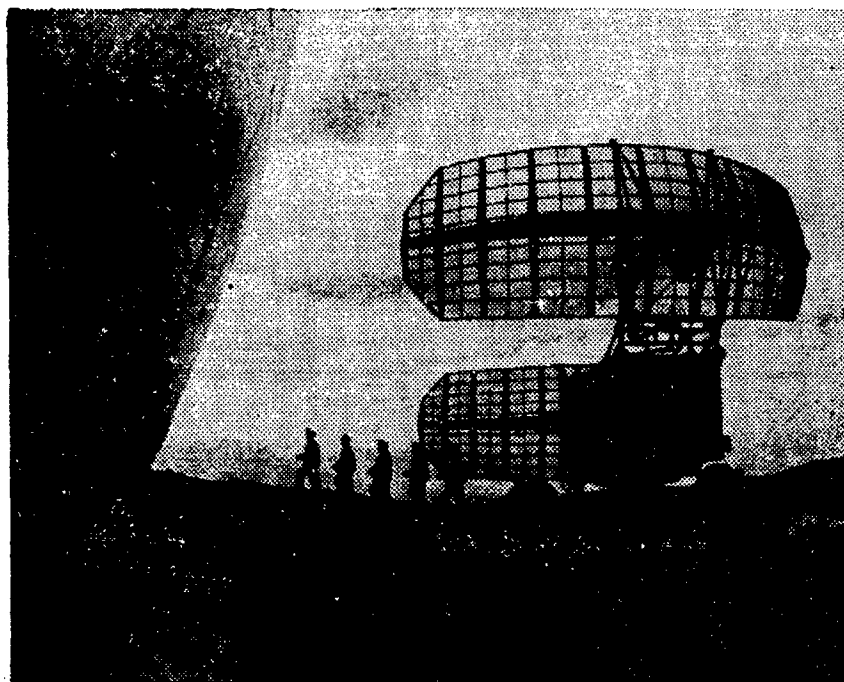
92P60005A Beijing KEJI RIBAO [SCIENCE AND TECHNOLOGY DAILY] in Chinese 24 Aug 91 p 1

[Untitled photoreport by KEJI RIBAO staff; photo by Wu Jinming]

[Text] The B<sub>1</sub>-FMC<sub>1</sub>-630 flexible manufacturing cell (FMC) developed as a State Seventh 5-Year Plan priority project by the Beijing No. 1 Machine Tool Plant has a six-position pallet-exchange apparatus and a mechanical-hand tool magazine. This high-precision, high-flexibility, high-productivity, highly automated machine tool meets mid-eighties international standards. [The accompanying photograph shows the new FMC.]



The B<sub>1</sub>-FMC<sub>1</sub>-630



A View of the Ganbala Radar Station

**Ganbala Radar Station Built by Air Force Unit**

92P60007A Chengdu *SICHUAN RIBAO* in Chinese  
18 Jun 91 p 1

[Untitled photoreport by You Cheng [0645 6134] to accompany photo by Sun Li]

[Summary] A Chengdu-based Air Force unit temporarily stationed in the Tibetan capital [i.e., Lhasa] has overcome numerous logistical difficulties in its completion of renovations to the 5,375-meter-high Ganbala radar station. High-grade intelligence rate has risen to over 98 percent for this station, which provides a major contribution to aircraft communications in Tibet. [The photograph shows the Ganbala radar station.]

**Airborne SAR Remote Sensing System Used To Survey Flood Damage**

92P60007B Beijing *KEJI RIBAO* [*SCIENCE AND TECHNOLOGY DAILY*] in Chinese 30 Jul 91 p 1

[Article by Yue Ziqiang [2867 1311 1730]: "Radar Remote Sensing Serves in Flood-Damage Assessment"]

[Summary] An aircraft flying out of the Shanghai Airport recently completed an 11,000-meter-altitude aerial survey of flood damage in the Suzhou-Wuxi-Changzhou area, especially around the Tai Hu feeders. This was the first "combat" use of a multistrip, multiple-polarization side-looking synthetic aperture radar (SAR) with a ground resolution of 10m x 10m. Numerous multistrip photographs were taken of a 50,000-square-kilometer

area on three separate flights totaling nine hours; the data has proven invaluable in assessing flood damage in this region.

**33fs Pulse Generation Via Mixed Dye Saturable Absorber**

92P60007C Shanghai *ZHONGGUO JIGUANG*  
[*CHINESE JOURNAL OF LASERS*] in Chinese Vol 18  
No 7, Jul 91 pp 523-526

[Article by Lin Weizhu [2651 0143 2701], Qiu Zhiren [8002 1807 0088], Xu Wencheng [1776 2429 2052], and Huang Zuozhu [7806 0155 2691] of the Institute of Lasers and Spectroscopy, Zhongshan University, Guangzhou: "33fs Pulse Generation by Using Mixed Dye Saturable Absorber"; project funded by NSFC, MS received 4 Oct 89]

[Abstract] Pulses with a FWHM of 33 femtoseconds (fs) have been generated from a colliding-pulse mode-locked (CPM) ring-type Ar<sup>+</sup> laser using a hybrid dye saturable absorber made from a  $3 \times 10^{-4}$  Mol concentration of DODCI (diethyloxadicarbocyanine iodide) and a  $1 \times 10^{-5}$  Mol concentration of MG (malachite green). Laser-pulse center wavelength is 630 nm, and the laser operated in the TEM<sub>00</sub> mode. The physical arrangement is shown in Figure 1 below, while three other figures [not reproduced] depict autocorrelation traces and absorption spectra.

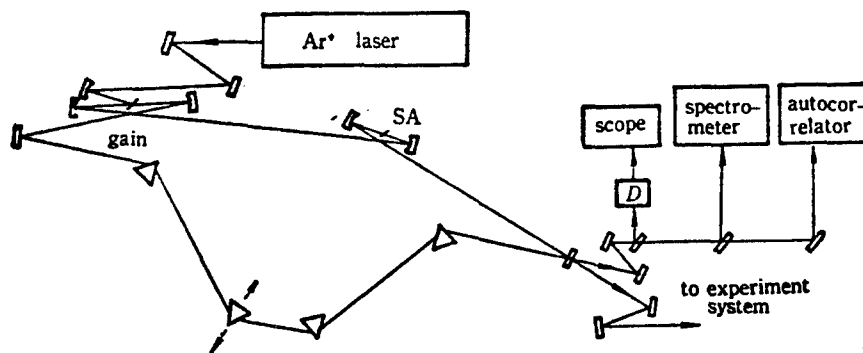


Figure 1. Schematic of the Six-Mirror Ring Cavity Incorporating a Four-Prism Sequence CPM Dye Laser

### References

1. J. A. Valdmanis et al., OPT. LETT., 10 (3), 131 (1985).
2. E. P. Ippen et al., CHEM. PHYS. LETT., 38, 611 (1976).
3. A. Watanabe et al., IEEE J. QUANT. ELECTR., QE-19 (4), 533 (1983).
4. D. Kuhlke et al., IEEE J. QUANT. ELECTR., QE-19 (4), 526 (1983).
5. H. A. Haus, IEEE J. QUANT. ELECTR., QE-11 (9), 736 (1975).
6. J-C. M. Diel et al., APPL. OPT., 24 (9), 1270 (1985).
7. M. J. Rosker et al., PHYS. REV. LETT., 57 (3), 321 (1986).
8. A. Penzkofer, APPL. PHYS., B 46, 43 (1988).
9. D. N. Dempster et al., J. CHEM. SOC. FARADAY II, 68, 1479 (1972).
10. O. E. Martinez et al., J. OPT. SOC. AM., B 2 (5), 753 (1985).

### First Fully Mobile, High-Accuracy CW Tracking Radar System Unveiled

92P60007D Beijing ZHONGGUO DIANZI BAO  
[CHINA ELECTRONICS NEWS] in Chinese 2 Aug 91  
p 3

[Article by Wang Junhong [3769 6511 1347]: "New-Generation Continuous-Wave Highly Mobile Measurement Station Goniometric System Unveiled"]

[Summary] The high-accuracy CW mobile-tracking-station goniometric system developed by MMEI's Institute 39 recently passed acceptance check in Xian, and is now undergoing trial operation in the full radar system. This goniometric system is critical vehicle-borne equipment for the nation's new-generation fully

mobile, high-accuracy CW tracking radar. The full system meets mid-to-late-eighties international standards.

### Central China University Develops 10kW-Class CO<sub>2</sub> Laser

92P60007E Beijing ZHONGGUO DIANZI BAO  
[CHINA ELECTRONICS NEWS] in Chinese 4 Aug 91  
p 1

[Untitled XINHUA photoreport, photo by Yu Dengjian]

[Summary] Scientists at Central University of Science and Technology's Laser Institute have developed a 10kW-class high-power CO<sub>2</sub> laser. The accompanying photo depicts the researchers conducting tests on the new high-power laser.

### Radar-Oriented Bulk Acoustic Wave Delay Line Developed

92P60007F Beijing ZHONGGUO DIANZI BAO  
[CHINA ELECTRONICS NEWS] in Chinese 4 Aug 91  
p 3

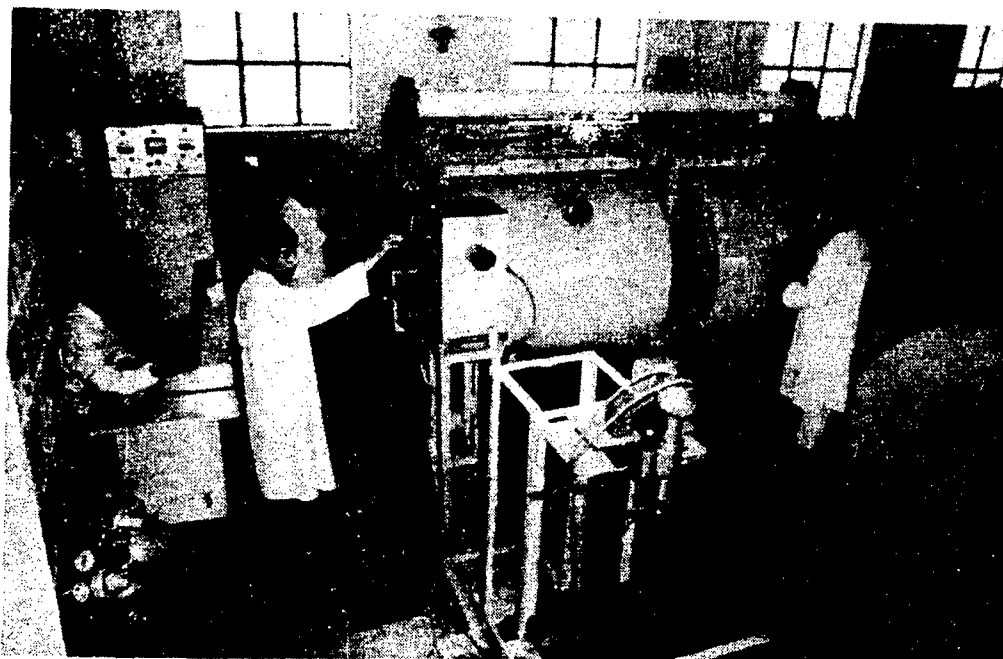
[Untitled photoreport, photo by Jiang Guangchao and Feng Jintang]

[Summary] Scientists at MMEI's Institute 26 have developed a range zero-adjustment device (called a bulk acoustic-wave delay line) for a subminiature fire-control radar. The accompanying photo shows a representative from the National Defense Science, Technology and Industry Commission [NDSTIC] listening to a detailed explanation of the device from an institute radar specialist.

### 300,000-Pixel Frame-Transfer CCD System Unveiled

92P60007G Beijing ZHONGGUO DIANZI BAO  
[CHINA ELECTRONICS NEWS] in Chinese  
11 Aug 91 p 3

[Article by Yang Yasheng [2799 0068 3932]: "300,000-Pixel Large-Surface-Array CCD Camera Developed"]



[Summary] MMEI's Institute 44 has developed a 600-pixel-by-500-pixel large-surface-array visible-light frame-transfer charge-coupled device (FTCCD) camera. Following upon the institute's realization of 491x384-bit and 756x581-bit large-surface-array interline-transfer

CCD cameras last year, the appearance of the new FTCCD camera represents a major step forward in development of imaging devices.

The new camera consists of a light-sensitive region, a temporary-storage area, a horizontal shift register, and



an output circuit; it has a three-phase three-layer polycrystalline-silicon overlapping-gate structure. The horizontal shift register is a buried-channel CCD. The output incorporates a floating diffusion source follower amplifier. Applications of the new FTCCD camera include target tracking, high-image television, character recognition, information display, medicine, and scientific research.

#### **Dual-Wavelength Nd:YAL Laser Unveiled**

92P60007H Beijing ZHONGGUO KEXUE BAO  
[CHINESE SCIENCE NEWS] in Chinese 30 Aug 91  
p 1

[Article by Yang Yongtian [2799 3057 3944] and Yang Zhaoliang [2799 6856 5328]: "CAS Fujian Institute of Material Structure Develops First Dual-Wavelength Neodymium-Doped Yttrium-Aluminate Laser"]

[Summary] Four major new devices developed by the CAS Fujian Institute of Material Structure recently passed appraisal in Beijing. The new devices include a neodymium-doped yttrium-aluminate (Nd:YAL) dual-wavelength (1.0795  $\mu\text{m}$  and 1.3414  $\mu\text{m}$ ) CW laser with an output power of 33.7W and 30W at the two wavelengths, respectively; this achievement has set a world record. Also included is a Nd:YAL pulsed laser. Applications of multi-wavelength lasers—one of the hottest

subjects of international study—include precision laser spectroscopy, resonance holographic interferometry, optical radar, and laser medical treatment.

#### **Shanghai Scientist Develops State-of-the-Art Liquid-Crystal Light Valve**

92P60007I Tianjin ZHONGGUO JISHU SHICHANG  
BAO [CHINA TECHNOLOGY MARKET NEWS]  
in Chinese 4 Sep 91 p 1

[XINHUA photoreport (photo by Wang Zijin): "Zhuang Songlin Develops 'Liquid-Crystal Light Valve'"]

[Summary] Dr. Zhuang Songlin [8369 2646 2651], director of the Shanghai Optical Instruments Institute and of the Shanghai Institute of Laser Technology, has developed a state-of-the-art high-tech electronic device called a "liquid-crystal light valve," for which foreign orders have already been placed and production begun. Since his return in 1982 from graduate studies in the United States, Dr. Zhuang (shown at right in the accompanying photograph), an internationally recognized member of SPIE (the International Society for Optical Engineering), has made numerous contributions to the development of the domestic optical industry in areas such as computer imagery analysis and missile laser guidance.



### Stimulated Raman Scattering in Single-Mode Fiber and the Walkoff Between Pumping and Raman-Stokes Pulses

91FE0721 Shanghai GUANGXUE XUEBAO [ACTA OPTICA SINICA] in Chinese Vol 11, No 6, Jun 91 pp 481-486

[Article by Fan Liming [2868 4539 2494], Wang Shijie [3769 0013 2638], Li Shiyang [2621 1102 5391], Chen Shisheng [7115 2514 0524], and Xu Zhizhan [1776 5267 1455] of the Chinese Academy of Sciences Shanghai Institute of Optics and Fine Mechanics, P.O. Box 800-211, Shanghai 201800; manuscript received 19 Oct 90]

[Text] Abstract: This article reports the results of experiments on stimulated Raman scattering [SRS] in single-mode optical fibers and the use of a streak camera to measure the relative delay time of pumping pulses and Raman-Stokes pulses. The results show that Raman-Stokes pulses from SRS formed at a location about one walkoff length from the input end of the fiber.

Key terms: optical fiber, self-phase modulation, stimulated Raman scattering.

#### I. Introduction

Since the discovery by Woodbury and Ng of stimulated Raman scattering of light in a nitrobenzene Kerr box in 1962, people have conducted research on SRS in different media. Because a relatively high laser power density can be obtained over a rather long length of fiber, quartz optical fibers have gradually become an extremely effective measure for research on SRS and other nonlinear processes. Although people are still extremely unclear at present regarding the active mechanisms in SRS, SRS in fibers can still be used to create coherent infrared radiation and to make Raman lasers.

When laser pulses are transmitted through fibers, they are affected by three main factors: self-phase modulation, stimulated Raman scattering, and group velocity dispersion. Self-phase modulation causes spreading of the pumping laser spectra and, when fitted with a pair of gratings under appropriate conditions, compression of ultra-short laser pulses can be achieved<sup>[1,2]</sup> to obtain femtosecond laser pulses. SRS can create coherent laser pulses at new wavelengths and some have already observed Stokes pulses as high as 10 steps<sup>[3]</sup>. Group velocity dispersion can cause reforming of pumping pulse waveforms and spatial walkoff of pumping pulses and Stokes pulses<sup>[4,5]</sup>, so group velocity dispersion is extremely unfavorable for optical communications. Schadt et al. have analyzed self-phase modulation of Stokes pulses and pumping pulses. Stolen et al. have observed pulse walkoff and self-phase modulation of Stokes pulses in fibers, but we have seen no cases of relatively precise measurement of this using a streak camera.

This project used different lengths of single-mode fibers and an Nd:YAG primary passive colliding mode-locking

laser frequency doubler laser pulse pump along with a streak camera to study SRS of laser pulses with a wavelength of 532 nm and a pulse width of 40 ps and the walkoff of pumping pulses and Stokes pulses.

#### II. Experimental Setup

The setup used in the experiment was similar to the setup used to study self-phase modulation in fibers<sup>[6]</sup>, as shown in Figure 1. The 50 ps sequence of pulses generated by the primary passive colliding mode-locking Nd:YAG laser passed through a single-pulse selecting switch which selects a single pulse from the sequence that is then coupled to the fiber after amplification (not shown in the illustration) and frequency doubling. In the experiment, a 1 m grating spectrograph was used to observe and photograph the pulsed laser's SRS high resolution spectra. The spectrograph's line dispersion was 0.74 Å/mm. A fast photodiode and high-frequency oscilloscope were used to monitor variations in pulse energy and the quality of single pulse selection. A 1.064 μm total reflection lens with an S of 45° was used to eliminate the effects of 1.064 μm laser pulses on SRS. Two types of fibers were used in the experiments. One was a 2 meter-long single-mode polarization-preserving visible light fiber. The fiber had a core diameter of 4 μm and the fiber coupling efficiency was 20 percent. The other type was infrared single-mode fiber 10 m and 20 m in length. This fiber had a core diameter of 8 μm and the fiber coupling efficiency was 30 percent.

#### III. Experimental Results and Analysis

##### A. Stimulated Raman scattering in the short fiber

Figure 2 shows the single pulse waveform input into the fiber. The typical half-height width (FWHM) was 40 ps. Figure 3 shows the SRS spectra in the single-mode polarization-preserving fiber. The spectrum at the left side of the figure corresponds to the pumping laser pulses. The spectrum spread is due to self-phase modulation in the fiber, whereas the threshold value of SRS is comparatively higher. When the laser power density in the fiber is higher than the threshold value of SRS, we observed SRS with a Raman frequency shift of 440 cm<sup>-1</sup>. The Raman conversion efficiency at this time is relatively low, as shown in Figure 3(a). Figures 3(b) and 3(c) show the results when the laser power coupled into the fiber is increased. The Raman conversion efficiency is higher than 50 percent in both cases. Under conditions of higher pumping laser power, energy envelopment effects appeared in the pumping pulses<sup>[6]</sup>, so that subsequent increases in the energy converted nearly all of them into SRS.

No obvious pulse walkoff was observed in the 2 meter-long fiber. The distance  $l_{wo}$  in the fiber required for laser pulse walkoff was<sup>[4]</sup>:

$$l_{wo} = T \times C \times v / [D(\lambda) \times \Delta v]. \quad (1)$$

In the equation,  $\Delta v$  is the frequency difference between the pumping laser pulses and Raman-Stokes pulses,  $v$  is

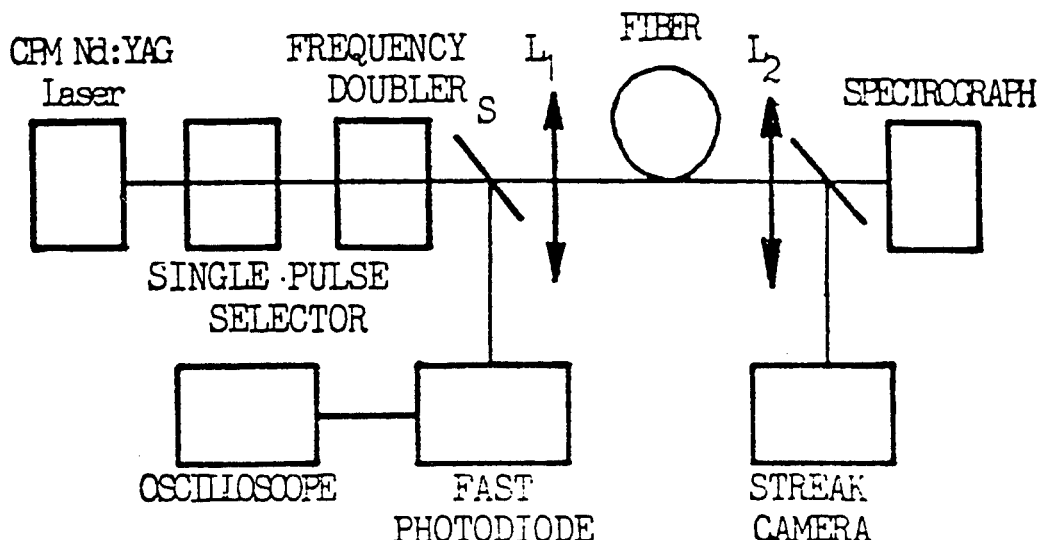


Figure 1. Experimental Setup

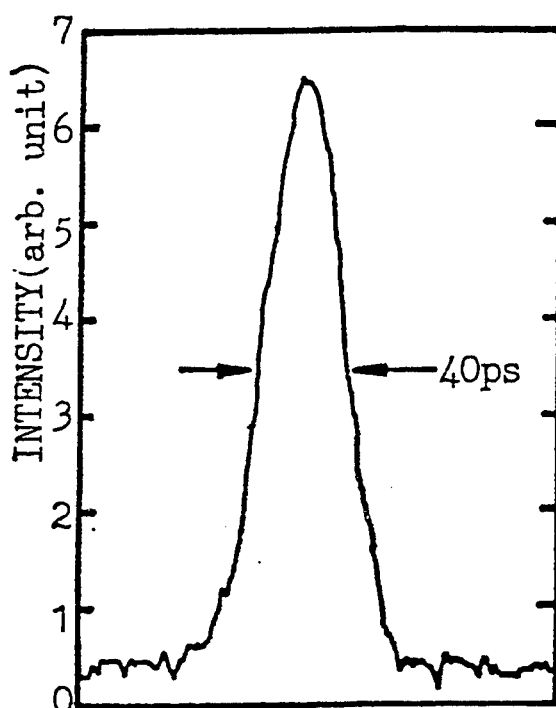


Figure 2. Envelopement of Single Pulse Coupled Into the Single-Mode Fiber. Pulsewidth (FWHM) 40 ps

the average frequency of the laser,  $T$  is the width of the pumping pulses, and  $D(\lambda)$  is the dispersion in the fiber. For a 5320A pumping laser,  $\nu/C = 18,577 \text{ cm}^{-1}$ ,  $D(\lambda) = 0.073$ , and  $\Delta\nu = 440 \text{ cm}^{-1}$ . For 40 ps laser pulses, the walkoff length of Raman-Stokes pulses and pumping pulses was 6.94 m. The fiber used in the experiment was

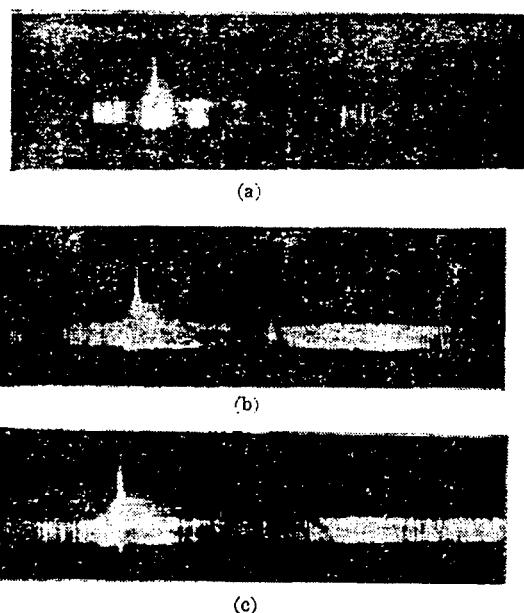
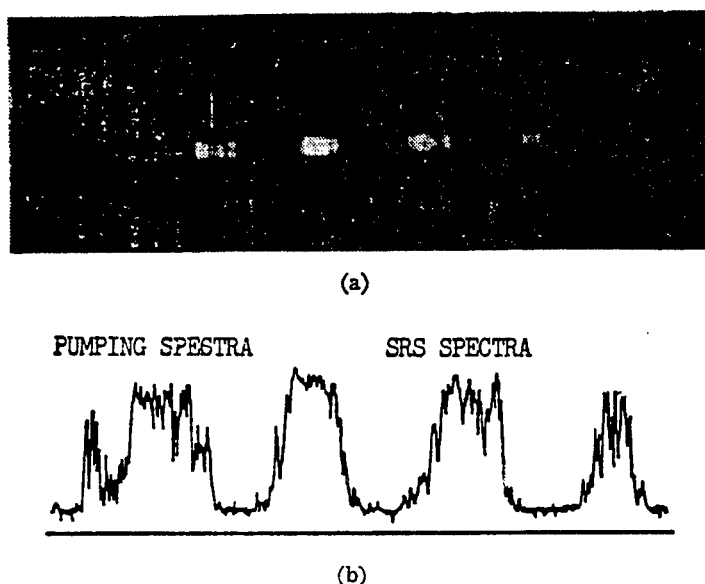


Figure 3. High Resolution Spectra of Stimulated Raman Scattering in a 2 Meter-Long Single-Mode Polarization-Preserving Optical Fiber. The Energy Coupled Into the Optical Fiber Increased From Fig. (a) to Fig. (c)

rather short and the effects of group velocity on transmission of the laser pulses in the fiber were rather small.

#### B. Walkoff of pumping pulses and Raman-Stokes pulses

We used 10 m and 20 m fibers to study SRS and the spatial walkoff of pumping pulses and Stokes pulses



**Figure 4. High Resolution Spectra of Stimulated Raman Scattering in a 20 Meter-Long Single-Mode Optical Fiber**  
Key: (a) Photograph of stimulated Raman scattering spectra and pumping pulse (b) Density trace of Figure 4(a)

transmitted through the fiber. Figure 4 shows typical SRS spectra in the 20 m fiber (the SRS spectra in the 10 m fiber were completely analogous). Figure 4(a) is a photograph of the spectra and Figure 4(b) is the corresponding density trace. The figures show that the pumping laser creates two-stage SRS in the fiber and the corresponding Raman frequency shifts are  $240\text{ cm}^{-1}$ ,  $442\text{ cm}^{-1}$ , and  $682\text{ cm}^{-1}$ . Unlike the single-mode polarization-preserving fiber, SRS with a frequency shift of  $240\text{ cm}^{-1}$  was observed. This may be related to the fiber manufacturing process or to the size of the Raman gain of this frequency shift in the polarization-preserving fiber that was not measured.

After the pumping laser creates Raman-Stokes pulses in the fiber, because of group velocity dispersion, after passing along the  $\Delta L$  transmission distance, the Stokes pulses become spatially separated from the pumping laser pulses and cause a time delay  $\Delta t$ :

$$\Delta t = \Delta L \times D(\lambda) \times \Delta v / (C \times v). \quad (2)$$

For a given fiber length, the measured pulse delay  $\Delta t$  can be used to determine the location of Raman-Stokes pulses formed in the fiber.

Figure 5 is the measured results for the 20 m fiber at different input powers. In Figure 5(a), the pumping laser pulses only create Raman-Stokes pulses with a frequency

shift of  $240\text{ cm}^{-1}$ . In Figure 5(b), walkoff of Stokes pulses with frequency shifts of  $240\text{ cm}^{-1}$  and  $442\text{ cm}^{-1}$  from the pumping pulses was observed. Figures 5(c) and 5(d) correspond, respectively, to the situation for 3 and 4 Stokes pulses. In SRS, the first Stokes pulse created will serve as a pumping source for the next higher level of Stokes pulses. The experimental results indicate that Stokes pulses with a frequency of  $240\text{ cm}^{-1}$  lead pumping pulses by 66 ps, while Stokes pulses with a frequency shift of  $440\text{ cm}^{-1}$  lead by 122 ps, as shown in Figure 5(c). The corresponding fiber length required to generate pulse leading is derived from equation (2):  $\Delta L_1 = 20.9\text{ m}$  and  $\Delta L_2 = 21.2\text{ m}$ , as shown in Table 1. Obviously,  $\Delta L_1$  and  $\Delta L_2$  are both greater than the total length of the fibers used in the experiments, whereas Stokes pulses cannot be created before entering the fiber. The experimental results show<sup>[4]</sup> that Raman-Stokes pulses are actually created about one pulse width ahead of the pumping laser pulses. Thus, reasonable estimates of the location where Raman-Stokes pulses are created should be made by subtracting the corresponding pulse walkoff length  $l_{wo}$  from  $\Delta L_1$  and  $\Delta L_2$ . From this, the location where amplified Stokes pulses with Raman frequency shifts of  $240\text{ cm}^{-1}$  and  $442\text{ cm}^{-1}$  are formed from the end of the fiber are, respectively, 11.8 m and 5.6 m. In conjunction with the results shown in Table 1, this permits the following conclusion to be drawn: SRS Raman-Stokes pulses are formed at a location about one walkoff length from the input end of the fiber.

**Table 1.**

$\Delta v(\text{cm}^{-1})$	$\Delta t(\text{ps})$	$\Delta L(\text{m})$	$l_{wo}(\text{m})$	$\Delta L'(\text{m})$	$L_S$
240	65.8	20.9	12.7	8.2	11.8
442	122.2	21.2	6.9	14.3	5.6

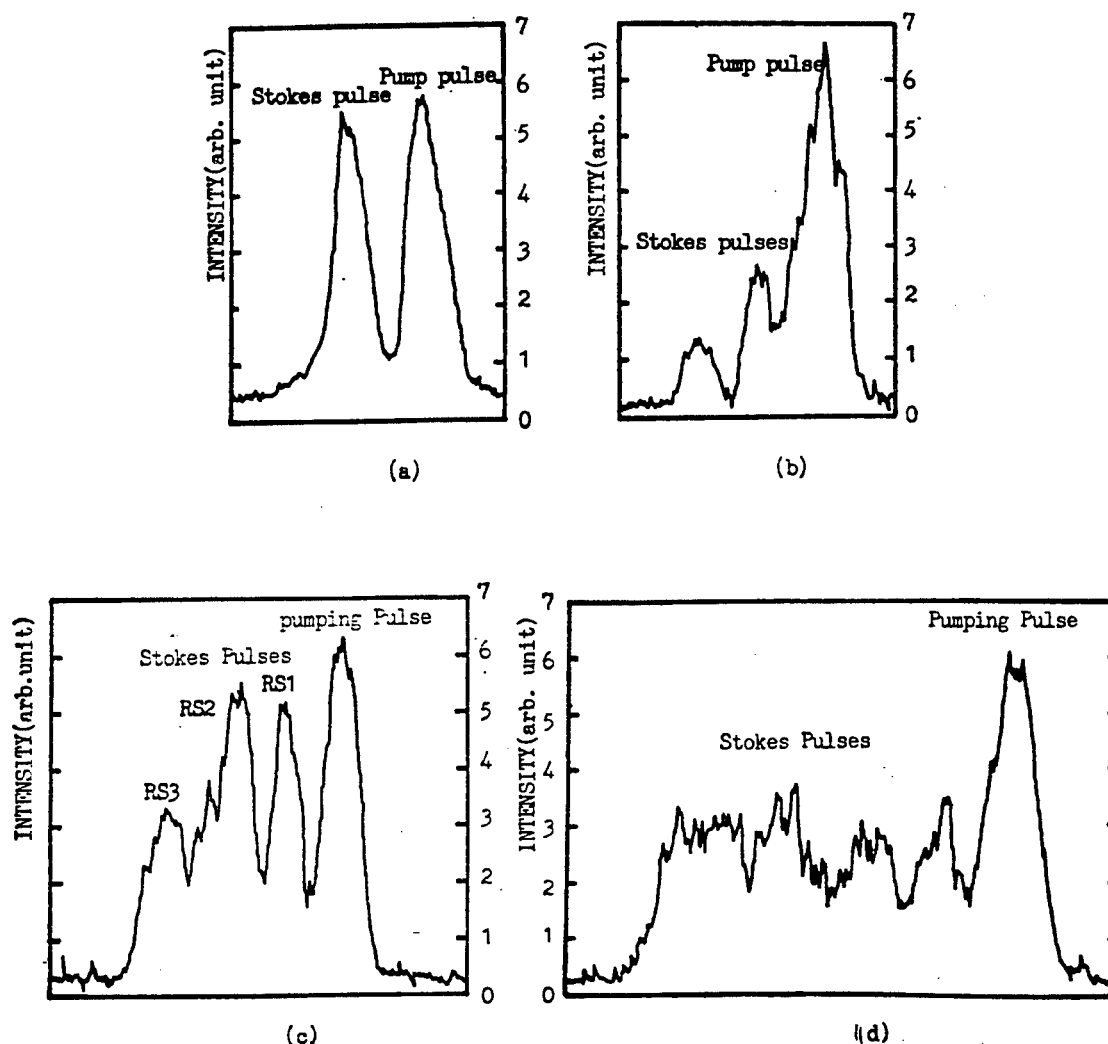


Figure 5. Envelopment of Output Pulses From a 20 Meter-Long Single-Mode Optical Fiber Measured by a Streak Camera With a Time Resolution of 10 ps

As for the Stokes pulses in Figure 5(c), RS3 is actually the result of coherent superimposition of Raman-Stokes pulses created after the RS1 frequency shift of  $442\text{ cm}^{-1}$  and RS2 frequency shift of  $240\text{ cm}^{-1}$ . As for Raman-Stokes pulses during the RS1 frequency shift of  $240\text{ cm}^{-1}$ , because they are approximately the same as the RS2 Raman frequency shifts, and because RS2 itself has very strong self-phase modulation, they are very hard to differentiate in spectral and temporal terms.

Figure 6 shows the output laser pulses of the 10 m fiber. At an input laser pulse width of 20 ps and a pumping pulse delay of 47 ps, the estimated location of Raman-Stokes pulse formation is 7.6 m from the input end of the fiber, which is approximately equivalent to the pulse walkoff length of 6.4 m, so the results are basically identical to those for the 20 m fiber.

#### IV. Conclusion

This project involved experimental research on laser SRS in single-mode optical fibers of different lengths. The results of the experiments permit the following conclusions to be drawn:

1. Stimulated Raman scattering Stokes pulses in the fibers form at a location about one walkoff length from the input end of the fiber. Subsequent transmission of the laser pulses in the fibers caused walkoff of the pumping laser pulses and the Stokes pulses.
2. Stimulated Raman scattering with Raman frequency shifts of  $240\text{ cm}^{-1}$  and  $442\text{ cm}^{-1}$  was observed in the single-mode fibers. SRS with a frequency shift of  $240\text{ cm}^{-1}$  was not seen very often in the fibers.
3. Using the relative delay times of the pumping pulses and Stokes pulses in the fibers based on equation (2) can

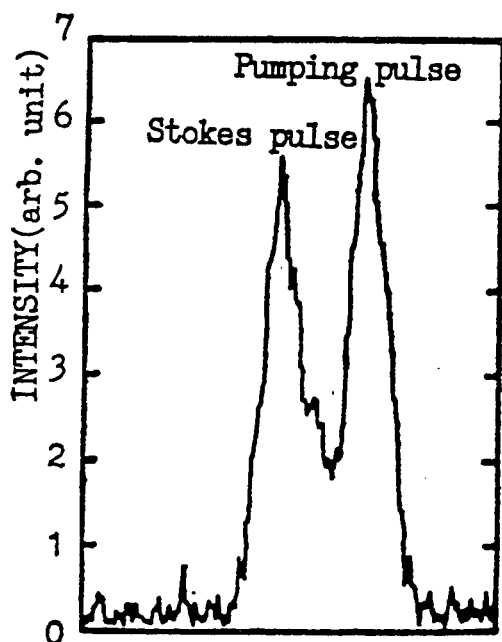


Figure 6. Envelopment of Output Pulses From a 10 Meter-Long Single-Mode Optical Fiber Measured by a Streak Camera With a Time Resolution of 10 ps. Pumping Pulsewidth (FWHM) Was 20 ps

permit measurement of dispersion and other parameters in the fibers, which is extremely favorable for liquid core fibers.

Zhu Guoying [2612 0948 5391], Lu Haihe 7120 3189 7729], and other comrades also participated in this research project. The single pulse switch used in this experiment was provided by comrade Mang Yanping [5462 3601 5493] at the Chinese Academy of Sciences Shanghai Institute of Optics and Fine Mechanics, and we would like to express our gratitude. The authors would also like to thank comrade Zhu Qingchun [4555 1987 2504] of the Institute's Integrated Laboratory for his assistance in the streak camera measurements.

#### References

- [1] A. S. Gouveia-neto, et al., Opt. Comm., Vol 64, No 2, 1987 pp 163-166.
- [2] Fan Liming [2868 4539 2494], et al., Guangxue Xuebao [Acta Optica Sinica], Vol 11, No 5, May 1991, pp 385-389.
- [3] Gaopei Juan, et al., Applied Physics, Vol 24, 1981, pp 303-306.
- [4] R. H. Stolen, et al., IEEE Journal of Quantum Electronics, QE-22, No 11, Nov 1986, pp 2150-2160.
- [5] Dieter Schadt, et al., Journal of the Optics Society of America (B), Vol 3, No 10, Oct 1986, pp 1257-1262.

[6] Fan Liming, et al., Guangxue Xuebao, Vol 11, No 2, Feb 1991, pp 161-165.

#### Coming Ten Years of Environmental Remote Sensing in China

40100084A Beijing HUANJING YAOGAN [REMOTE SENSING OF ENVIRONMENT] in Chinese Vol 6 No 3, Aug 91 pp 163-168

[English abstract of article by Chen Shupeng of the Institute of Remote Sensing Application, CAS]

[Text] To congratulate [colleagues] on the tenth anniversary of China's Environmental Remote Sensing Committee, Professor Chen Shupeng has pointed out at the Symposium on Remote Sensing Developing Trends and Research Front in the 1990s that remote sensing technique had been listed as a national key project twice in the past 10 years. Encouraging progress has been made since then. Remote sensing information has been popularized gradually with applications in economic construction and national defense. New applied fields have also been developed and distinct social and economic benefits have been achieved. A new service trade of high technology and information has been preliminarily formed. It has started to arouse attention in academic circles in both the Asian-Pacific region and [elsewhere in] the world.

In the coming 10 years, during which Chinese government will implement its 10-Year Program, remote sensing technique has been listed as a key project in the Eighth 5-Year Plan again. Professor Chen Shupeng has consulted with 32 professors and experts on remote sensing developing trends in the 1990s in China. Several major points can be concluded as follows:

(1) The development and application of meteorological satellite information will reach its climax once again. Relatively sufficient preparation on theory, methodology and technology has been made in the past 10 years; and successful experience with launching of the Fengyun-1 [FY-1] satellites has been achieved. The disadvantages needed to be avoided have also been found. Thus, in the coming 10 years, as one of the major information sources in environmental remote sensing, meteorological satellites will play a vanguard role in natural disaster monitoring, crop-yield estimation and study of global environment change.

(2) With regard to resource satellite remote sensing, the ground receiving station built by China has achieved successful operation experiences, and has developed and improved the function of receiving data and images from various satellites. In the 1990s, in the sky of the Asian and Pacific region, there will be five kinds of international remote sensing satellites, i.e., Landsat-7, MOS, JERS, SPOT and ERS-1. The information sources will be very rich. The resource satellites cooperatively built by China and Brazil will also join them in the middle 1990s. They are expected to provide real-time assurance for information sources after the establishment of a

remote sensing information system for natural disaster monitoring and crop yield estimating.

(3) Airborne remote-sensing technique has made great progress in the past 10 years. Breakthroughs both in design and application of airborne imagery spectrometers, multiply polarized side-looking radar, microwave radiometers and light aircraft; and on all-weather, information transmission and digital image processing have been made. Stable and continuous development in urban planning and management, mineral deposits and petroleum field exploration, manufactory sites, power-station selection, and disaster prevention, etc. will be realized. Especially, these will be used to meet the urgent needs for investment environmental evaluation in open cities.

(4) The equipment potentiality and technical progress made in the past 10 years should be fully used in the key projects of the Eighth Five-Year Plan. Two strategic targets, "natural disaster prevention and harnessing" and "crop-yield estimation", should be taken as subjects so as to compose an integrated technical system of a fairly intelligent level; and to have functions of great storage capacity, real-time transmission and quick processing.

(5) China should continue participating in the international cooperation program taking global study as a target, and contribute active efforts to the Ten-Year International Disaster Reduction, the International Space Year and the International Geosphere-Biosphere Program, etc.

**CAS Optoelectronics Institute Develops  
Chip-Fabrication Optical Equipment**

92P60008A Beijing KEJI RIBAO [SCIENCE AND  
TECHNOLOGY DAILY] in Chinese 5 Aug 91 p 1

[Article by Deng Xianchun [6772 6343 2504] and Zheng Tianfen [6774 3944 5358]: "Rapid Research Advances in [Development of] Special-Purpose Microelectronics Equipment"]

[Summary] The CAS Institute of Optoelectronics Technology has developed several types of optical equipment specially used for fabrication of ICs, and is one of the major centers that will provide such equipment to the domestic microelectronics industry in the Eighth 5-Year Plan. This institute, which has four research labs and over 100 scientists and engineers, has developed the nation's first semiautomatic proximity/contact-type optical lithography unit (the model JK-1), a laser positioning platform for a variable-rectangle electron-beam exposure machine, a step-and-repeat projection optical lithography machine (direct-step-on-the-wafer, or DSW), an automatic inspection system for mask defects, a synchrotron-radiation X-ray lithography system, and three other similar devices. Of these, the automatic mask-defect inspection system can detect over 99 percent of defects in silicon wafers for 1.5-micron-and-larger ICs. The X-ray lithography system has already been installed and debugged at the Beijing Electron-Positron Collider's Synchrotron Radiation Laboratory. The step-and-repeat projection lithography unit, which passed national-level acceptance check in the first half of this year, has a limiting resolution of 0.8 micron, an alignment accuracy of better than  $\pm 0.35$  micron, and a productivity of 39 wafers per hour. The development of this unit indicates China has begun to master DSW fabrication techniques as well as 2-micron-and-lower production technology.

**Silicon-Gate CMOS PLL Frequency-Synthesizer  
IC Developed**

92P60008B Beijing ZHONGGUO DIANZI BAO  
[CHINA ELECTRONICS NEWS] in Chinese  
11 Aug 91 p 3

[Article by Yao Jingping [1202 0079 1627]: "New Silicon-Gate Phase-Locked-Loop Frequency-Synthesizer Circuit Fabricated"]

[Summary] The BJ145146 silicon-gate CMOS phase-locked-loop (PLL) frequency-synthesizer IC jointly developed by the Beijing Electron Tube Plant, the Qinghua University Radio Department, and the CAS Microelectronics Center has passed technical appraisal. This device, widely used in radio and mobile communications equipment, has seven DC parameters which fully comply with the international MC145146 standard. Of these DC parameters, the value for [drain] cutoff current ( $I_{DD} = 90 \mu A$ ) is lower than that of foreign samples. This IC can fully replace the MC145146.

**Motorola To Invest \$200-400 Million in Tianjin  
in Next Decade**

92P60008C Beijing JISUANJI SHIJIE [CHINA  
COMPUTER WORLD] in Chinese No 31, 14 Aug 91  
p 2

[Unattributed article: "U.S. Motorola Corp. To Invest in Construction Project in Tianjin Development Zone"]

[Summary] (XINHUA)—Representatives of Motorola Inc. recently concluded an agreement with the Tianjin Economic and Technical Development Zone (TETDZ) involving investment in a 100,000-square-meter TETDZ construction project. According to the plan, Motorola within the next 10 years will invest \$200-400 million in the project. First-phase investment, totaling \$40 million, will go for construction of an LSI production plant; this will be followed by construction of a communications equipment plant, an automotive electronic parts plant, a semiconductor devices plant, and a telephone equipment plant.

**Electroluminescent Flat Panel Display Developed**

92P60008D Beijing ZHONGGUO KEXUE BAO  
[CHINESE SCIENCE NEWS] in Chinese 27 Aug 91 p 1

[Article by Jia Jinlin [6328 3160 2651]: "New Display Developed"]

[Summary] A new solid-state flat panel display (FPD)—a type called a thin-film electroluminescent display—has been developed by Tianjin Institute of Science and Engineering. This type of display, which directly converts electrical energy into optical energy, can be used in industries such as aerospace, defense (tactical vehicles and warships), broadcasting, and computers. This type of FPD, which has a novel three-level or three-layer structure, has advantages over other types such as the LCD, plasma display, and LED display.

**Status of IC R&D Described**

92P60008E Beijing ZHONGGUO DIANZI BAO  
[CHINA ELECTRONICS NEWS] in Chinese 6 Sep 91 p 3

[Article by Professor Wang Yangyuan [3769 7122 0337] of Beijing University: "Status, Development Strategy for Nation's IC Technology"]

[Excerpt] [Passage omitted] In the past decade, Chinese researchers have developed almost 2,000 varieties of ICs. Already put into production are 2,000-gate CMOS gate arrays, 800-1,200-gate ECL gate arrays, and 16-bit microcomputer ICs. Complete fabrication technology for 1-1.5-micron VLSI circuits is in its early phase. During the Eighth 5-Year Plan, 1-1.5-micron standard technology will be perfected, and large-scale production of 1-micron VLSIs and ASICs will be initiated. Submicron VLSI research, already begun, will be continued; efforts will concentrate in areas such as soft-X-ray exposure, electron-beam exposure, reactive ion etching technology, and thin-film development. R&D bases for



research on GaAs ICs, including microwave and millimeter-wave devices and very-high-speed ICs (VHSICs) are being built. Already developed are 208-gate GaAs gate-array VHSICs, 3 GHz GaAs static frequency-divider VHSICs, 0.1-4.5 GHz GaAs dynamic frequency-divider VHSICs, C-band GaAs low-noise-amplifier

(LNA) monolithic microwave integrated circuits (MMICs) with a noise figure of 1-3.5 dB and a gain of 20-33 dB, and Ku-band [GaAs] LNA MMICs with a noise figure of 3 dB and a gain of 12-18 dB. These devices are critically needed for economic and defense development. [passage omitted]

## R&D of High-T<sub>c</sub> Superconducting Devices

92P60002A Beijing WULI [PHYSICS] in Chinese Vol 20 No 6, Jun 91 pp 334-338

[Article by Zhou Lian [0719 1670] of the Northwest Institute of Nonferrous Metals (NWINM), Baoji, 721014: "China's Research Advances in High-Temperature Superconducting Materials"]

[Excerpts] [Passage omitted]

### III. Some Advances in [Development of] High-T<sub>c</sub> Oxide Devices

#### [Passage omitted] 1. Magnetic Shielding

NWINM has fabricated a YBCO-superconductor magnetically shielded tube,<sup>13</sup> which has a shielding factor of  $10^5$  and a maximum shielded magnetic field of 4 mT [milliTeslas]; this device has been used by Fudan University researchers in a radio-frequency (rf) quantum amplifying interferometer.

#### 2. Magnetic Flux Converters

Two types of flux converters have recently been fabricated. One, developed by Beijing Institute of Nonferrous Metals from Bi-Pb-Sr-Ca-Cu-O/Ag wire, has two continuous coils. When the magnetic oscillation coil generates a  $1 \times 10^{-6}$  A-m<sup>-2</sup> signal, its flux change as measured by a SQUID [superconducting quantum interference device] is  $10 \phi_0$  (where  $\phi_0$ , the magnetic flux quantum, =  $2.07 \times 10^{-15}$  Webers). The other type of flux converter, developed by NWINM, consists of a 1,500-mm-long BiPbSr-CaCuO/Ag wire wound into four linked coils; as measured by an rf quantum amplifying interferometer with a sensitivity of  $\phi_0/7$ , its coupling factor is 0.194.

#### 3. UHF Antennas

Using a Bi-Sr-Ca-Cu-O superconductor, Qinghua University has fabricated a miniature loop antenna and matching network; at a 560 MHz optimized frequency and a temperature of 77K, its relative gain compared to a copper antenna of the same type is 5 dB higher.<sup>14</sup>

#### 4. rf Quantum Interferometers

Several domestic research institutes have developed a few types of rf quantum interferometers and have employed them as precision instruments for measuring magnetic fields and electrical quantities. From a YBCO sintered bulk superconductor, the China Metrology Research Institute has fabricated an rf quantum amplifying interferometer.<sup>15,16</sup> At 77K, its corresponding flux noise is  $5 \times 10^{-4} \phi_0/\text{Hz}^{1/2}$  (in the 10-100 Hz range). This device has been used to determine the magnetic shielding capacity of high-T<sub>c</sub> superconducting materials, resistance, and changes in biomagnetic and geomagnetic fields; it has stood up for over 100 recyclings between

77K and 300K [i.e., room temperature]. Fudan University has used a double-hole rf quantum amplifying interferometer as a sensor in a system for determining magnetic susceptibility over a range of temperatures. In the 20-200 Hz frequency range, this apparatus's susceptibility resolution is  $5 \times 10^{-8}$  emu/cm<sup>3</sup>.<sup>17</sup> New applications have already been found for these rf quantum amplifying interferometers, even while their performance is still being improved. [passage omitted]

### References

[Passage omitted]

13. Wang Jingrong et al., Proceedings ICMC '89, Los Angeles, July 1989, 24-28.

14. He Aisheng et al., CRYOGENICS, 30 (1990), 946.

15. Chiao Weichuan et al., Proceedings of the Beijing International Conference on High-Temperature Superconductivity, World Scientific (1989), 58.

16. S. Q. Xue et al., CRYOGENICS, 30 (1990), 925.

17. Qiu Jingwu et al., CRYOGENICS, 30 (1990), 920.

### Deposition of Superconducting Nb Films, Preparation of Nb/Al-AlO<sub>x</sub>/Nb Josephson Junctions

91FE0690A Hefei DIWEN YU CHAODAO [CRYOGENICS AND SUPERCONDUCTIVITY] in Chinese Vol 19 No 2, May 91 pp 16-21

[Article by Xu Jianhong [1776 0494 5725], Cai Anjiang [5591 1344 3068], Liu Pingmei [0491 5493 2734], Tang Yanlin [3282 1693 2651], Liu Xinhua [0491 2450 5478], Wang Jiyun [3769 0679 0061], Gong Haiyan [1362 3189 3601], and Zhang Chaoping [1728 2600 5281] of Hefei Institute of Cryogenics and Electronics (HICE): "Deposition of Superconducting Nb Films, Preparation of Nb/Al-AlO<sub>x</sub>/Nb Josephson Junctions"; MS received 5 Feb 91]

[Text]

### Abstract

Superconducting Nb films with room-temperature-to-liquid-nitrogen-temperature resistance ratio  $\beta$  better than 2.2 were successfully deposited via a planar magnetron sputtering technique using a cryo-pump vacuum system by rigorously controlling the sputtering parameters and procedure. Using a wet-etching technique, Nb/Al-AlO<sub>x</sub>/Nb Josephson junctions with a cross-section area of  $4 \times 4 \mu\text{m}^2$  were prepared. The Josephson effect was observed with the aid of a 4.4 K cryostat developed by HICE.

### 1. Introduction

Thin-film Josephson junctions made from soft superconducting materials such as Sn and Pb have poor stability and reliability because they cannot withstand repeated

cycling between room temperature and 4.2 K. In comparison, Nb has a relatively high mechanical strength and is chemically stable. In elemental superconductors, it has the highest transition temperature and is suitable for fabrication of Josephson junctions. Nevertheless, Nb has a high melting point; moreover, it is easily contaminated by impurities. Therefore, Nb films are difficult to fabricate. Usually, Nb films are made by evaporation with a high-power electron gun or deposition by sputtering.

In the process of making thin-film Josephson junctions, preparation of the potential barrier is very important. The oxide formed on the surface of Nb can be used as a barrier. However, in addition to forming the high-valence  $\text{Nb}_2\text{O}_5$ , there is also the lower-valence  $\text{Nb}_2\text{O}_3$ . The latter is conductive and the former has a high dielectric constant. This significantly affects the high-frequency (HF) performance of the device. In order to resolve this problem,  $\text{SiO}_2$  and  $\text{Al}_2\text{O}_3$  are used to replace Nb oxides.

In 1983, M. Gurvitch<sup>1</sup> developed the Nb/Al- $\text{AlO}_x$ /Nb junction technique. Since then, S. Morohashi et al.<sup>2</sup> made some improvements. Thus, a solid foundation has been laid for the development of a total Nb Josephson-junction technology. The technique involves the deposition of a layer of Al on the surface of Nb film and then formation of  $\text{Al}_2\text{O}_3$  on Al.  $\text{Al}_2\text{O}_3$  has excellent chemical stability and a tight chemical structure; further, it has a low dielectric constant. Therefore, Nb-based Josephson junctions with an  $\text{Al}_2\text{O}_3$  barrier are reliable and have better HF characteristics.

Our preliminary results on the study of Nb/Al- $\text{AlO}_x$ /Nb Josephson junctions are reported here.

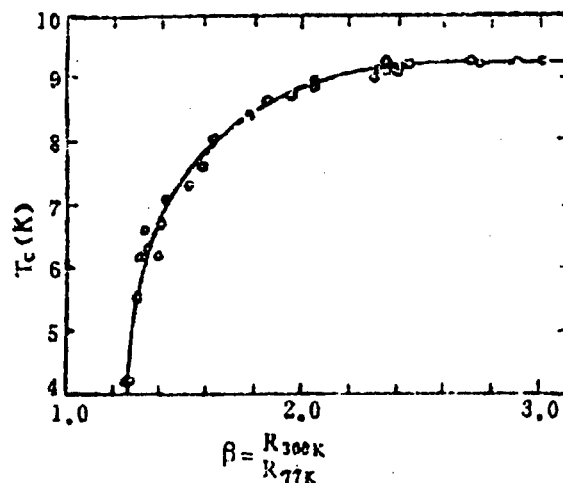


Figure 1.  $T_c$  vs.  $\beta$  for Nb Films<sup>5</sup>

## 2. Deposition of Nb Films and Evaluation of Performance

The equipment used is a RF planar magnetron sputtering device. The vacuum system of the device consists of a mechanical pump and a cryo-pump. Its vacuum limit is  $5.0 \times 10^{-7}$  Torr.

High-purity Nb was used as the target material and high-purity Ar was used as the sputtering gas. The substrate is single-crystal Si wafer. It is carefully cleaned prior to use and baked at  $140^\circ\text{C}$  for approximately 1 hour. Before deposition of the Nb film, the system is pumped to a background vacuum of  $1.0 \times 10^{-6}$  Torr. The baking and degassing are then carried out. Ar is let into the system to  $10^{-3}$ - $10^{-2}$  Torr to begin pre-sputtering for 3-5 minutes. The system is then switched to Nb film deposition. In the meantime, the substrate is maintained at a proper temperature.

Table I lists the results obtained under different conditions.

Table I. Values of Nb Film Under Different Conditions

Sample	RF high voltage (kV)	Ar partial pressure (Torr)	Substrate temperature ( $^\circ\text{C}$ )	Film thickness (Angstroms)	$\beta = R_{300}/R_{77}$
1	3.0	$1.5 \times 10^{-2}$	300	2,000	3.41
2	3.0	$3.0 \times 10^{-3}$	200	2,500	2.88
3	3.0	$5 \times 10^{-3}$	100	2,500	2.81
4	3.0	$4 \times 10^{-3}$	Room temperature	2,000	2.73
5	2.8	$3 \times 10^{-3}$	Room temperature	1,500	2.57
6	2.6	$4 \times 10^{-3}$	Room temperature	1,500	2.75
7	2.6	$3 \times 10^{-3}$	Room temperature	1,500	2.37
8	2.4	$4 \times 10^{-3}$	Room temperature	1,500	2.25

An important parameter in judging the superconducting quality of Nb films is the transition temperature. Especially in the device-fabrication process, it is necessary to know this value. Using the room-temperature-to-liquid-N-temperature resistance ratio,  $\beta$ , we can roughly estimate the superconducting transition temperature  $T_c$ .<sup>3-5</sup> Figure 1 shows the relation between  $T_c$  and  $\beta$  for Nb films.

In conjunction with Table I, we can see that (1) at the same RF voltage, the  $\beta$  of the Nb film decreases with falling substrate temperature, and (2)  $\beta$  also drops with decreasing RF voltage when the substrate temperature remains constant. In this work,  $\beta$  is normally better than 2.2. Based on the plot,  $T_c$  should be around 9 K. It was experimentally measured to be better than 8 K.

### 3. Preparation of Nb/Al-AIO<sub>x</sub>/Nb Josephson Junctions

Figure 2 shows the process flow diagram for fabricating the Nb/Al-AIO<sub>x</sub>/Nb Josephson junction.

#### 3.1 Substrate Material and Cleaning

P-type <111> single-crystal silicon wafer was chosen as the substrate. A layer of SiO<sub>2</sub>, approximately 5,000 Angstroms thick, is thermally grown to serve as a barrier layer. Prior to deposition of Nb film, the substrate undergoes the following cleaning treatments: (1) boiling in solution I, i.e., NH<sub>4</sub>OH:H<sub>2</sub>O<sub>2</sub>:H<sub>2</sub>O = 1:2:5, for 10 minutes, (2) boiling in solution II, i.e., HCl:H<sub>2</sub>O<sub>2</sub>:H<sub>2</sub>O = 1:2:6, for 15 minutes, and (3) rinsing thoroughly with deionized water and baking dry at 140°C for approximately 1 hour.

3.2 Parameters used to deposit the Nb film for the lower electrode are shown in Table II.

Table II. Parameters for Depositing Lower Electrode Nb Films

Background vacuum	RF voltage	Ar partial pressure	Substrate temperature	Deposition rate
1 x 10 <sup>-6</sup> Torr	3.0 kV	3 x 10 <sup>-3</sup> Torr	300°C	20 Angstroms/s

The film thickness is held at approximately 2,500 Angstroms by controlling the deposition time.

#### 3.3 Etching of Lower Electrode Pattern

Nb films are etched with domestically made BN-303 negative photoresist using a wet-etching approach. The etchants are HF:HNO<sub>3</sub>:H<sub>2</sub>O = 1:4:8 and H<sub>2</sub>SO<sub>4</sub>:H<sub>2</sub>O<sub>2</sub> = 3:1. The photoresist is removed at 80°C.

#### 3.4 Al Film Deposition

Before depositing the Al film, the lower Nb film electrode is baked in high vacuum at 400°C to remove any impurities adsorbed on its surface. Al film deposition begins after the temperature is lowered. Table III lists the deposition conditions for Al film.

Table III. Al Film Deposition Conditions

Background vacuum	RF voltage	Ar partial pressure	Substrate temperature	Pre-sputtering time	Deposition rate
1 x 10 <sup>-6</sup> Torr	3.0 kV	1 x 10 <sup>-3</sup> Torr	Room temperature	300 s	5 Angstroms/s

The purpose for pre-sputtering is to remove adsorbed impurities on the target surface. The thickness of the film is controlled at approximately 100 Angstroms.

#### 3.5 Oxidation of Al Film

Oxygen is introduced into the system and maintained for 30 minutes. Thus a layer of Al<sub>2</sub>O<sub>3</sub> is formed on the fresh Al film.

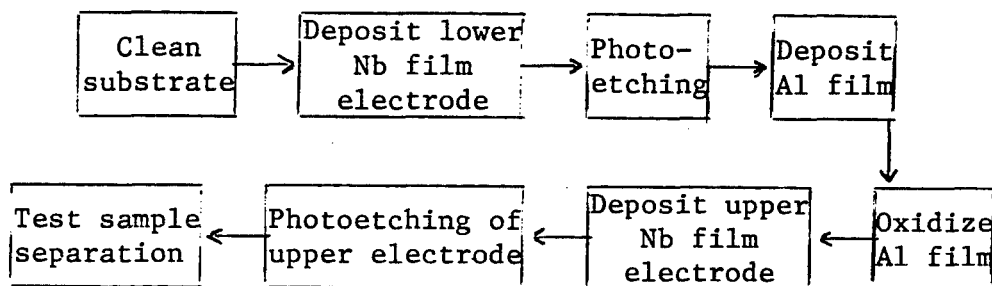


Figure 2. Fabrication Process for Nb/Al-AIO<sub>x</sub>/Nb Josephson Junctions

### 3.6 Deposition of Upper Nb Film Electrode

After oxidation is completed, the system is immediately pumped to high vacuum to proceed with the deposition of the upper Nb film electrode. After taking into consideration that high-energy ions may damage the aluminum

oxide layer during sputtering and mutual diffusion between Al and Nb may take place, deposition conditions were adjusted as shown in Table IV.  $\beta$  is greater than 2.0 and the thickness is controlled at 1,500 Angstroms.

Table IV. Parameters for Depositing Upper Electrode Nb Films

Background vacuum	RF voltage	Ar partial pressure	Substrate temperature	Deposition rate
$1 \times 10^{-6}$	2.6 kV	$3 \times 10^{-3}$ Torr	Room temperature	20 Angstroms/s

3.7 The etching condition for the upper electrode is identical to that of the lower electrode. The etching time is limited by the appearance of the lower electrode pattern.

3.8 Au electrodes were evaporated onto specimens and separated. Indium (In) leads were soldered or pressed on for testing.

Figure 3 [photo not reproduced] is a SEM (scanning electron microscope) picture of a Nb/Al-AlO<sub>x</sub>/Nb Josephson junction we prepared. The junction area is  $4 \times 4 \mu\text{m}^2$ .

### 4. DC I-V [Current-Voltage] Characteristics

A standard four-lead method was used to measure the DC I-V characteristics of Nb/Al-AlO<sub>x</sub>/Nb Josephson junctions fabricated with a 4.4 K cryostat developed by HICE. Figure 4 shows the results.

Figures 4(a) and 4(b) are typical Josephson effects and their  $I_c$  values are 1.5 mA and 70  $\mu\text{A}$ , respectively. There is no hysteresis. The I-V curve shown in Figure 4(c) is "smoother," indicating the specimen has experienced larger temperature excursion. Figure 4(d) is an I-V curve with hysteresis.

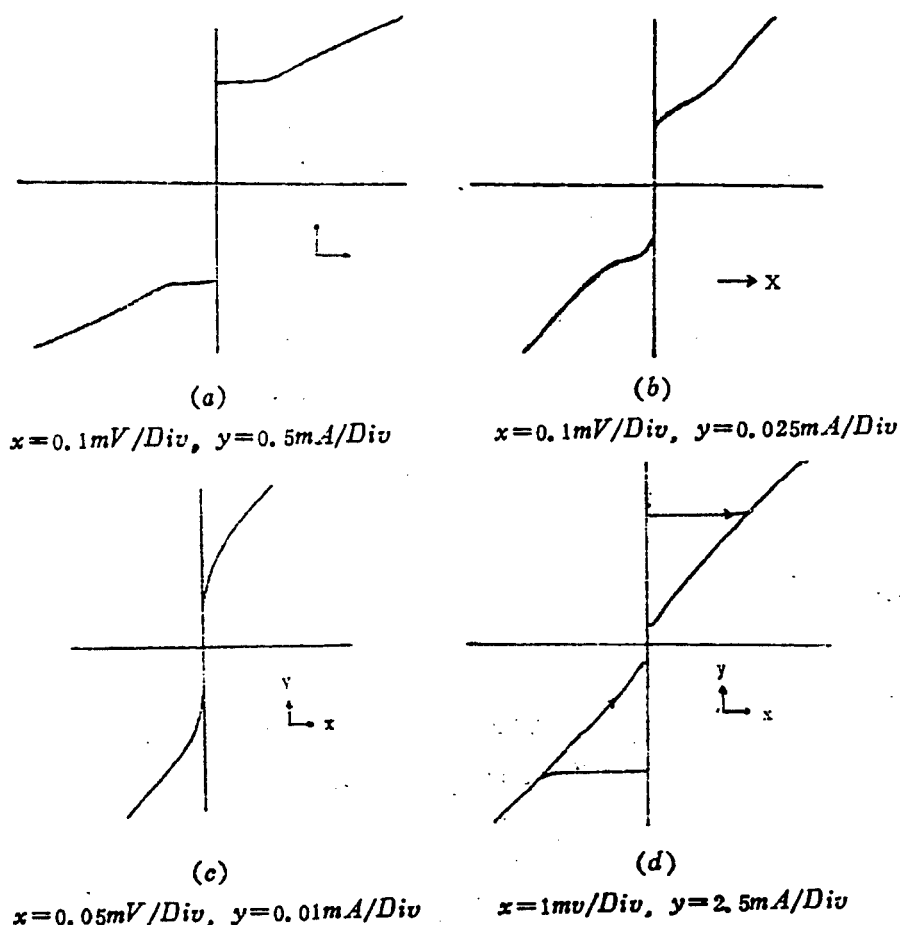


Figure 4. I-V Curve for Nb/Al-AlO<sub>x</sub>/Nb Josephson Junctions

## 5. Discussion

Sputtering is chosen to minimize contamination.<sup>6</sup> During its growth, Nb film is particularly sensitive to oxygen and oxygen-containing impurities. A minute amount of impurity in Nb film will lead to a decrease of  $T_c$ . To obtain high-quality Nb films by deposition, it is necessary to accomplish the following:

5.1 Minimize total impurities. The background vacuum of the system needs to be improved. High-purity Ar gas and high-purity Nb targets must be used. The substrate material has to be thoroughly cleaned. In our system, a cryo-pump is used, instead of an oil-diffusion pump. Compared to oil-diffusion pumps, a cryo-pump works at a higher speed and can achieve a higher vacuum. Furthermore, it avoids the oil contamination issue associated with oil-diffusion pumps. Sputtering is chosen because the target surface is cleaned as the process proceeds and the residual oxygen-containing gas could adsorb on sputtered Nb.

5.2 Minimize interaction time between impurity and substrate. This is primarily achieved by raising the sputtering rate. A high sputtering rate is obtained by adjusting the Ar partial pressure, RF voltage and target to substrate position using magnetron sputtering.

5.3 Remove impurities on the substrate. Another effective measure is to raise the substrate temperature. On one hand, gas impurities adsorbed on the substrate surface are released at high temperature. On the other hand, because of increased molecular motion, the probability for gas impurities to stay in the film also drops significantly. In this work, 300°C was chosen as the suitable substrate temperature.

When depositing the upper Nb film by sputtering, high-energy ions are bombarding the oxide layer on the Al film which leads to the degradation of the junction. In earlier work, Nb film was only used as the lower electrode. In this work, the sputtering voltage for the upper Nb film is lower than that for the lower Nb film to reduce ionic energy. In this case, substrate temperature is also very important. When substrate temperature is high, the surface of the lower electrode is poor, possibly due to diffusion of Nb and Al.

When tests are done in a Dewar at liquid-helium temperature, the importance of lead wires is not significant enough. However, with a cryostat, the effect of leads is noticeable. If lead wires are too thick, the cryostat will have a larger thermal load which significantly affects the time required to lower the temperature. Sometimes, the cryostat cannot even function properly.

## 6. Conclusions

Superconducting Nb films with excellent characteristics have been prepared by deposition with a planar magnetron RF sputtering technique by controlling the sputtering parameters. Nb/Al-AlO<sub>x</sub>/Nb Josephson junctions have been fabricated using a wet chemical-etching

method. Ideal Josephson effects were observed with the aid of a cryostat. This has laid a solid foundation for further development of Nb-based Josephson junctions and quasi-particle tunneling junctions.

## References

1. M. Gurvitch, M. A. Washington, and H. A. Huggins, APPL. PHYS. LETT., 24, 472, 1983.
2. S. Morohashi, F. Shinoki, et al., APPL. PHYS. LETT., 46, 1179, 1985.
3. R. Frerichs and C. J. Kircher, J. APPL. PHYS., 34, 3541, 1969.
4. Low-Temperature Superconductivity Laboratory, Department of Physics, Fudan University, DIWEN YU CHAODAO [CRYOGENICS AND SUPERCONDUCTIVITY], 9, 24, 1981.
5. Meng Xiaofan [1322 1420 0416], Cui Guangqi [1508 1639 7221], et al., DIWEN YU CHAODAO [CRYOGENICS AND SUPERCONDUCTIVITY], 12, 36, 1984.
6. J. J. Besset, "Thin Solid Films," 32, 19, 1976.

## Study of RF SQUIDS at Liquid-Nitrogen Temperature

91FE0690B Hefei DIWEN YU CHAODAO  
[CRYOGENICS AND SUPERCONDUCTIVITY]  
in Chinese Vol 19 No 2, May 91 pp 40-45

[Article by Zhang Chaoxing [1728 2600 5281], Wang Haiyan [3769 3189 1750], Deng Hongbin [6772 4767 2430], Hu Laiping [5170 0171 1627], Zhang Hongbin [1728 1347 2430], Wu Lei [1566 5623], and Zhang Zheng [1728 1513] of Hefei Institute of Cryogenics and Electronics (HICE): "Study of RF SQUIDS at Liquid Nitrogen Temperature"; MS received 5 Feb 91]

[Text]

## Abstract

Double-hole RF-SQUIDS [radio-frequency superconducting quantum interference devices] made from high- $T_c$  bulk YBCO have been operated reliably at liquid-nitrogen (liquid-N) temperature. This paper discusses the technical details of the material, device fabrication and measurement. Basic concerns of circuits for RF-SQUID instruments are presented. In the 0-100 Hz frequency range, the flux resolution is  $5.1 \times 10^{-4} \phi_0/(\text{Hz})^{1/2}$  [where  $\phi_0$ , the magnetic flux quantum, is about  $2.068 \times 10^{-7}$  gauss-m<sup>2</sup>], corresponding to an energy resolution of  $2.8 \times 10^{-27}$  J/Hz. For a good device the read-out circuit is still the contributor to flux noise. Finally, applications of RF-SQUIDS made of high- $T_c$  bulk materials are discussed.

## 1. Introduction

The superconducting quantum interference device (SQUID) is one of the basic types of superconducting electronic devices. A series of high-performance instruments has been built with SQUIDs. These instruments have outperformed conventional electronic devices beyond their limitations. In many special applications, they cannot be replaced by conventional technology. For instance, SQUIDs are used in fundamental research, precision measurement, survey of resources, biomedicine, and military applications such as high-speed circuitry and magnetic-anomaly detection, coast security and low-frequency communications. Although SQUIDs made of low-critical-temperature (low- $T_c$ ) materials have been available commercially for some time, the range of applications is limited by the stringent liquid-helium operating condition which is expensive and inconvenient for the users. Conventional electronic devices operating at liquid-N temperature are widely used. There is no doubt that high-performance superconducting devices and equipment operating at liquid-N temperature will be welcomed by users.

Since the discovery of high- $T_c$  oxide superconductors, a great deal of work has been devoted to device development in order to reproduce the performance of low- $T_c$  superconducting devices at liquid-N temperature. One success is the high- $T_c$  SQUID. DC-SQUIDs and RF-SQUIDs<sup>1-6</sup> have been successfully made with high- $T_c$  bulk and thin-film materials and used in a large number of applications.<sup>4,5</sup> Because the device is based on superconductivity of particles and Josephson-junction structure, the main problems are excess noise in the low-frequency band and stability of cycling between room temperature and low temperature. Theoretically, the high- $T_c$  SQUID has a magnetic flux resolution comparable to that of a commercial low- $T_c$  device.<sup>7</sup> Therefore, it is important for researchers working on superconducting electronic devices to investigate suitable materials and develop the necessary thin-film preparation techniques to build devices that meet our needs, and to study device structure and parameters and read-out circuits to improve the overall performance.

Our work began with the preparation of YBCO material to study the Josephson-junction effect at liquid-N temperature. It resulted in the development of RF-SQUIDs that operate at liquid-N temperature. The corresponding flux automatic compensation lock-in read-out circuit was developed. The flux resolution between 0 and 100 Hz is  $5.1 \times 10^{-4} \phi_0/(\text{Hz})^{1/2}$ , which corresponds to  $2.8 \times 10^{-27} \text{ J/Hz}$ . Good devices show a low noise level. Compared to the triangular wave modulated by flux, the primary source of noise is determined by the read-out circuit. There is a significant difference in stability. Some devices failed to show triangular waves after a few cycles between room temperature and low temperature. Some had good triangular-wave output for flux lock-in after several dozen cycles over 1 year. Material quality plays a critical role in noise level and device stability.

## 2. Preparation of Materials and Devices

Chosen as the raw materials were 99.95 percent  $\text{Y}_2\text{O}_3$ , 99 percent  $\text{BaCO}_3$  and 99 percent  $\text{CuO}$ . They were carefully mixed and ground according to a stoichiometric ratio of  $\text{Y}:\text{Ba}:\text{Cu} = 1:2:3$ . The mixture was pre-heated, sintered and annealed using techniques reported in the literature. However, some fine details were addressed to yield a more homogeneous structure, resulting in a higher  $T_c$ , narrower transition width and higher  $J_c$  [critical current density]. The  $T_c$  is usually above 90 K, transition width less than 0.5 K, and  $J_c$  over  $100 \text{ A/cm}^2$ . A bridge junction made of this material exhibits more classical ac and dc Josephson effects.

Figure 1 shows the principle of an RF-SQUID.  $L$  is a superconducting ring with a weakly connected junction.  $L$  is coupled in parallel to a resonant tank circuit  $L_T, C_T$ . When  $L_T, C_T$  is excited at its resonant frequency by a RF source, the voltage of the tank circuit is modulated by the external magnetic flux  $\phi_e$  of  $L$ . The modulated output and external flux are periodic functions of quantum magnetic flux  $\phi_0$ . The amplitude of magnetic modulation,  $\Delta V_T$ , is

$$\Delta V_T = \frac{\omega L_T \phi_0}{2M} = \frac{\omega}{2K} \sqrt{\frac{L_T}{L}} \phi_0 \quad (1)$$

where  $\omega$  is the angular frequency of the RF oscillator,  $M$  is the mutual inductance between the superconducting ring  $L$  and the tank circuit inductance  $L_T$ ,  $K$  is a coupling coefficient, and the magnetic flux quantum  $\phi_0 = 2.07 \times 10^{-15} \text{ Webers}$  [ $= 2.07 \times 10^{-15} \text{ Tesla-m}^2$ ].

In order to obtain the periodic voltage-flux relation described above, the weak connection of the superconducting ring ought to satisfy a sinusoidal current phase relation, i.e.,  $I = I_c \sin \theta$ . Furthermore, there is no hysteresis and  $2\pi I_c R^2 C / \phi_0 < 1$ . The ring inductance should satisfy  $2\pi L I_c / \phi_0 \geq 1$ . The coupling between the ring and the tank circuit should satisfy  $K^2 Q \geq 1$ , where  $Q$  is the quality factor of the tank circuit. An additional limit imposed to high- $T_c$  SQUIDs is that the  $I_c$  of weak connection may be higher than that of 4.2-K devices, but the inductance of the ring must be less than that of 4.2-K devices. Otherwise, the flux-modulated signal will be buried in the noise. Based on noise theory of RF-SQUIDs, reducing inductance is helpful in improving the resolution of magnetic flux. Hence, we adopted a double-hole bridge-junction SQUID structure shown in Figure 2. The inductance of the double-hole structure is  $1/2$  of the ring inductance of the same aperture. Therefore, the weak connection may be slightly larger, which makes it easier to adjust  $I_c$ . In addition, the structure is mechanically symmetric, which enhances mechanical stability of the device. Adjusting  $I_c$  is a key step in the fabrication of the device. Usually, it needs to be repeated several times

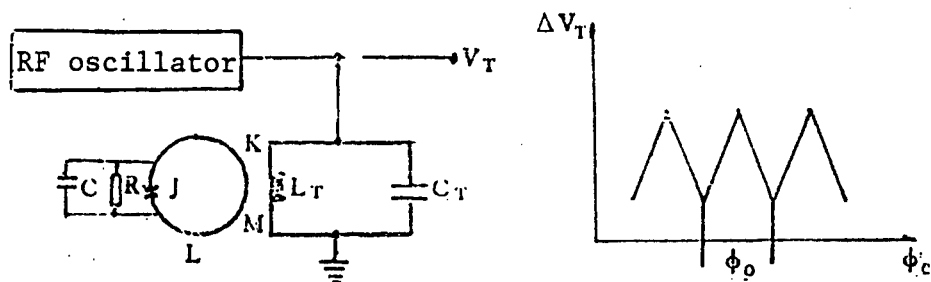


Figure 1. Principle of RF-SQUID

until a good triangular wave is obtained. An RF-SQUID transducer is made by packaging an adjusted device with the tank circuit.

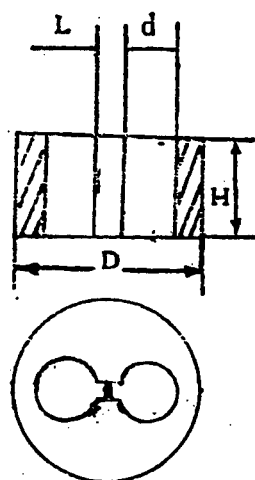


Figure 2. Schematic Diagram of a Double-Hole RF-SQUID

D: 9 mm, H: 3-5 mm, d: 0.9-1 mm, l: 0.5 mm

### 3. Electronic Circuit

The read-out circuit used is similar to a conventional RF-SQUID read-out circuit, i.e., using the flux-compensated lock-in read-out method to measure flux changes. Figure 3 shows the block diagram of the circuit. The main features of this circuit include the use of a higher RF bias frequency for better flux resolution, using varactor tuning for ease of operation, using a low-noise FET amplifier as a pre-amplifier to improve the match between the device and the circuit, and using a higher flux-modulating frequency to enhance the capability to track external flux changes.

The high-frequency (HF) component is a key part of the RF-SQUID read-out circuit and requires careful design

and testing. The major specifications of the RF amplifier include the following: center frequency about 30 MHz, bandwidth about 0.6 MHz, voltage gain  $\geq 80$  dB, input impedance  $> 2k\Omega$  and equivalent input noise better than  $2nV/(Hz)^{1/2}$ . The low-frequency (LF) component is for automatic flux-compensated lock-in detection. It is capable of choosing different operating modes to meet different needs. The monitoring interface is used to check whether the instrument is working properly and the output interface is to record input flux changes.

### 4. Experiments and Performance Measurements

The following experiments and performance measurements were carried out:

A four-lead method was employed to measure the  $T_c$  and  $J_c$  of the material. Materials with high  $T_c$ , narrow transition width and high  $J_c$  were chosen to make bridge junctions and dc and ac Josephson effects were investigated. Typical I-V characteristics were found. The dc transition is relatively sharper and the ac behavior shows a clear step. In addition, the magnetic field was found to be able to modulate  $I_c$ . Materials with such characteristics can be used to fabricate devices.

The devices were tested using the circuit described in Section 3. The device is loaded into a probe and connection is made with a low-loss cable and amplifier. The probe is shielded by a high- $T_c$  superconducting cylinder. Tuning begins after the device is chilled down sufficiently. A sweeping signal is added to observe the triangular waveform on an oscilloscope through the monitoring interface. The bandwidth of observation is about 200 kHz. When proper coupling between  $I_c$  and the circuit is achieved, a good triangular waveform can be obtained, as shown in Figure 4 [photo not reproduced]. The amplitude of voltage modulation by flux is quite different with different devices. Usually, it should be above  $5 \mu V$  to be acceptable. Better devices can achieve  $10 \mu V$ . During the process of adjusting  $I_c$ , a transition of operation mode from hysteresis to dispersion was observed. In addition, multi-quantum transition was also observed as a result of unsuitable device parameters (mainly  $I_c$ ).



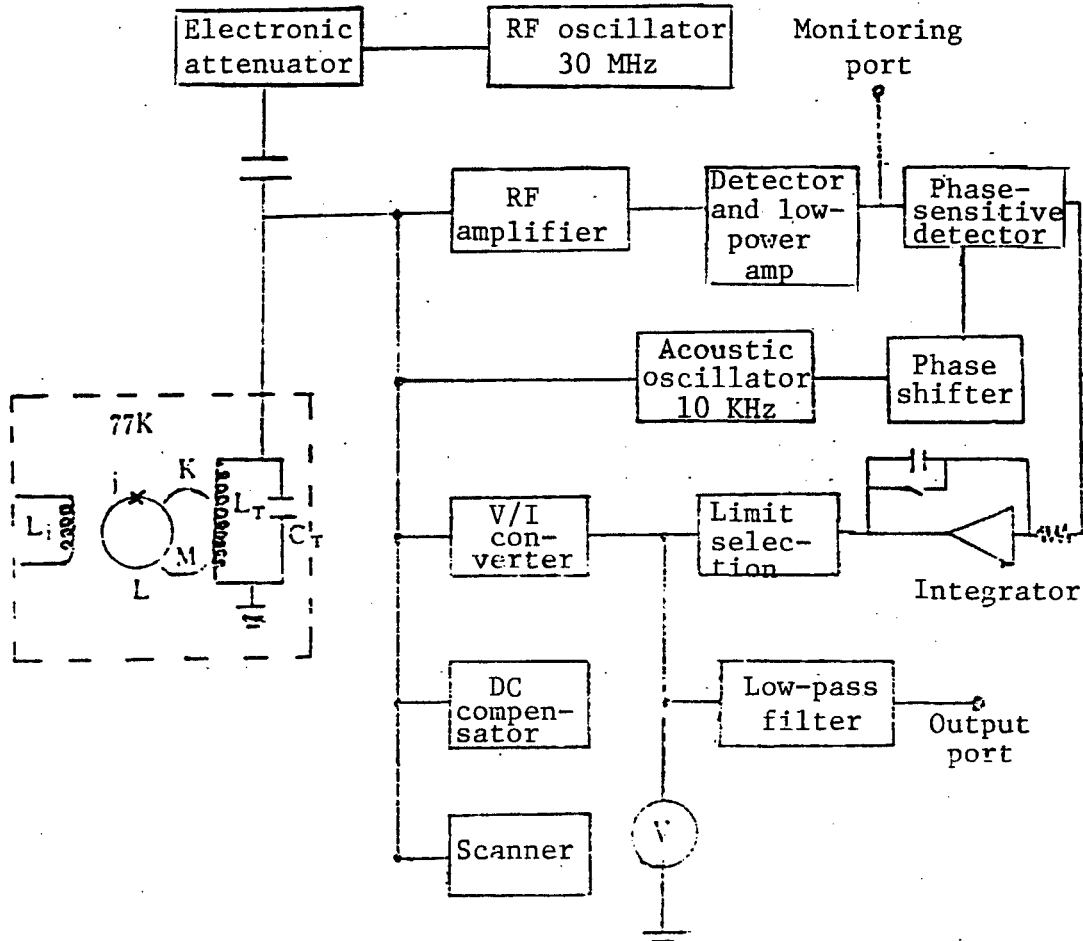


Figure 3. Schematic Diagram of Flux-Compensated Lock-in RF-SQUID Read-Out Circuit

The triangular waveforms generated by different devices are significantly different in both signal-to-noise ratio and amplitude. The relation between the dc and ac Josephson effect I-V characteristics and the shape of the triangular waveform has been discussed elsewhere.<sup>8</sup>

Our devices were measured by cycling between room temperature and liquid-N temperature. The triangular waveforms of sealed devices were found to have no apparent changes after several dozen cycles, as shown in Figure 5 [photo not reproduced].

The contribution of the amplifier to flux noise was investigated. Different amplifiers were used to observe the output of the same device. It was discovered that the triangular waveform is apparently better with a low-noise amplifier compared to a high-noise amplifier, as shown in Figure 6 [photo not reproduced]. Therefore, the read-out circuit plays a dominant role in terms of noise flux.

In order to evaluate the device, lock-in measurement was made using the circuit described in Section 3. The flux noise voltage is measured while the device operates at a specific point. Figure 7 shows the flux noise curve in the most sensitive scale of the instrument at 0-1 Hz. The corresponding magnetic flux resolution is  $3.04 \times 10^{-3} \phi_0/(\text{Hz})^{1/2}$ . Table I shows the results of the device at different frequency ranges. The rate of change of output voltage versus input flux is  $\Delta V/\Delta \phi_e = 2060 \text{ mV}/\phi_0$ . The inductance of the device is  $2 \times 10^{-10} \text{ H}$ . The following equations can be used to calculate the magnetic flux resolution and energy resolution:

$$S_{\phi}^{\frac{1}{2}} = \frac{V_{N_F-5}}{\Delta V/\Delta \phi_e} \cdot \frac{1}{\sqrt{\Delta f}} \quad (\phi_0/\sqrt{\text{Hz}}) \quad (2)$$

$$\epsilon = \frac{S_{\phi}}{2L} \quad (\text{J}/\text{Hz}) \quad (3)$$

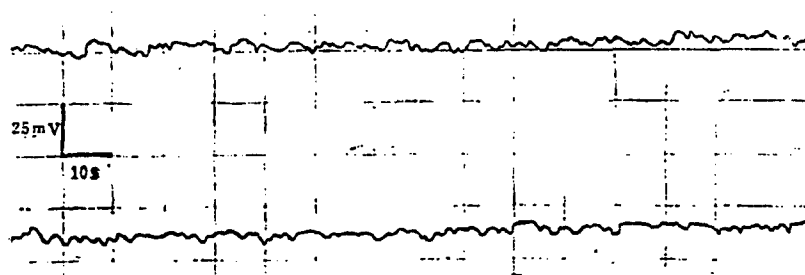


Figure 7. Noise Flux of Device at 0-1 Hz

Several devices were measured using a recorder at 0-1 Hz. The corresponding magnetic flux resolution is in the range of  $3.5 \times 10^{-3} \phi_0/(\text{Hz})^{1/2}$ .

Table I.  $S^{1/2}$  and in Different Frequency Ranges

Measured bandwidth $\Delta f$ (Hz)	0-0.83	0-9.4	0-112
Noise voltage peak-to-peak $V_{NP-P}$ (mV)	28.5	40	55
Magnetic flux resolution $S^{1/2}_\phi$ ( $\times 10^{-3} \phi_0/(\text{Hz})^{1/2}$ )	3.04	1.27	0.51
Energy resolution $\epsilon$ (J/Hz)	$9.9 \times 10^{-26}$	$1.7 \times 10^{-26}$	$2.8 \times 10^{-27}$

## 5. Discussion

5.1 RF-SQUIDS capable of working at liquid-N temperature were successfully prepared using bulk YBCO. In conjunction with the appropriate circuit, RF superconducting quantum interference systems which could operate at liquid-N temperature were made. These devices could be used in the laboratory; in addition, they bring a great deal of convenience and feasibility to the exploration of certain applications.

5.2 The characteristics of these bulk devices do not change much after repeated cyclings between room temperature and liquid-N temperature. On one hand, this shows that intrinsic properties of this material do not change due to temperature cycling. On the other hand, because the substrate and the junction are made of the same material, there is no thermal mismatch or lattice mismatch between the superconducting thin film and the substrate. This is the advantage of this device.

5.3 Humidity and water vapor are detrimental to the superconductivity of YBCO. The fine bridge region is most susceptible to humidity attack. Better techniques may improve the corrosion resistance of the material. Just like with other semiconductor devices, the material

needs to be sealed to lengthen the useful life of high- $T_c$  YBCO devices. A suitable packaging technique must be sought to solve this problem.

5.4 This device has a higher  $1/f$  noise, which is not good for LF applications. The turning point from  $1/f$  noise to white noise was found to be at 5 Hz. Whether this point can be pushed toward even lower frequency must be determined by additional research in noise mechanisms and material processing techniques.

5.5 For good devices, the read-out circuit plays a dominant role in flux noise. Improving the match between the read-out circuit and the device can further improve the magnetic flux resolution and other indicators.

5.6 In conclusion, the bulk device and the resulting instrument permit us to attempt certain applications. The flux resolution of the magnetometer made of this device is as high as  $1 \times 10^{-12} \text{ T}/(\text{Hz})^{1/2}$ . This magnetometer may be used to measure weak abnormal magnetic signals and magnetic signals of the human heart (of the order of approximately  $5 \times 10^{-11} \text{ T}$ ). These applications are undoubtedly very attractive.

## References

1. R. H. Koch, C. P. Umbach, et al., "Quantum Interference Devices Made From Superconducting Oxide Thin Films," APPL. PHYS. LETT., Vol 51, pp 200-202, 1987.
2. J. E. Zimmerman, J. A. Beall, et al., "Operation of a Y-Ba-Cu-O RF-SQUID at 81 K," APPL. PHYS. LETT., Vol 51, pp 677-618 [as published], 1987.
3. Xue Shouqing [5641 1108 3237], Wang Shizhong [3769 0013 0022], et al., "Operation of an RF-SQUID Made From Y-Ba-Cu-O in Liquid Nitrogen," DIWEN YU CHAODAO [CRYOGENICS AND SUPERCONDUCTIVITY], Vol 17, No 1, pp 15-20, February 1989.
4. S. Q. Xue, J. Zhang, et al., "High- $T_c$  RF-SQUID Magnetometer and Its Applications," ICEC 13, 24-27 April 1990, Beijing, PRC.

5. Qiu Jing-Wu, Zhou Lu-Wei, et al., "High-Temperature SQUID Susceptibility Measuring System," ICEC 13, 24-27 April 1990, Beijing, PRC.
6. Fan Chang-Xin, Wei Xin-Miao, et al., "High-Temperature Bull-RF-SQUID," ICEC 13, 24-27 April 1990, Beijing, PRC.
7. John Clarke, "Principles and Applications of SQUID," PROCEEDINGS OF THE IEEE, Vol 77, No 8, pp 1208-1223, August 1989.
8. Liu Dong [0491 2639] and Yang Tao [2799 3447], "Characteristics of RF-SQUID and YBCO Particles," DIWEN YU CHAODAO [CRYOGENICS AND SUPERCONDUCTIVITY], No 1, p 40, 1991.

## Reports on Fiber Optic Communications

### Shanghai Gets First State-of-the-Art Optical Cable Production Line

92P60010A Shanghai JIEFANG RIBAO in Chinese  
27 Jul 91 p 1

[Article by Zhang Zhiyuan [1728 1807 6678]: "First Integrated Fiber-Optic-Cable Production Line Completed"]

[Summary] Construction on Shanghai municipality's first state-of-the-art fiber-optic-cable production line, installed at the Shanghai Cable Plant (SCP), has been completed. This information was disclosed to this writer yesterday by an SCP senior engineer, who noted that there are hopes to provide fiber-to-the-home services to Shanghai municipality residents within 10 years. This integrated production line, one of 14 key projects of the Shanghai Municipal Government, includes both imported and independently designed and manufactured equipment. It will produce a variety of fiber-optic-cable types, including mountain cable, cold-resistant cable, marine and river cable, multi-core (i.e., multi-fiber) cable, and military cable.

Overall investment for the new production line was 22.57 million yuan, annual designed output is 2,000 kilometers of cable, and annual industrial added value after three years of operation is estimated at 43.30 million yuan, amounting to 12 million yuan in taxes to the state.

### Shanghai Institutes Develop Fiber Packing Jelly

92P60010B Shanghai JIEFANG RIBAO in Chinese  
31 Jul 91 p 1

[Unattributed article: "Shanghai Develops Optical-Fiber Packing Jelly"]

[Summary] East China Institute of Chemical Engineering's Materials Science Research Division and Shanghai's Ziyou [5261 0645] Institute of Chemical Engineering, Science and Technology have jointly developed one of the key elements in the manufacture of fiber-optic cable—optical-fiber packing jelly. Moreover, they have received orders for the product from Germany's Siemens, the U.S.'s Corning, and Britain's Imperial Chemical Industries Co. After trials at the Tai Hu Communications Equipment Plant in Wuxi, the new material, which passed State Education Commission-sponsored ministry-level acceptance check yesterday, will be incorporated into the Shanghai Cable Plant's newly completed imported fiber-optic cable production line. This new line will provide much of the 800,000-odd kilometers of fiber needed for domestic fiber-optic-cable projects in the Eighth 5-Year Plan.

## Fiber-Optic-Cable, DMW, ISDN Projects Described

92P60010C Beijing KEJI RIBAO [SCIENCE AND TECHNOLOGY DAILY] in Chinese 27 Aug 91 p 1

[Article by Wang Hanlin [3769 5060 2651]: "Communications Technology Strides Into New Phase: Overall Has Reached Mid-Eighties International Level"]

[Summary] The nation's communications trunkline construction enterprises will completely convert to fiber-optic cable in the Eighth 5-Year Plan. This major change is a result of one of the priority projects in the Seventh 5-Year Plan, an MPT-sponsored project entitled "Communications Technology Development," which has now brought China's communications industry as a whole into a new era, equivalent to mid-eighties international levels.

Major achievements during the Seventh 5-Year Plan include commercialization of 34 Mb/s [DS3 standard] single-mode-fiber communications systems, installation of functional 140 Mb/s [DS4 standard] fiber systems, and development of key pieces of equipment for DS5 [565 or 622 Mb/s] fiber systems; conversion from multimode to single-mode fiber; domestic manufacture of complete municipal-telephone and long-distance-telephone stored-program-controlled (SPC) digital switchboards; development of complete 140 Mb/s digital microwave (DMW) systems, and construction of experimental 6 GHz 140 Mb/s DMW systems; completion of narrow-band integrated services digital network (ISDN) experimental network models; and realization of experimental coherent fiber-optic communications systems at research laboratories. In addition, industrial-scale pilot plants for manufacture of single-mode fiber are in operation, techniques for domestic manufacture of the quartz-glass tube used in optical fibers have been mastered, and a variety of optical devices and instruments used in fiber-optic communications have been domestically developed. Statistics released by MPT show that as of the end of 1990, 3,800 kilometers of fiber-optic lines incorporating domestically made equipment had been laid nationwide.

## Nanjing-Wuhan Line Formally Operational

92P60010D Beijing JISUANJI SHIJIE [CHINA COMPUTERWORLD] in Chinese No 34, 4 Sep 91 p 2

[Article by Xin You [2450 1429]: "Nation's Backbone Communications Network—Nanjing-Wuhan Fiber-Optic-Cable Line Formally Operational"]

[Summary] The nation's first high-capacity, long-range fiber-optic-cable communications trunkline, the 979-kilometer-long Nanjing-to-Wuhan line, has passed state acceptance check and is formally operational. This DS4 (140 Mb/s) single-mode long-wavelength fiber-optic transmission system incorporates equipment and cable imported from Germany, the United States, Japan, and Italy. This 107-million-yuan line now provides over

2,340 terminal circuits and 4,500 repeater circuits. It will be linked with the existing Beijing-Shanghai-Hangzhou and Nanjing-Wuhan-Guangzhou coaxial cable communications systems as well as with the just-recently-completed Beijing-Shanghai DMW system to form a nationwide backbone communications network that will greatly increase long-distance communications capability.

### Construction Begun on Xian Domestic Satcom Earth Station

92P60009A Xian SHAANXI RIBAO in Chinese  
30 Jul 91 p 1

[Article by Zhou Zhenqing [0719 2182 3237]: "Xian Domestic Satellite Communications Earth Station Construction Begun"]

[Summary] Ground breaking for the Xian domestic satcom earth station, located in Chang'an County, took place on 23 July. Outfitted with equipment imported from the United States and Canada by MPT with the aid of a foreign loan, the station will eventually have two 13-meter antennas and one 9-meter antenna. First-phase construction calls for one 13-meter antenna, which can be linked with the Intelsat Indian Ocean transponders to provide Shaanxi Province and the Xian area with 720 long-distance circuits in the near term and 960 in the long term.

Total investment for this project is estimated to be 24.18 million yuan; overall construction covers an area of

2,060 square meters. Cooperating on the design and construction of the project are the Shaanxi Province Radio Communications Office, the MPT Design Institute, the Xian Municipal Second Construction Engineering Co., and the Xian Co. of MPT's China Communications Construction Corporation. It is estimated that civil construction will be completed by the end of November this year, equipment will be installed early in 1992, and the station will be formally turned over for operation by the end of 1992.

### ISDN Digital/Analog Transmission System Developed

92P60009B Beijing ZHONGGUO DIANZI BAO  
[CHINA ELECTRONICS NEWS] in Chinese 2 Aug 91  
p 3

[Untitled photoreport, photo by Huang Jiwei and Wang Shunli]

[Summary] A digital/analog hybrid integrated services transmission system was recently developed by MPT's Institute 54. The new system's functions include transmission of telephone conversations, TV signals, and data. System design includes all-solid-state transceiving units. Main and back-up modules have both manual and automatic switchover.

[The photograph shows technicians testing the new equipment.]



### **Shandong Imports Digital Transmission System From Germany's SEL**

92P60009C Beijing ZHONGGUO DIANZI BAO  
[CHINA ELECTRONICS NEWS] in Chinese 9 Aug 91  
p 3

[Article by Yu Yu [3768 1342]: "Shandong's First Digital Transmission System"]

[Summary] Shandong Province's first digital transmission system, incorporating technology and equipment imported from Germany's SEL and funded with the aid of a German loan, became formally operational a few days ago. Consisting of a 22-station Jinan-to-Qingdao segment and a 10-station Yantai segment, as well as 32 other stations, the 140 Mbit/s [DS4 standard] wireless repeater system provides each segment with one operating channel and one guard channel; each channel can carry 1,920 simultaneous telephone circuits, or can carry TV broadcasts.

### **HDTV Included in MMEI's 10-Year R&D Goals for TV Industry**

92P60009D Beijing JINGJI RIBAO [ECONOMIC DAILY] in Chinese 26 Aug 91 p 3

[Article by Xie Shixin [6200 0013 2450]: "Nation's Color TV Industry Development Outline Becomes Clear: HDTV Development Strategy To Be Formulated Next Year"]

[Summary] The developmental outline for the nation's color TV industry in the last decade of the 20th century is now becoming clear. MMEI recently disclosed its four-point strategy:

(1) While maintaining the current domestic market share for mid-to-low-grade color TVs, efforts to accelerate development of new technologies should be increased. Annual production of color TVs in the remaining years of the Eighth 5-Year Plan will be 12-15 million; high-grade color TVs will be put into production, with a goal of 4 million sets to be exported. CAD technology will be applied to design of electronic tuners, including digital TV electronic tuners; and digital-IC-based TVs and frequency-synthesized remote control units will be developed.

(2) Product quality, especially quality of the "Zhonghua" [China] brand color TVs, will be further raised.

(3) Product design and development potential will be increased, principally with CAD/CAM technologies.

(4) The great significance of high-definition television (HDTV) technology should be fully recognized, and this technology should be developed and applied. Based on the nation's needs and the current domestic economic situation, the major strategic significance of the development of HDTV technology will be considered. Following upon the trends seen abroad, Chinese authorities are now organizing discussion groups and formulating

development strategies; it is estimated that a relatively clear-cut strategy—including a unified domestic HDTV [technical] standard—will be formulated by early next year.

### **Jiangsu Long-Distance Telephone Network's First High-Capacity DMW Trunkline Operational**

92P60009E Beijing DIANXIN JISHU  
[TELECOMMUNICATIONS TECHNOLOGY]  
in Chinese No 8, Aug 91 p 48

[Untitled news brief by Jin Yuqi [6855 6877 3825]]

[Summary] The Jiangsu Province long-distance telephone network's first high-capacity digital microwave (DMW) trunkline was put into operation on 8 May 1991. This trunkline, running from Nanjing through Yangzhou, Yancheng, Nantong, Wuxi, and Zhenjiang cities as well as Taizhou, Zhangjiagang, Dongtai, and other counties and towns, is 481 kilometers in overall length. Funded with a loan from Britain's Cable & Wireless PLC, this independently designed and constructed trunkline includes a DM-1000 140 Mbit/s [DS4 standard] DMW system imported from Japan's Fujitsu Ltd.

### **Survey of Domestic Public Packet-Switching Networks**

91FE0780 Beijing JISUANJI SHIJIE [CHINA COMPUTERWORLD] in Chinese No 27, 10 Jul 91  
pp 69, 71, 73

[Article by Gao Xingzhong [7559 2502 1813] of the Beijing Municipality Telecommunications Administration Bureau: "The Current Situation of China's Public Packet-Switching Networks"]

[Text] Trial operational observation and preliminary examination and acceptance of China's first public packet-switching network in Feb 1989 showed that it had the conditions for being opened to service. With the approval of the Central Telecommunications Bureau of the Ministry of Posts and Telecommunications, it was formally opened to the outside for service in Nov 1989. This network has a Network Management Center NMC composed of two computers and uses MINI 6/450 mini-computers from France's Bull Corporation in conjunction with special network management software, and it has implemented centralized management for all of China.

Initially, the network had three node computers PSX installed in Beijing, Shanghai, and Guangzhou and eight concentrators RCU installed in Shenyang, Tianjin, Nanjing, Xi'an, Chengdu, Wuhan, Shenzhen, and the Ministry of Posts and Telecommunications Data Institute. These node computers and concentrators use DPS25 II computers produced in 1984 by France's SESA Corporation (now merged to form the CAP-SESA Corp.). The concentrators use the same software as the node computers and also have local switching functions, but they do not have routing functions and their hardware and

equipment are held as mutual reserves. This network is for combined international and domestic use. The international output/input bureau is in the Beijing node computer and is interconnected with international public packet-switching networks.

### I. Network Structure and Service Functions

The interconnections among the node computers, concentrators, and Network Management Center are divided into two categories, carrier telephone line connections and permanent virtual circuit connections. Two dedicated four-line full duplex carrier telephone lines are currently used between the node computers with a speed of 9600 b/s and X.25 (automatic sequencing) multi-line protocol from France's SESA Corporation is used for communications. A four-line dedicated full duplex carrier telephone line is used between the node computers and concentrators with a speed of 9600 b/s and using the X.25 protocol. With the exception of the Beijing-Chengdu link, which can only operate at a speed of 4800 b/s because it uses a microwave circuit, all of these circuits operate at a speed of 9600 b/s according to CCITT M.1020 proposals. There are two four-line full duplex circuits with a speed of 9600 b/s between the Network Management Center and the Beijing node computer and it uses the X.25 protocol. The Beijing International Output/Input Circuit has dedicated direct satellite carrier telephone circuits to the United States and France, both of them full duplex circuits with a speed of 9600 b/s and using the X.75 protocol.

At present, there are 48 permanent virtual circuits in the network. There is a permanent virtual circuit between the primary and reserve equipment at the Network Management Center that is used for dialogues to enable an automatic switchover to the reserve equipment in the event of a breakdown of the primary equipment. There are two permanent virtual circuits between the Network Management Center and each of the node computers and concentrators that are used for, respectively, technical service contacts and collecting charge data information. There is a virtual circuit among the three node computers that is used for service contacts.

The network can provide three types of service functions for subscribers:

#### A. Basic service functions

For the switching virtual circuit (SVC), when two subscriber terminals are communicating, they must first make a virtual call and establish the virtual circuit. When they finish communicating, the virtual circuit is released. For the permanent virtual circuit, there is no need to call to communicate between two subscriber terminals because the virtual circuit is a permanent connection and has dedicated circuit connection functions.

#### B. User selectable supplementary service functions

The DPS25 II computer provides all CCITT X.25 suggested (1984 edition) selectable services, more than 27 types altogether such as closed user groups (CUG), bilateral closed user groups, direct calling, user identification (NUI), charge reversing, abbreviated dialing, expanded packet sequence coding (mode 8 or 128), selectable window size (2-7), non-standard temporary selectable packet lengths (32, 64, 128, 256 bytes/packet), temporary selectable through-put levels (50, 100, 150, 200, 300, 1200, 2400, 4800, 9600, 48000 b/s), closed user group incoming call closure and outgoing call blocking and allowable outgoing calls and allowable incoming calls, regular user incoming call blocking and outgoing call blocking to restrict them to being able to make outgoing calls from this logical channel but not incoming calls or to only be able to make incoming calls and not outgoing calls, rapid selection, charge information notification, call transferring, joint use of a single users code by multiple terminals, multi-line users, and user service functions provided by packet assembly/disassembly devices PAD.

#### C. New service functions include Teletex, Videotex, and so on.

### II. User Terminal Types

The DPS25 II node computers and concentrators permit the following types of terminals to enter the network:

1. Synchronous packet-type terminals connected via a dedicated line. These terminals must conform to the CCITT suggested X.25 protocol.
2. Synchronous packet-type terminals connected via telephone switching networks PSTN. These terminals must conform to the CCITT suggested X.32 protocol.
3. Asynchronous character-type terminals. These terminals must conform to the CCITT suggested X.3, X.28, and X.29 protocols.
4. Telex terminals connected via the Telex network.
5. Videotex, French-made terminals which conform to European standards.
6. Terminals which conform to the IBM SNA/SDLC protocol. Because the network only imported a few models, at present it cannot provide an entire module for use by this protocol.

Communications between the packet network and Telex network and public telephone network and at present only permit users on asynchronous terminals to call packet networks on the Telex network and public telephone network at present, and will also permit reverse calling in the future. Users on the Telex network connected to the Beijing node computer are connected to the packet network via a dedicated interface (Telex PAD arrangement). When asynchronous user terminals on the telephone network wish to connect to the public packet

network, they must first submit an application and the Network Central Control Station will provide them with a definition and establish a user code. After this, the dialing arrangement is used to dial up the special number to connect with the packet network (it can be the special service number 1XX or it can be the telephone connect continuously selectable number). When the circuit is opened, the network user identification (NUI) can be entered to enable identification and charging by the network. Only then can the packet network's called number on the network be entered.

### III. Primary Technical Properties and Operating Indices of the Network

1. System capacity. Each node computer can be composed of 20 to 40 DATEM modules that are interconnected via a dual-bus arrangement, with a bus speed of 10 Mb/s. Each module can be connected to as many as 90 terminals. Thus, each node computer can be connected to roughly 700 to 1,500 terminals depending on the speed of the connected circuit and the actual required configuration.

2. System throughput capacity. Each module can handle 90 packets/second (when the packet length is 128 bytes) and has been measured at 96.2 packets/second. The call processing capacity of each module is 12 times/second and has been measured at 18.8 times/second. Calculated at 20 modules each, a node computer would have a throughput capacity of  $(20 \times 96.2)/2 = 1,000$  packets.

#### 3. Network time delay

a. The virtual circuit setup time averages less than 1.1 second and has been measured at 30 ms to 490 ms (the former is for users on the same node computer, the latter is via three node computers).

b. Time delay of data packets on the packet network: when the data packets do not pass through a concentrator, the average time delay should be less than 150 ms and has been measured at 16 to 32 ms (under the same conditions as a.). When passing through a concentrator, the average time delay of the data packets should be less than 450 ms and has been measured at 380 ms.

4. Network trunk line error rate. Under control by multilink protocol, if the trunk line transmission quality can be held at a  $1 \times 10^{-5}$  error rate (the CCITT suggested standard for speeds of 9600 b/s and below), the network error packet rate would be better than  $1 \times 10^{-8}$  (equivalent to an error rate of better than  $1 \times 10^{-10}$ ).

5. System availability rate. The requirement was 99.9 percent, and was measured at 99.97 percent after 3 months of trial operation.

6. Mean time between failures (MTBF) of virtual circuits. Provisions state this should be greater than 80 hours. The results in actual operation (by a computer automated system) showed that between each of the node computers and the Network Management Center, they were, respectively:

Beijing 144 hours, Shanghai 246 hours, and Guangzhou 253 hours.

7. Results of long-distance relay circuit testing. Testing of the four carrier telephone circuits linking the Network Management Center with Beijing was conducted based on the basis of CCITT M.1020 proposals using a K1190 digital circuit analyzer, HP4945 line damage analyzer, DF-64 error tester, PT-80 printer, and other equipment. This mainly involved testing the amplitude characteristics, group time delay, reflection losses, harmonic distortion, impedance measurement, noise level, phase jitter, level deviation, frequency drift, pulse noise, transient interrupts, errors, and so on. Overall, the circuit quality can meet the requirements for being opened to digital communications. The quality is not high, however, and in particular there are quite a few transient interrupts during busy periods, most apparent daily from 0900 to 1100 hours, 1300 to 1600 hours, and 1900 to 2100 hours when there are frequent long distance calls. The error rate of most domestic circuits is better than  $1 \times 10^{-5}$ , but some are  $1 \times 10^{-4}$  and are somewhat worse at busy times. The quality of international satellite circuits like the Beijing-Paris and Beijing-New York circuits is excellent, with extremely few transient interrupts and error rates better than  $1 \times 10^{-7}$ .

### IV. User Network Entry Experiment Conditions

1. Asynchronous terminal entry to network. Regular terminals with asynchronous terminal two-line full duplex and speeds of 1200 b/s that conform to the X.28 protocol like VT-100, Module 925, 301, IBM PC AT/XT, 286, 386, and so on can enter the network. Another example is users on public telephone networks, which are also two-line full duplex asynchronous terminals with a speed of 1200 b/s. In addition, 1200/75 speed Videotex via public telephone networks can also operate normally.

2. Synchronous terminal entry to network. Most synchronous terminals conforming to the X.25 protocol that use 2400 b/s two-line full duplex or 2400/4800/9600 b/s four-line full duplex patterns for communication are microcomputers configured with an X.25 interface board and software to turn them into X.25 protocol terminals. Examples include the TOP25 imported from DATA CRAFT in New Zealand, which can create eight logical channels; the United States' S.COM25 X.25 interface that can create 32 to 128 logical channels; and Canada's EICOM 25 X.25 interface, which can open 16 to 64 logical channels. These three interfaces can all operate in IBM PC AT/XT and 286/386 computers. The Beijing Municipality Telecommunications Administration Bureau has also conducted experiments with the Ministry of Posts and Telecommunications Data Institute X.25 interface microcomputer, the Beijing Posts and Telecommunications College X.25 microcomputer, the Beijing Fangxing Information Institute X.25 microcomputer, the Fudan University and Changzhou Computer Plant microcomputer terminal, the Southeast China University X.25 synchronous 9600 b/s and asynchronous (maximum of 19.2 Kb/s) protocol converter,



the Beijing Posts and Telecommunications Bureau X.25 and SNA/SDLC protocol converter, and so on which confirmed that they can operate normally when entering the network.

3. Telex interface. Telex terminals with a 50 b/s speed (with a total of eight continuously selectable interfaces) can connect with any user on the public packet network via the Telex network and communicate normally.

4. Connection with mainframe computer networks (large, medium-sized, and small computers). A series of experiments indicate that the following mainframe computers can enter the network via X.25 terminals or protocol converters: PDP 11/73, DEC Corp. VAX750, IBM 420/AS, HP3000, VAX785, IBM 4381, 4361, DPS 7000, and all other machines in the packet network of a certain ministry which have X.25 interfaces can enter the network.

5. Network connection experiments with packet assembly/disassembly equipment (PAD). We conducted network entry experiments with the PAD-A2 and PAD-C developed by Institute 1930 in the Ministry of Machine-Building and Electronics Industry, the PSX and PAD developed jointly by Qinghua University and the Nanjing Communications Equipment Plant, the PAD-16 from the Ministry of Posts and Telecommunications Data Institute, the PAD from France's (Saite) Company, the PSX and PAD from Holland's Phillips TRT Company, and so on, and all of them operated normally.

Moreover, during the Asia Games, we used the PAD produced by Qinghua University to connect to the packet network via an optical cable circuit. The asynchronous terminal of the PAD was connected to the Asia Games electronic computer STRATUS X2000 fault-tolerant computer and provided real-time searches of the Asian Games results announcement system for Japan, South Korea, Hong Kong, and other countries and regions which were welcomed and praised by users.

#### V. The Situation for Opening Up to International and Domestic Users

1. International circuits. We have now opened the Beijing-Paris NTI (International Packet Network Output/Input Bureau) and Beijing-WU Company in New York, the United States (now merged with the ITT Corp. to form the World Com Corp.) and, based on service requirements, we have also opened it to Tokyo, Hong Kong, and other places. At present, we are also testing its opening via public packet networks in the United States and France to 18 countries and regions including Argentina, Australia, Belgium, Brazil, Canada, Chile, Germany, South Korea, Malaysia, Mexico, Holland, New Zealand, Singapore, Sweden, Japan, and so on. The Ministry of Posts and Telecommunications has formally issued charge standards for only the United States,

France, Germany, Belgium, Sweden, Switzerland, Singapore, Hong Kong, Canada, Australia, and other countries and regions. Although some countries and regions have apportioning agreements, they have not been opened on a trial basis.

2. Domestic circuits. All those in the original plan have been opened up. They include the Beijing-Shanghai, Beijing-Guangzhou, and Shanghai-Guangzhou dual telephone channels, the Beijing-Tianjin, Shenyang, Wuhan, Chengdu, and Xi'an single telephone channels, the continuous municipal telephone line used from Beijing to the Data Institute, and single telephone lines from Shanghai-Nanjing and Guangzhou-Shenzhen. Most of these lines use cable circuits of rather good quality. There are also 10 telephone continuously selectable numbers connecting the Beijing node computer and the municipal telephone network for users on the telephone network to connect to. There are also eight continuously selectable numbers connected to the Telex network for connection by users on the Telex network.

3. User network entry utilization situation. From the opening of service in November 1989 to the end of December 1990, there were a total of 209 users (not including experimental interfaces). Divided according to speed, there were five at 9600 b/s, 32 at 4800 b/s, 25 at 2400 b/s, and 147 at 1200 b/s. Divided according to the type of user network entry terminal, there were 62 synchronous, 28 asynchronous, and 119 telephone dialing. Dividing according to region and city, there were 93 in Beijing (A) and seven in Beijing (B) for a total of 100, and there were 52 in Shanghai, 22 in Guangzhou, 10 in Tianjin, nine in Shenzhen, six in Nanjing, four in Shenyang, three in Chengdu, two in Xi'an, and one in Wuhan. Divided according to the qualities of Chinese and foreign users, businesses and agencies in foreign countries accounted for 23 percent and organs of foreign countries located in China and news agencies accounted for 12 percent, for a total of 35 percent. Chinese foreign trade enterprises accounted for 18 percent, scientific research organs for 15.4 percent, institutions of higher education for 5.2 percent, and Chinese commercial enterprises for 26.4 percent, for a total of 65 percent. In terms of the amount of service, however, organs and companies of foreign countries accounted for about two-thirds of the total network, and most were electronic mail and international information searches. The proportion of communications and information searches within China was relatively small.

#### VI. Charge Standards for User Entry Into the Network and Use

The charge principles for the public packet-switching network were identical to those of international customs, meaning basic charges with added communications charges:

1. Basic charges. All terminals or computers which connected via dedicated circuits paid monthly charges according to their communications speed, with higher

prices for higher speeds. If they entered the network via PSTN or Telex, they were required to register the user network identification NUI and were charged each month.

2. Communications charges. Charges were made according to the amount of information transmitted and received and the duration of the communications. The unit of the amount of communications was the Segment and each segment was 64 8-bit information groups (Octet). The communications time was in minute units.

3. Selectable function charges. If a user selected a closed user group, transfer calling, recipient payment, rapid selection, or other added functions, they were also charged each month.

4. Other charges. These include initial installation charges, charges for modems rented from telecommunications departments and user circuit testing dedicated line charges, protocol examination and acceptance charges, user identification NUI, and other charges.

The current charging standards for the public packet-switching network are:

a. Initial installation charge: 100 yuan/user.

b. The following table shows the charges for different speeds:

Table 1. User Charges for Different Communications Speeds (Yuan/Month)

Item	Speed			
	1200 b/s	2400 b/s	4800 b/s	9600 b/s
Basic charge	150	200	300	400
Inner-city circuit testing	200	400	600	800
Modem rent	120	200	280	400

c. Protocol examination and acceptance charge: 300 yuan for X.25, 100 yuan for X.28.

d. Communications charge: 0.20 yuan/minute and 0.025 yuan/segment inside China, 0.08 yuan/minute and 0.07 yuan/segment for international and Hong Kong and Macao.

e. Charge for using NUI: 10 yuan/month.

## VII. Problems That Exist and Countermeasures

1. Small coverage area. We now cover only 10 cities, which cannot meet the requirements of all users. The common desire is to cover at least 30-plus cities where provincial CPC Committees are located. Ministry of Posts and Telecommunications plans call for the use of Chinese-made PAD equipment to be extended to provincial CPC Committee cities, including several coastal cities, by the first half of 1991. Second, we must expand the capacity of existing network equipment and increase the number of terminal modules and expanded the number of locations reached internationally, and make appropriate increases in the speeds between node computers in order to meet the needs of growing numbers of users. At the same time, we should reinforce guidance over packet networks established by provinces and municipalities. Based on the requirements of the China Public Packet-Switching Network Technology System which call for a single network and single system, the provincial packet networks now being established in Guangdong, Sichuan, Jiangsu, and other provinces are included in the large network system and use interface interconnection to foster the benefits of the entire network.

2. Small number of circuits. For example, in some regions where there are rather concentrated users, user

needs cannot be met. The large number of inner-city relays supplied to the fields and halls during the recent Asia Games were DS 1 digital circuits with a speed of 2 Mb/s in the inner-city fiber optic transmission network that were broken down into some analog four-line circuits and some 64 Kb/s digital circuits. The former served directly as Asia Games computer relays and other non-voice services like providing FAX, Telex, and public telegram services. The latter were turned into XC-64 digital data networks based on 64 Kb/s and used the CCITT X.50 suggested interface protocol to provide 1200-9600 b/s up to 19.2 Kb/s digital data circuits and were available for users in a semi-permanent connection arrangement. They have now been linked into 10 tandem points that are administered by the Network Control Center. They are expected to provide services by the first half of 1991. This can solve the problem of numerical inadequacies, and it can solve the problems of overly-long relays, high attenuation, and poor continuity caused by old cable construction and wrapping which have prevented the opening up of moderate and high-speed data circuits. In addition, the Beijing region is now in the process of accelerating construction of a domestic small satellite data communications system (VSAT) to compensate for inadequate ground-based networks. It can provide point-to-point circuits at a speed of 64 Kb/s and under, and it can be connected with the public packet network to build a Chinese Public Packet-Switching Network with even broader coverage.

3. Poor quality of domestic long-distance transmission lines. This is mainly embodied in the instability of the quality of domestic carrier telephone circuits. For example, in the major Beijing-Shanghai, Beijing-Guangzhou, and Shanghai-Guangzhou channels, there are quite a few transient interrupts caused by overloading of coaxial cable circuits which have negative

effects on data transmission but relatively few effects on conversations. Observations over a 24-hour period show three peaks in the occurrence of transient interrupts during three periods during the morning, afternoon, and evening, all of them periods of busy voice services. One countermeasure is renovation and rectification of transmission levels and solving the problem of overloading on major channels. Another is to open the Beijing-Shanghai digital microwave circuit and Shanghai-Wuhan optical cable as soon as possible and to open the Beijing-Guangzhou domestic satellite circuit as soon as possible.

4. Mainframe computer protocol interface problems. Large and medium-sized computers in China like the IBM 43 series and 30 series machines, Siemens computers, VAX and M series, Univac 1000, and other machines were imported rather early and initially were not configured with X.25 protocol interfaces. There are two ways to solve the network entry problems of these machines. One is to configure them with the necessary hardware and software to enable them to connect to the packet network. The second is to use PAD, synchronous protocol converters, and other methods to solve the problem. Many units in China now have such products.

5. Charging problems. In the area of domestic charges, it is more convenient for users to use the domestic long-distance dialing network than the packet network, but the quality is not as good as the packet network so many users consider the economy of using this network. Information from the related areas indicates consideration is now being given to whether or not some users can receive preferential measures for a period of time.

6. Database and information source problems. Because China has just begun developing an information industry, our computers are mainly used to collect and arrange information for use by leaders in decision making and they have not been widely opened to society. Added to the fact that China uses a combined planned economy and market regulation to organize production and marketing, there is still a problem of information security. Thus, there are still few effective, applied, systematic, and accurate databases (including public and special-purpose ones) oriented toward society. The collection, handling, processing, analysis, distribution, and application of information sources have still not become forces of production. According to analysis by the relevant authoritative departments, only about 5 percent of our databases can be opened up to and used by society. All of the remaining ones are specialized databases established and used by those who made them. There are also various types of communications and information value-added services (VAS) such as Videotex, data processing, graphics services, scientific computing, electronic mail, text electronic processing, office automation, basic telecommunications facilities, and so on that are very backward compared to the industrially developed nations which have obstructed the rapid development of our information industry.

## VIII. Development Prospects

According to statistics from the International Telecommunications Union (ITU), there were a total of 214 public data networks operating in 87 countries and regions of the world at the end of 1987, and two-thirds of them were public packet-switching networks. Moreover, many countries and regions have adopted policies to support and restrict the development of public packet-switching data networks but they are making great efforts to develop public packet-switching data networks. Many developing nations are now building and expanding public packet networks and countries like France, the United States, Japan, and others where integrated service digital networks (ISDN) have developed more quickly are making major efforts to expand their public packet networks to meet the ever-growing need for information communications.

1. Forecasting user demand is an important basis for public packet-switching network development. From the macro perspective, the scale of data communications networks should be closely related to a nation's economic situation, socioeconomic environment, existing basic telecommunications facilities, and so on. From the micro perspective, it should have a positive relationship to the number and applications levels of all types of computers of a region as well as the degree of maturity of all types of databases and its capacity for developing data processing. In a developing country, government departments and public service activities occupy an extremely important status in society. This is particularly true in China. With the exception of foreign commerce and foreign affairs organs, they first should serve computing centers and information centers in all major departments of the national economy like planning commissions, S&T information and commercial systems, news management departments, foreign economics and trade organs, institutions of higher education, scientific research organs, and all ministries and commissions of the central authorities.

2. Developing data communications requires full motivation of initiative in all areas. Data communications is a new method of communications outside of traditional telecommunications like telegraph, telephone, FAX, and Telex. Actually, it provides the conditions for substantial VAS. It integrates the organic relationships among information suppliers (all types of databases), information users, information exchangers (telecommunications), and information equipment manufacturers and serves society. It is a form of systems engineering, so it is extremely necessary that we establish organs (both official and civilian) for greater coordination and integration to spur the development of China's data communications.

3. Actively develop all types of new services in public packet-switching networks. For example, we are now considering services that we should have like Videotex, text processing systems (conforming to X.400 proposals), simple electronic mailboxes (EMail), Teletex,

remote monitoring, emergency reporting, and so on as well as various types of public and special-purpose databases to fully develop and utilize public packet-switching network resources. In the short term, various types of data and information processing and transmission, postal service collection, bank transfer account services, remote data processing, scientific computing, S&T information searching, news and information inquiries, and so on can undergo trial utilization on the network to provide information circulation services for all industries.

4. Develop Chinese-made packet-switching equipment as quickly as possible. Examples include node computers and concentrators as well various value-added services on the network. On the basis of existing backbone networks, use as much Chinese-made equipment as possible for network terminal equipment like PSX, PAD, X.25 protocol microcomputer terminals, various protocol converters, and so on. This can spur development of domestic industry and conserve foreign exchange, and we can wait until the technology is mature to develop our own large-scale node switching computers and matching network management center equipment to catch up with advanced international levels as quickly as possible.

**Fast Acquisition of Inbound Signal Under Low Signal-to-Noise Ratio Condition in RDSS System**

40100083A Beijing ZHONGGUO KONGJIAN KEXUE JISHU [CHINESE SPACE SCIENCE AND TECHNOLOGY] in Chinese Vol 11 No 3, Jun 91 pp 24-35

[English abstract of article by Ye Fei and Lu Wenfu of the Beijing Institute of Information Engineering; MS received 20 Oct 90]

[Text] An overall analysis on various kinds of possible methods of fast acquisition in view of the whole system is presented. Precise mathematical models have been established and used to analyse the influences of PN [pseudorandom noise] pattern, Gaussian noise and Doppler frequency shift on the performance of PN code acquisition. Computer-aided analysis gives some quantitative and qualitative results which indicate that SAW [surface acoustic wave] matched filter is the best choice.

Theoretical analysis is also given to the recommended RDSS [radiodetermination satellite services] standard inbound PN pattern. One possible fast acquisition method has been conceived according to this pattern.

**References**

1. Martin A. Rothblatt, "Radiodetermination Satellite Services and Standards," 1987.
2. Marvin, K. S., et al., "Spread Spectrum Communication," 1985.
3. R. C. Dixon, "Spread Spectrum Systems," National Defense Industries Publishing House, 1982.
4. Joseph H. Yuen, "Deep Space Telecommunications Systems," 1985.
5. Wu Zhongyi, et al., "Pseudorandom Sequence Techniques," Harbin Institute of Technology Publishing House, 1986.
6. Kowatsch, M., "Synchronization in a Spread Spectrum Communication Modem Based on SAW Convolvers," PROC. IEEE MILITARY COMMUNICATIONS CONFERENCE, 1984, 125-130.
7. Kowatsch, M., "Burst Communication Modem Based on SAW Elastic Convolvers," IEEE ULTRASONIC SYMP. PROC., 1982, 262-267.
8. Morgan, D. F. and Hannach, J. M., "Surface Wave Recirculation Loops for Signal Processing," IEEE TRANS. SONICS AND ULTRASON., SU-25, 1978, 30-42.
9. Hjelmstad, J. and Skaug, R., "Fast Synchronization Modem for Spread Spectrum Communication System Using Burst-Format Message Signalling," IEEE PROC., Vol 128, Pt. F, 1981, 370-378.
10. Brodtkorb, D. and Lagnor, J. E., "Fast Synchronization in a Spread Spectrum System Based on Acoustoelectric Convolvers," IEEE ULTRASON. SYMP., 1978, 561-566.
11. Kowatsch, M., "Design of a Convolvers-Based Packet Voice Spread Spectrum System," IEEE ULTRASON. SYMP., 1984, 127-131.

### Lanzhou Heavy-Ion Accelerator Physics Experiments Terminals Certified

91FE0720A Lanzhou LANZHOU KEJI QINGBAO [LANZHOU S&T INFORMATION] in Chinese No 1, Feb 91 p 17

[Article by Song Wenjie [1345 2429 2638]: "Lanzhou Heavy-Ion Accelerator Physics Experiments Terminals and Public Experimental Facility Certified"]

[Text] Lanzhou heavy-ion accelerator physics experiments terminals and public experimental facility, the largest of its kind in China, was certified and accepted by experts from the Chinese Academy of Sciences (CAS) on 14 October 1990.

The physics experiments terminals are apparatuses which employ heavy-ion beams provided by the accelerator to conduct physics experiments. Usually, the system is very sophisticated and large. The eight terminals certified, including the large-area position-sensitive ionization chamber, in-situ gamma-ray detection apparatus, in-line isotope separator, large spherical scattering chamber, fast chemical separation apparatus, heavy-ion time-of-flight spectrograph, atomic physics research apparatus and heavy-ion radiation device, as well as the four public facilities, were built by the Institute of Modern Physics beginning in 1984. With these terminals, scientists can conduct research on heavy-ion physics, atomic physics, solid-state physics, materials science, radiation biology and radiation medicine.

The appraisal committee, consisting of 15 experts from the CAS and 11 other research and higher learning institutions, believes that the design, machining, installation and testing of these eight experiment terminals is a success. All major technical specifications have been met or exceeded. Some specifications are at a world-class level for similar equipment. The large-area position-sensitive ionization chamber, in-line isotope separator and heavy-ion radiation apparatus are officially open to the users to conduct eight heavy-ion physics experiments. Some experiments have yielded good results. The four public facilities have been used in numerous experiments and have proved to be reliable; they meet the needs. In particular, the data acquisition and processing system and the public NIM instrument warehouse provide considerable service to the users.

### Design Calculations for Improved ECR Ion Source

91FE0720B Beijing GAONENG WULI YU HE WULI [HIGH-ENERGY PHYSICS AND NUCLEAR PHYSICS] in Chinese Vol 15 No 4, Apr 91 pp 343-348

[Article by Xu Yongxing [6079 3057 5281], Liu Zhanwen [0491 0594 4489], and Wei Baowen [7614 1405 2429] of the Institute of Modern Physics, CAS, Lanzhou, 730000: "Design Calculations for Improved ECR Ion Source"; MS received 28 Jul 89]

[Text]

### Abstract

The design concept of an ECR [electron cyclotron resonance] ion source with a  $\omega_{\text{ecr}}$  resonance surface and a  $2\omega_{\text{rf}}$  enclosed equigauss surface is presented. In addition, this paper also shows the design data for a 0.8 T axial mirror field and a 0.8 T radial hexapole confined field. The calculation shows that the axial expansion of the  $\omega_{\text{ecr}}$  resonance surface of this improved ECR ion source is significantly higher than that of the imported CAPRICE ion source. Furthermore, it produces an enclosed  $2\omega_{\text{rf}}$  equigauss surface. These design parameters indicate that the intensity of highly charged ion beams may be raised substantially.

### 1. Introduction

An ECR ion source is a plasma device which is heated by cyclotron resonance through the use of an axial and radial magnetic field. It is usually divided into two stages. The first stage produces a cold, high-density plasma which diffuses into the second stage. After heating, it becomes a high-temperature, low-density plasma. Ionization occurs gradually through multiple collisions between ions and electrons to produce highly charged ions. This type of ion source can produce a beam of highly charged ions of a certain intensity and quality (emissivity and energy dispersion). Moreover, it can operate continuously over a long period of time and has a long lifetime. These are advantages beyond comparison which makes it very popular in heavy-ion nuclear physics and atomic physics.

In order to extend its capability and raise the single-particle energy, HIRFL (Heavy Ion Research Facility at Lanzhou) is in the process of installing a CAPRICE ECR ion source. The operating principle, structural characteristics and confinement magnetic field distribution of this type of ion source have been described elsewhere.<sup>1</sup> Since HIRFL consists of a standard fan cyclotron (SFC) with an energy constant  $K = 69$  and a separated sectors cyclotron (SSC) with an energy factor  $K = 450$  in series, the matching efficiency of the two accelerators and the stripping efficiency of the stripper vary between 1 and 23 percent. If the transport efficiency of every segment and the efficiency of each accelerator are included, then the overall efficiency is even lower. Typically, an ECR ion source produces 12  $\mu\text{A}$  of  $\text{Xe}^{19+}$  and the current intensity after vertical injection and SFC acceleration is estimated to be 0.48  $\mu\text{A}$ . The stripping efficiency to produce  $\text{Xe}^{35+}$  is 12.61 percent and the current is 0.06  $\mu\text{A}$ . Finally, the beam current after the front transportation line and SSC acceleration is  $3.6 \times 10^{-3}$   $\mu\text{A}$ . This shows that the intensity of the final highly charged ion beam is very limited. In order to satisfy the requirement of various experiments, raising the current density is an important issue. One way to solve this problem is to increase the productivity of the ECR ion source. In view of the fact that the ECR ion source is a rapidly growing technology, in order to be able to track the next generation of ECR ion source, an improved ECR ion-source design scheme based on the CAPRICE ion source is

proposed. Its axial magnetic field is different from the current design concept abroad. A desired radial magnetic field is established without altering the structure of the original permanent magnetic elements.

## II. Design Concept of the Improved ECR Ion Source

The fundamental mechanism of the ECR ion source is to effectively transport high-frequency power to the second-stage plasma through cyclotron resonance with a fixed axial and radial magnetic field. Based on the Larmor equation, the resonance frequency is

$$\omega_{\text{ecr}} = \omega_{\text{rf}} = eB/m_e c, \quad (1)$$

where  $\omega_{\text{ecr}}$  and  $\omega_{\text{rf}}$  are the resonance frequency and HF frequency, respectively,  $B$  is the resonance magnetic field, and  $e$  and  $m_e$  are the electron charge and mass, respectively. Once the HF frequency is determined, there is an equigauss surface in the source cavity, usually called an ECR resonance surface, as shown in Figure 1. Electrons penetrate the ECR resonance surface many times to achieve acceleration in a statistical sense. This leads to the increase of plasma electron temperature which makes it possible to generate highly charged ions. Because the ECR resonance surface is surrounded by a plasma containing high-temperature electrons, the intensity of the highly charged ion beams is to a large extent determined by the size of the resonance surface and the density of high-temperature electrons. There are several ways to raise the beam intensity of an ECR ion source.

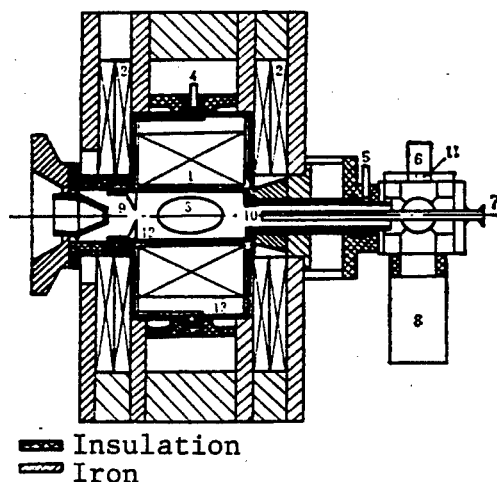


Figure 1. Structure of ECR Ion Source

Key: 1. Permanent magnet; 2. Coil; 3. ECR resonance surface; 4, 5. Cooling water inlet and outlet; 6. Waveguide; 7. Inlet of working gas; 8. Molecular pump; 9. Ion source outlet; 10. Gas inlet tube; 11. Microwave window; 12. Plasma cavity; 13. Permanent magnet assembly rack

### 1. Increase Microwave Frequency

A highly charged ion beam of a certain intensity is closely related to the Lawson criterion of  $n_e \tau$ , where  $n_e$  is the electron density and  $\tau$  is the ion confinement time. The rate for an ion to go from charge state  $i$  to  $i + 1$  is proportional to the electron density.<sup>1</sup> Therefore, the intensity of the highly charged ions is directly proportional to the high-temperature electron density. However, plasma physics points out that microwaves can no longer propagate in a plasma once its electron density exceeds a certain level  $n_c$ , which is the cutoff frequency and which is given by:

$$n_c = \frac{\omega_{\text{rf}}^2 m_e \epsilon_0}{e^2},$$

Here,  $\epsilon_0$  is the dielectric constant in vacuum, and  $e$  and  $m_e$  are the charge and mass of an electron, respectively. Therefore, increasing the input microwave frequency is one way to improve the intensity of a highly charged ion beam. R. F. Bourg<sup>2</sup> tried to raise the frequency of the Minimafox ECR ion source from 10 GHz to 16.6 GHz to improve its performance. The operating frequency of the CAPRICE ECR ion source is also at 10 GHz. Based on our present operating budget, it is difficult to acquire a new transmitter. Hence, this approach was abandoned.

### 2. Lengthen Second-Stage Source

Based on the above analysis, lengthening the second-stage source to extend the axial magnetic mirror field to enlarge the ECR resonance surface axially is another way to raise the highly charged ion-beam intensity. In the early development stage of the CAPRICE ECR ion source, B. Jacquot<sup>3</sup> lengthened the second-stage ion source from 14 cm to 16 cm. This increases the volume surrounded by the ECR resonance surface somewhat which raises the microwave input power from 250-300 W to 500-600 W. This requires considerable changes in the geometry of the source; hence, it is not desirable.

### 3. Adjust Axial Magnetic Mirror To Extend ECR Resonance Surface

The profile of the axial double-peak magnetic mirror directly determines the size of the ECR resonance surface. It is possible to insert an appropriate iron element without raising the coil current. The peak magnetic field is increased while its width is reduced. This makes the valley between the two peaks wider. Without lengthening the source, the enclosed resonance surface can be enlarged. Nevertheless, the selection of an appropriate magnetic element requires precision analysis and computation. Since we have considerable experience in this field, this approach is still very attractive.

#### 4. 2 $\omega_{rf}$ Operating Mode

As the research on the mechanism of ECR ion sources progresses, a new concept<sup>4</sup> has been established. In addition to the classical operating mode,  $\omega_{ecr} = \omega_{rf}$ , an ECR ion source has another operating mode, i.e.,  $\omega_{ecr} = 2\omega_{rf}$ ,  $3\omega_{rf}$ , ..., as long as the equigauss surface of the corresponding B field is enclosed in the source cavity. Although there is still some controversy associated with this new mechanism, it is commonly agreed upon that the new operating mode would be beneficial to improve plasma confinement. It is estimated that the ion-beam intensity generated by both  $\omega_{rf}$  and  $2\omega_{rf}$  surfaces is approximately four times that produced by  $\omega_{rf}$  alone. In order to produce an enclosed  $2\omega_{rf}$  equigauss surface, further analysis of the axial and radial magnetic field is necessary. Of course, the  $\omega_{rf}$  resonance surface of the CAPRICE ECR ion source is enclosed with certain specific axial and radial magnetic field parameters. However, because the magnetic field is always low, the equigauss surface for  $2\omega_{rf}$  is not enclosed. Therefore, it is impossible to operate in this new mode with existing parameters. Considering the fact that the present transmitter operates at 10 GHz and the corresponding resonance magnetic field is 0.36 T, from equation (1) the magnetic induction strength corresponding to the  $2\omega_{rf}$  enclosed surface is 0.72 T. Hence, the two axial field peaks must be greater than 0.72 T; otherwise, the  $2\omega_{rf}$  equigauss surface is not enclosed on the axis. Furthermore, the radial maximum hexapole field must be raised from 0.4 T to around 0.8 T; otherwise, the  $2\omega_{rf}$  equigauss surface might hit the vacuum chamber wall and cannot be enclosed in the cavity. Obviously, based on the magnetic field achievable inside an ECR ion source, it is extremely difficult to produce an enclosed  $3\omega_{rf}$  equigauss surface.

Based on the above analysis, in view of our present situation, it is appropriate to take steps 3 and 4. First, the present magnetic structure is altered by inserting an iron element to raise the peak axial field to approximately 0.75 T without increasing the coil current. This is to enlarge the geometric size of the  $\omega_{rf}$  resonance surface and provide the necessary condition to establish the  $2\omega_{rf}$  equigauss surface. Furthermore, it reduces the width of the axial magnetic field peak to facilitate the transport of highly charged ions and to raise the beam intensity. Next, in order to produce an enclosed  $2\omega_{rf}$  equigauss surface, the maximum radial hexapole field must be increased to 0.8 T. These targets become the basis for the following axial and radial magnetic field design.

#### III. Design Computations for Radial Magnetic Field

From the overall design consideration, the maximum radial magnetic field must reach approximately 0.8 T. Based on the optimal performance of permanent magnets available, the original hexapole structure is not adequate.<sup>1</sup> In order to reduce the magnetic flux path in air, the new structure involves the insertion of a permanent magnet of similar material and proper orientation between the poles with a magnetization strength M, as

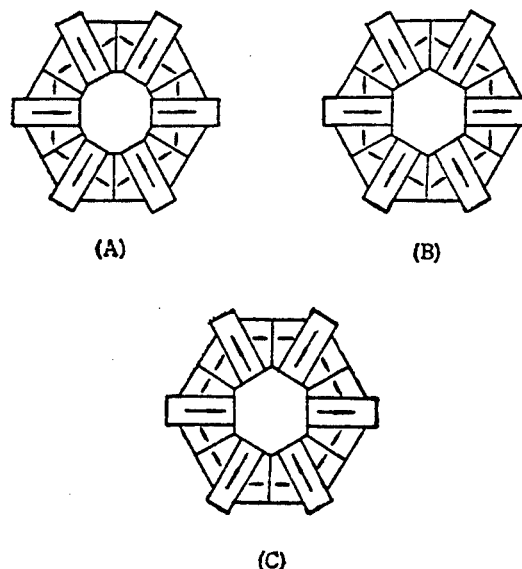


Figure 2. Three Possible Radial Permanent-Magnet Structures

shown in Figure 2. The radial magnetic field distributions of the three magnetic structures shown in Figure 2 were obtained using the PANDIRA<sup>5</sup> program. The permanent magnet chosen is made of samarium cobalt with  $B_r = 0.87$  T and  $H_c = 8.2$  kOe. The results are shown in Figure 3. Curves (1) and (2) are the magnetic field distribution at  $30^\circ$  for structures (a) and (b). Curve (3) is the magnetic field distribution at  $0^\circ$  for structures (a) and (b). Obviously, these two structures have quite different magnetic fields at different angles of orientation, which is not desirable. The field distribution of structure (c) at  $0^\circ$  is shown in Curve (4). Its magnetic field distribution at  $30^\circ$  is marked as x. Its magnetic lines of force are shown in Figure 4; due to symmetry, only 1/12 is shown. Nevertheless, the maximum field is approximately 0.7 T, which cannot meet our design requirement. In order to raise the maximum operating field strength, we used the FHLN200 permanent magnet made of neodymium-iron-boron (Nd-Fe-B) which allows us to operate at as high as  $200^\circ\text{C}$ . Its  $B_r$  is at least 1.05 T and  $H_c$  is approximately 8.5 kOe. At room temperature, the maximum hexapole magnetic field is 0.82 T. The temperature coefficient of this material is  $-0.07\%/^\circ\text{C}$ . The permanent magnet is water-cooled. The inlet temperature is  $15^\circ\text{C}$  and the outlet temperature is  $25^\circ\text{C}$ . Hence, even in the worst situation, we can ensure that the radial field is greater than 0.79 T to avoid the  $2\omega_{rf}$  enclosed surface from hitting the wall of the vacuum chamber. Thus, not only can the radial magnetic field of the structure shown in Figure 2(c) reach the design target with an Nd-Fe-B magnet, but also sufficient uniformity along various angles of orientation can be ensured.

#### IV. Computation of Axial Magnetic Field

Under the condition that magnetic excitation current is not increased, different schemes were considered to raise

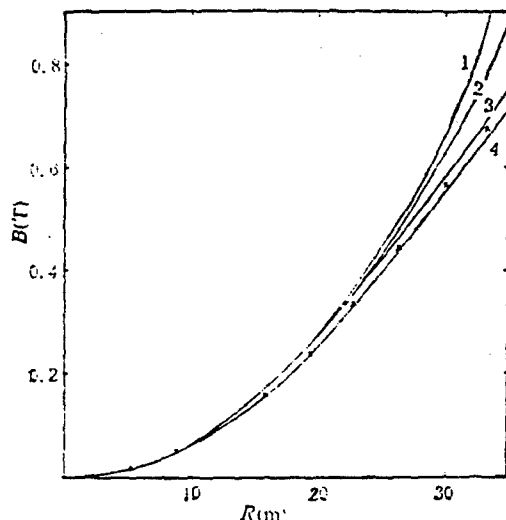


Figure 3. Radial Magnetic Field Distribution of the Three Permanent Magnets at 0° and 30°

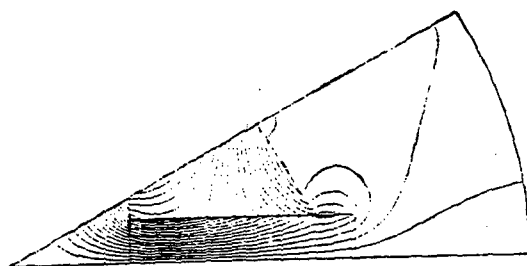


Figure 4. Magnetic Lines of Force for Structure (c)

the axial magnetic field peak without making substantial changes to the ECR source. After comparison, a 15-mm-thick soft iron ring was added near the output terminal of the coil, as shown in the shaded part of Figure 5. Three different ring shapes, i.e., wedge, rectangular and reverse wedge, were used to study the effect on the axial peak. The results show that different shapes play a minimal role on its distribution. For ease of machining, we used a ring with a rectangular top. Obviously, from Figure 6 we can see that this ring is responsible for raising the axial magnetic field from 0.65 T to 0.75 T and reducing the width of the peaks. In addition, in order to reduce the width of the magnetic field peak near the inlet to facilitate the diffusion of the cold plasma toward the second stage, we added another 10-mm-thick ring inside the other coil, as shown by the shaded area in Figure 5. The final axial magnetic field distribution is shown in Figure 6. The magnetic mirror indices are  $R_1 = 5.15$  and  $R_2 = 4.69$ . The magnetic

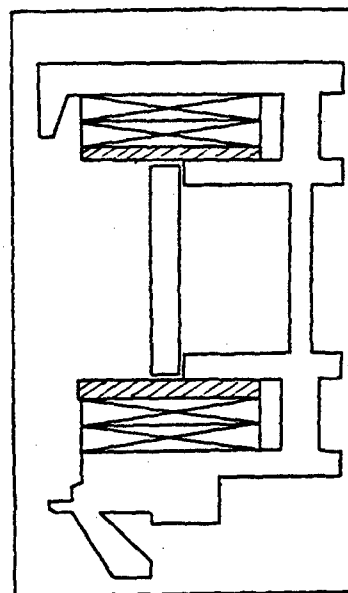


Figure 5. Insertion of Two Soft Iron Rings in ECR Ion Source

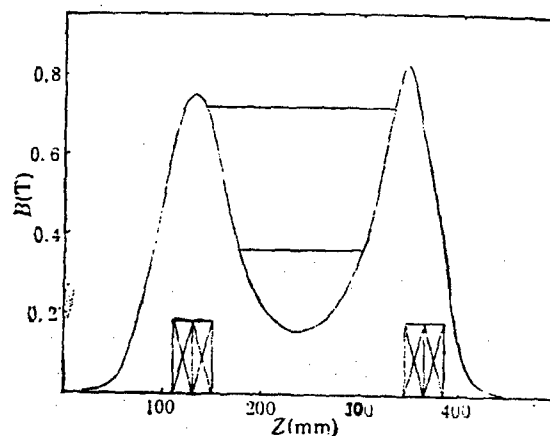


Figure 6. Axial Magnetic Field Distribution of the New ECR Ion Source

line-of-force distribution of this new structure is shown in Figure 7. Under the joint effect of the newly designed radial and axial field, the axial extension of the  $\omega_{ecr}$  surface is enlarged from 54 mm to 125 mm, and that of the  $2\omega_{rf}$  equigauss surface is 180 mm. Their profiles are shown in Figure 8. It indicates that the plasma area producing high-temperature, high-density electrons is expanded considerably. This provides the necessary condition to produce high-intensity charged ion beams. The axial field was computed using the MT-2D<sup>6</sup> and POISSON<sup>7</sup> programs and the results were cross-checked.



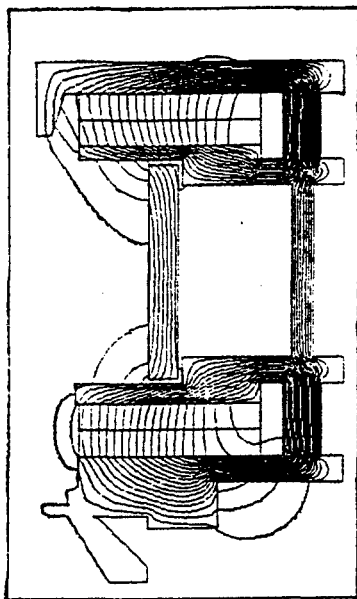


Figure 7. Magnetic Lines of Force of the New Magnet  
Structure

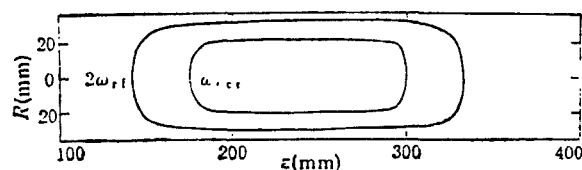


Figure 8.  $\omega_{ecr}$  Resonance Surface and  $2\omega_{rf}$  Equigauss Surface of ECR Ion Source

## V. Conclusions

Computation of an improved axial and radial magnetic field design for an ECR ion source based on the CAPRICE design shows that the axial extension of the second-stage source  $\omega_{ecr}$  resonance surface can be increased from 54 mm to 125 mm by adding 15-mm-thick and 10-mm-thick iron rings inside the two coils and modifying the radial magnet structure to raise the hexapole field from 0.4 T to 0.8 T without changing the transmission frequency. In addition, a 180-mm-wide enclosed  $2\omega_{rf}$  axial extension surface is produced. Thus, higher-intensity heavy ion beams can be produced based on this magnetic field profile.

## References

1. Liu Zhanwen, Xu Yongxing, and Wei Baowen, "Theory of the ECR Ion Source and Analysis of Its Magnetic Field," YUANZI NENG KEXUE JISHU

[ATOMIC ENERGY SCIENCE AND TECHNOLOGY], to be published.

2. F. Bourg, J. Debernardi, R. Geller, et al., Workshop on the 6th Inter. ECR Ion Source, P1, Berkeley, 1985.

3. B. Jacquot, P. Briand, F. Bourg, R. Geller, et al., Note Scientifique No. 887, CENG, DRFG-PADSI.

4. R. Geller and B. Jacquot, 7th Workshop on ECR Ion Source, p 31, Julich, 1986.

5. R. F. Holsinger, private communication, Part V, p 7.

6. Xu Yongxing and Ma Yingjie [7456 5391 2638], Chinese National Symposium on Particle Accelerators, 1979, p 377.

7. A. M. Winslow, UCRL 7784-T(1964).

## Experimental Terminal of Large Area Ionization Chamber at HIRFL Accelerator

91FE0692 Beijing GAONENG WULI YU HE WULI [HIGH-ENERGY PHYSICS AND NUCLEAR PHYSICS] in Chinese Vol 15, No 5, May 91 pp 442-449

[Article by Feng Enpu [7458 1869 2528], Zhu Yongtai [6175 3057 3141], Guo Zhongyan [6753 1813 6056], Qiao Weimin [0829 5898 3046], Zhan Wenlong [6124 2429 7893], Shen Wenqing [3088 2429 1987], Wang Xiaoqiu [3769 2556 4428], Wang Bing [3769 0014], Yin Shuzhi [1438 3219 5347], Feng Jun [7458 6511], Liu Guanhua [0491 0385 5478], Xi Hongfei [6741 3163 7378], Fan Enjie [5400 1869 2638], Zhu Xiang [4376 5046], Zhou Jianqun [0719 1696 5028], and Zeng Yuewu [2582 6460] of the Chinese Academy of Sciences Modern Physics Institute, Lanzhou: "Experiment Terminal of Large-Area Ionization Chamber at Lanzhou Heavy Ion Accelerator"; manuscript received 28 May 90]

[Text] Abstract: This article provides a general description of the large area ionization chamber experiment terminal, one of the physics experiment terminals built in conjunction with the Lanzhou Heavy Ion Accelerator. It introduces the basic structure of the experiment terminal and the detector systems with which it is configured, and it provides the results of performance tests on some of the detectors. Finally, it briefly describes a research project on moderate-energy heavy ion region reaction mechanisms now being conducted at this experiment terminal.

## I. Introduction

The Lanzhou Heavy Ion Accelerator (HIRFL) is a moderate energy region (20-100 MeV/u) heavy ion acceleration device. This is a transitional energy region between the low energy region and relativistic heavy ions. Thus, there is a transition process with certain characteristics of atomic nuclei collision behavior which exists in this energy region. In this energy region, when the acoustic velocity and Fermi energy levels of nucleons in nuclear

matter are reached or exceeded, Pauli's exclusion principle may not be observed. Because the average free path of the nucleons is shorter, nucleon-nucleon collision characteristics begin to appear, so the nuclear reaction characteristics of this energy region are not entirely atypical nor are they entirely quantum. Thus, it is neither a dissipation process of a single body nor two types of extreme circumstances of dissipation of two bodies. Moreover, the energy levels of heavy ions are not so low that their interaction can be viewed as an entirely average field effect, nor are they so high as to cause absolute dominance by individual nucleon collision behavior. From the perspective of dynamics, nuclear collision behavior begins to manifest the characteristics of fluid dynamics. Thus, this is a transitional region which displays the complexity of the reaction mechanism, meaning that it is not as simple as the deep inelastic collision processes and fusing processes of heavy ions of the low energy region, nor is it entirely like the fragmentation process in the high energy region. Thus, it can create, for example: gas-liquid phase transition phenomena in nuclear material<sup>[1]</sup>, incomplete deep inelastic collision processes<sup>[2, 3]</sup>, dissipation and fragmentation processes<sup>[4]</sup>, multiple fragmentation processes<sup>[5]</sup>, high heat and high excitation nuclear processes<sup>[6]</sup>,  $\pi$  meson emission<sup>[7]</sup>, high energy  $\gamma$  ray emission<sup>[8]</sup> area ionization chamber terminal is one of eight experiment terminals on the beam line of the Lanzhou Heavy Ion Accelerator (HIRFL) and is used to conduct research on moderate energy region heavy ion reaction mechanisms. Of course, it also can be used for research in certain aspects of nuclear structures. This article will discuss the basic structure of the large area ionization chamber experiment terminal and the basic properties of its detector system. Finally, it will provide a brief introduction to research projects now being conducted at the experiment terminal.

## II. Basic Structure of the Large Area Ionization Chamber Experiment Terminal

### A. Scattering chamber

Figure 1 is an external view of the overall structure of the large area ionization chamber experiment terminal. The cylindrical part of the structure in the middle is the terminal's scattering chamber. Figure 2 illustrates the overall configuration when the scattering chamber is connected with each of the elements and components of the terminal. The entire terminal is made of stainless steel.

The scattering chamber has an interior diameter of 1.5 m. The internal height of the cylinder itself is 760 mm. There are three beam entry tube windows on the horizontal plane of the scattering chamber beam that can be used to change the included angle between the scattering chamber and the beam to 0°, 12°, and 20°. There is a square window with a horizontal field angle of 45° to the front of the scattering chamber to enable connection with the detector system and flying time measurement tube at the front. Thus, it can be adapted to the small

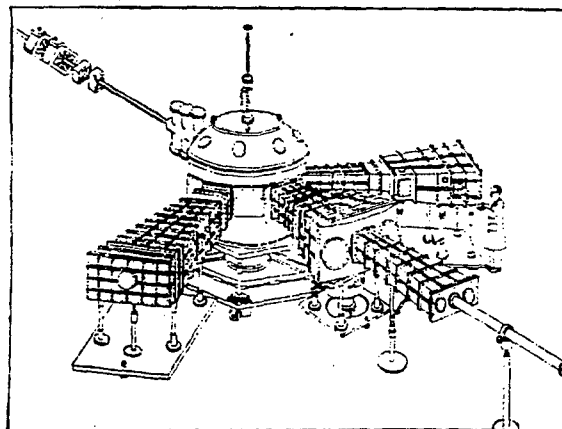


Figure 1. External View of the Overall Structure of the Large Area Ionization Chamber Experiment Terminal

rubbing edge angle and concentration of products in a pyramid in a frontal direction that characterize moderate energy region heavy ion reactions. There are also 12 square windows that can be opened around the scattering chamber (Figures 1 and 2). Each of the windows is level with the target and all have a field angle of 19° to satisfy the requirements for installing externally connected detectors at different angle locations. In addition, the detector signal outputs, high voltage supply, detector working gas circulation loops, cooling water channels, and so on can pass through flanges on the square windows. The outer bottom of the scattering chamber has a air potential trough that can use compressed air to lift the scattering chamber itself upward to rotate it to the desired angle.

At the center of the flat part of the crown-shaped top cap of the scattering chamber, the target rod and target installation system with a vacuum sealing tube is installed (Figure 1). A target holder on which the target is placed is connected to the target rod. The target rod can be shifted up and down at the top of the scattering chamber to change the position of the target. The target rod can also be rotated along 360° around its axis to change the normal direction included angle of the target to the beam.

The top cap of the scattering chamber is a "rotating curved surface". It has eight round windows aligned with the target position on it. The windows are 130 mm in diameter (Figure 1). The  $\gamma$  ray detectors pass through the vacuum isolation drum. They can extend from the outside into the space near the targets without destroying the vacuum state of the scattering chamber.

On the internal bottom plate of the scattering chamber, there is a 1.3 m diameter rotating disk (Figure 2). Detectors can be installed at different angles and different radial distances as required. The rotating disk can be rotated plus or minus 180° to the direction of the

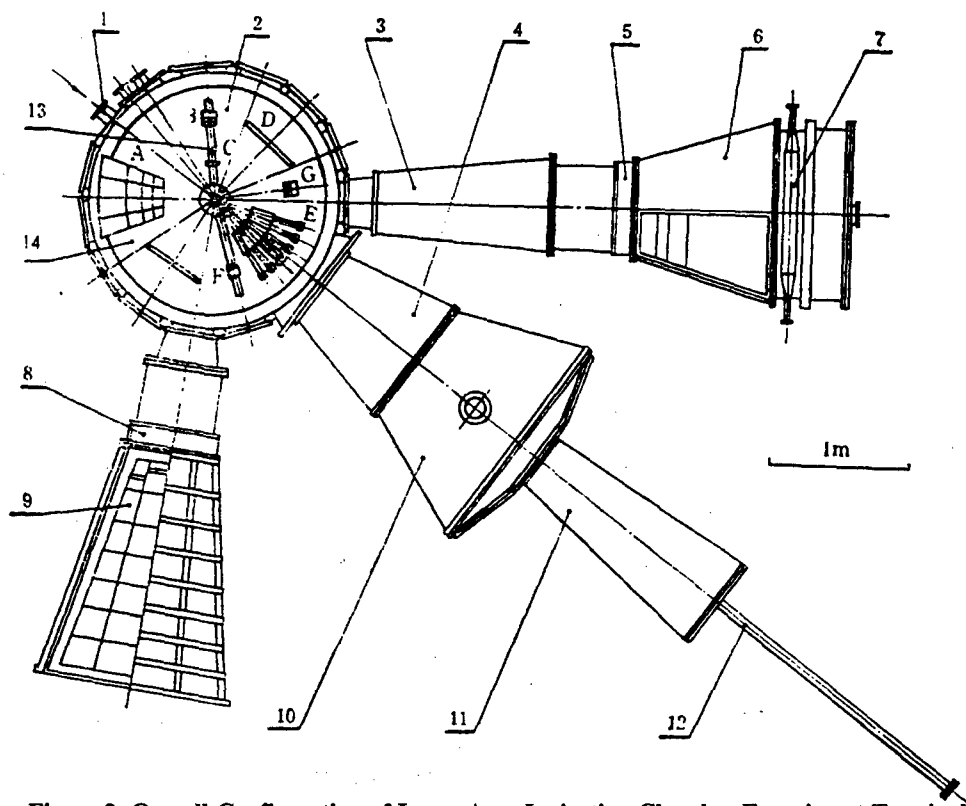


**Figure 2. Overall Configuration of Large Area Ionization Chamber Experiment Terminal**

Key: 1. Beam entrance; 2. Rotating disk; 3. Drift tube; 4. Drift tube; 5. Parallel plate avalanche chamber; 6. 80 cm large ionization chamber; 7. Plastic scintillator detector tracer; 8. Parallel plate avalanche chamber; 9. 140 cm large ionization chamber; 10. Drift tube; 11. Drift tube; 12. Faraday tube; 13. Rotating arm; 14. Outgoing window A. 35 cm ionization chamber; B. Semiconductor detector telescope; C. Microchannel plate detector; D. PPAC detector; E. Phoswich detector array; F. CsI (TI) detector; G. Semiconductor detector telescope

beam. There are two rotating walls installed above the rotating disk coaxial with the rotating disk (Figure 2). The walls are both 60 cm long and are also used for installing the detectors. Two stepping electric motors are used to turn the rotating walls and a computer is used to control the rotation angle. The rotation angle precision is  $0.1^\circ$ .

#### B. Drift tubes

Conical drift tubes with horizontal field angles of plus or minus  $12^\circ$  or plus or minus  $22.5^\circ$  can be connected to the square window at the front of the scattering chamber. The plus or minus  $22.5^\circ$  drift tube can also be connected in series behind the plus or minus  $12^\circ$  conical chamber (Figures 1 and 2). It has three round windows 35 cm in diameter in its back side and 1.36 m conical drift tubes can be connected to the windows (Figures 1 and 2). This makes the total length from the end of the tubes to the target 3.9 m. A 2.5 m long Faraday tube pipe is connected to the end of the drift tubes.

On the left side of the scattering chamber, there is another drift tube with a total length of 2.4 m from its

end to the target. At the back of it, the large area ionization chamber detector system can be connected (Figures 1 and 2).

#### C. Air extraction system and vacuum measurement system

The air extraction system includes one turbomolecular pump with an extraction speed of 3,500 L/s and two with extraction speeds of 1,500 L/s. There is also a cooling pump below the  $45^\circ$  conical zero degree chamber. The low vacuum air extraction is done by the HIRFL post-experiment public pre-evacuation machine unit. To date, the vacuum of the terminal has reached  $1.8 \times 10^{-6}$  mbar. The vacuum measurement system uses a digital "(pilani)" cold cathode for vacuum measurement. It can display vacuums from atmospheric pressure to  $10^{-10}$  mbar numerical grades.

#### III. Large Area Ionization Chamber Terminal Detector System

The terminal is configured with several types of detector telescopes for use in experimental research on moderate energy heavy ion reaction mechanisms. A description of them follows:

#### A. Avalanche chamber + 80 cm large ionization chamber + scintillator detector

This terminal will continue using an 80 cm deep large area position sensitive ionization chamber that was developed in 1980<sup>[9]</sup>. We used it in the 1.5 m cyclotron to do a series of low energy region heavy ion reaction mechanism experiment studies, such as a study on light system deep inelastic collision mechanisms<sup>[10-14]</sup>. When it was installed on this experiment terminal, it had a solid angle extending 7.7 msr to the target. Under low energy heavy ion conditions, the charge resolution obtained was  $Z/\Delta Z = 27$ <sup>[9]</sup>. When 800 mbar barometric Ar gas was used, the effective thickness of the ionization chamber was 105 mg/cm<sup>2</sup>. For example, for 50 MeV/u  $\alpha$  particles, it could only block the energy of 7 MeV/u  $\alpha$  particles and was incapable of detecting the total energy of the particles. As a result, a plastic scintillator (NE 102A) detector was installed behind the ionization chamber to serve as a detector to prevent high energy heavy ions from penetrating the ionization chamber. At the same time, it also provided position information<sup>[15]</sup>. This plastic scintillator was designed to have a long shape (760 mm long X 98 mm high, with two types, 27 mm and 88 mm thick, installed at the top and bottom). The structure is shown in Figure 2. The energy signals and position signals were read at the two ends of the scintillator. A light guide between the scintillator and photomultiplier tube (XP2020Q) also served as a vacuum seal. Because the upper and lower scintillators each corresponded to the upper and lower parts of the ionization chamber, they formed two independent  $\Delta E$ -E detector systems that could be used to block  $\alpha$  particle energies of nearly 60 MeV/u and greater than 100 MeV/u. In addition, for heavier outgoing products, the original ionization chamber was divided into four-stage electrodes that still formed independent  $\Delta E$ -E detectors. This expanded the dynamic range of the entire detector system. An  $\alpha$  source (8.78 MeV) was used to determine that the position resolution measured by the scintillator was 6 cm and the corresponding angle resolution was 1°.

To conduct time measurements, a parallel plate avalanche chamber (PPAC) was also installed at the front end of the ionization chamber's incoming windows (400 mm X 60 mm X 2)<sup>[16]</sup>. Its active area was 60 X 400 mm<sup>2</sup> and the electrode spacing was 2 mm. When using regular heptane gas, selecting a working voltage of 630 V, and using a position sensitive avalanche chamber to provide start time signals, it was possible to measure the resolution time of this PPAC itself at 250 ps.

#### B. Parallel plate avalanche chamber + 1.4 m large ionization chamber

The 1.4 m large ionization chamber<sup>[17]</sup> is another large detector used with this terminal. Its structure is illustrated in Figures 2 and 3. This ionization chamber is divided into independent upper and lower layers and each of the layers forms an ionization chamber. There is a Frisch grid 30 mm from the anode plate (A). The area of the incoming windows of the ionization chamber was

396 mm X 60 mm X 2. The horizontal field angle to the target was 19°. The solid angle formed was 33 msr. To increase the total permissible counting rate of the detector and make proper measurements in the same ionization chamber, the anode plate was divided into four angle regions within the full range of the field angle. Each region was divided into six parts along the radial direction  $\alpha$  (Figure 3) to adapt to the detection of different energies and different types of charged particles. Thus, it was actually equivalent to eight independent ionization chamber elements.

To make position measurements and flying time measurements, a penetrating parallel plate avalanche chamber (PPAC) was installed at the front end of the 1.4 m ionization chamber<sup>[18]</sup>. Its electrode plates are divided into eight independent elements corresponding to the eight elements of the 1.4 m ionization chamber. The spacing between their cathodes and anodes is 3 mm. When the working voltage is set at 490 V, the isobutylene gas and <sup>252</sup>Cf fission sources used for measurement gave resolution times of 300 ps and position resolution of 2 mm.

#### C. 35 cm ionization chamber

To measure heavier and lower energy outgoing particles at the rear angle site, a 35 cm deep ionization chamber can be installed on the large rotating disk of the scattering chamber<sup>[19]</sup>. The incoming window of the ionization chamber has an area of 24 X 5 cm<sup>2</sup>, a target distance of 30 cm, and a horizontal field angle of 40° to the target, to form a solid angle of 1.3 msr. The distance between the cathode plate and the Frisch grid is 116 mm and the distance between the anode plate and the Frisch grid is 30 mm. To expand the dynamic range of the measurements, the anode plate is divided into four elements along the radial direction. To make particle alignment measurements in the same ionization chamber, the anode plate is divided into four angle regions along the direction of the  $\theta$  angle. The total energy resolution measured by the three electrodes is 1.5 percent. The position resolution in the vertical direction is 3.6 mm.

#### D. Position sensitive dual-grid avalanche chamber

To measure heavier outgoing fragments in the scattering chamber, the position and flying time of heavy fragments can be measured. The position resolution along the X and Y axes is 4 mm<sup>[20]</sup>. These probes together with the 1.4 m ionization chamber and 35 cm ionization chamber were developed by the Modern Physics Institute's Gas Detector Development Group.

#### E. Optical laminated detector array

To measure light particles, a new type of circular optical laminated detector array was developed<sup>[21]</sup>. It is composed of 36 elements. It is placed on the rotating disk inside the scattering chamber and has a horizontal field angle range of 5° to 20° to the target, an output horizontal azimuth of 0° to 360°, and a solid angle extending 0.345 sr. This array is divided into three layers along the  $\theta$

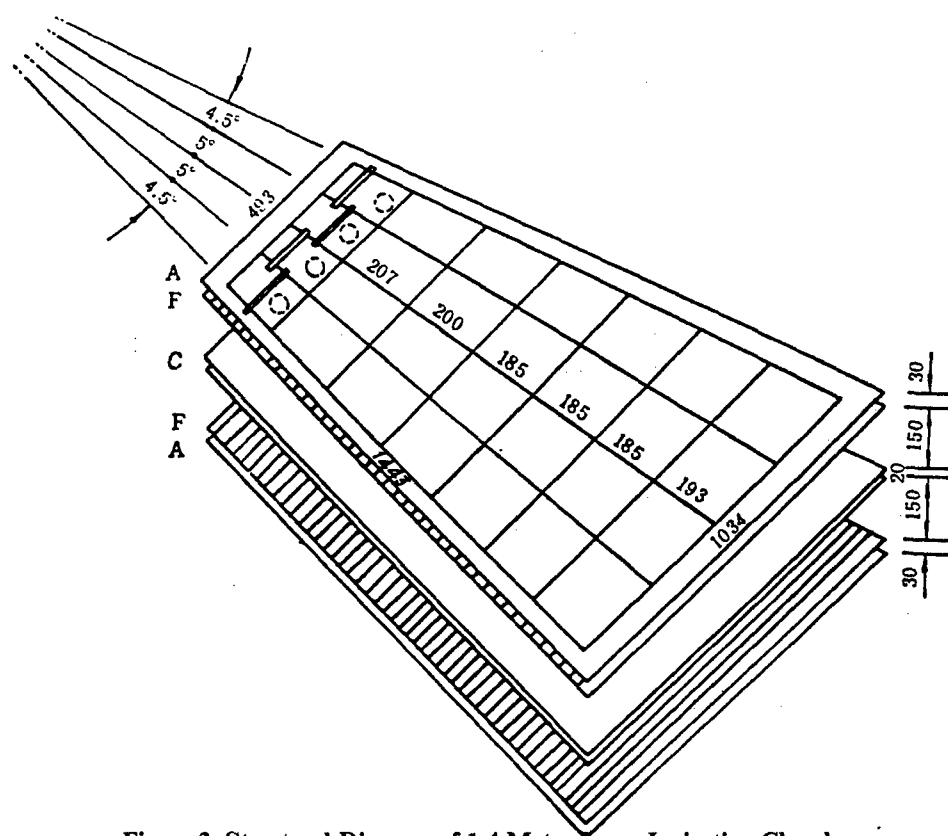


Figure 3. Structural Diagram of 1.4 Meter Large Ionization Chamber

direction and the azimuth  $\phi$  is divided into 12 elements to form a circular structure. Its structure is illustrated in Figure 4. Each element is a  $\Delta E$ -E telescope composed of a 0.7 mm thick rapid plastic scintillator (ST1421), 100 mm thick slow plastic scintillator (NE115), and HAMAMATSU-R1666 photomultiplier tube used to provide the signals. Because of the large difference in the photo decay times of the two types of plastic scintillators, using 2.7 ns and 270 ns scintillators permits selection of gate circuits with different time widths for gating integration of the fast and slow components of the light. Because there are different ratios of the fast and slow components generated by different types of charged particles which have identical energies, particle identification is possible. See reference [22] concerning the question of using plastic scintillator detectors in heavy ion physics. In the HIRFL accelerator, a 46 MeV/u  $^{12}\text{C}$  beam is used to bombard the nuclear reaction generated by the  $^{197}\text{Au}$  target. The charge resolution two-dimensional spectrum measured by the elements in this array is shown in Figure 5. The vertical coordinate in the graph is the light output of the fast components and the horizontal coordinate is the total light output. In it, the fast gate was chosen at 50 ns and the slow gate was chosen at 700 ns. It is apparent that there was rather good resolution of the outgoing products from the protons to the  $^{12}\text{C}$ .

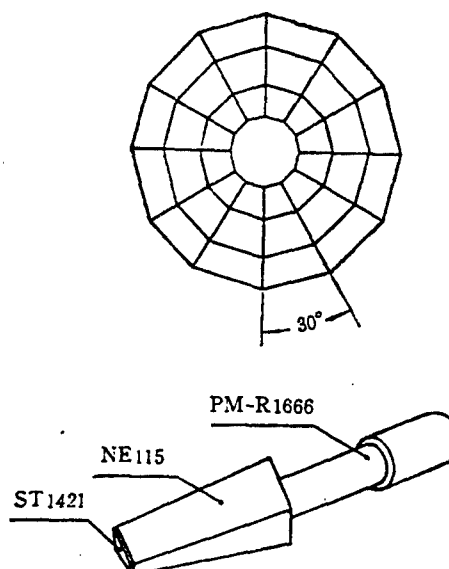


Figure 4. Structural Diagram of Optical Laminated Detector Array

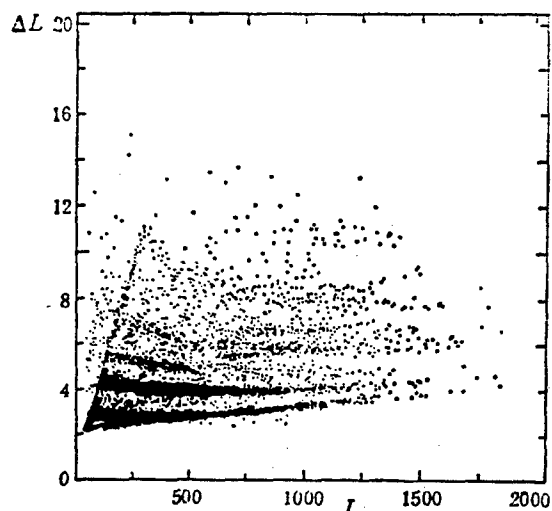


Figure 5. Two-Dimensional Spectra of Optical Laminated Detector Charge Resolution

#### F. Other detectors

Besides the various detectors described above, we also developed a telescope system<sup>[23]</sup> using a semiconductor surface-barrier  $\Delta E$  detector and a CsI crystal used as a blocking detector to detect high-penetration products, a  $\Delta E$  detector using an ionization chamber, and a telescope using a scintillator as an E detector<sup>[24]</sup>. In addition, we used a surface-barrier semiconductor telescope with good energy resolution properties to make several telescopes for use in experiments.

#### IV. Research Done at This Terminal

At present, the physics work we have done at this terminal has mainly involved research on moderate energy heavy ion reaction mechanisms.

##### A. Research on heavy ion incomplete depth inelastic collisions

This is a new reaction mechanism. It is different from deep inelastic collision mechanisms in that, after excitation, the bullet can be emitted in a forward direction along with a light particle having a velocity approximately that of the bullet and a dissipation collision reoccurs between the residual portion of the bullet and the target nucleus.

##### B. Research on heavy ion induced deep inelastic fragmentation

This is another prospective new reaction mechanism. It is different from the reaction mechanism described above in that the bullet and the target nucleus undergo a dissipation process to form a very hot nuclear matter group in a high excitation state. The subsequent process

is approximately the same as the "fireball" model generated by relativistic heavy ions and can be called a "participation ball". The "participation ball" can again undergo fragmentation (or splitting) and thereby become de-excited. Thus, it is called a dissipation fragmentation process.

##### C. Research on complex particles emitted in heavy ion reactions

Moderate energy ions used as a transitional zone between low energy and high energy heavy ions can cause changes in several reaction mechanisms, such as liquid-gaseous phase changes in nuclear matter and other phenomena. Thus, research on outgoing particles with charge numbers below 10-plus can provide information in this area. Preliminary experiments in this research project have already been completed and the data are now being processed.

##### D. Measurement of neutron-rich bullet reaction total cross sections

Data on neutron-rich bullet reaction total cross sections provides important information for research on moderate energy heavy ion nuclear reaction mechanisms. Neutron-rich bullets usually cannot be created directly in accelerators. They must be created using nuclear reaction methods and obtained by selecting them using a magnetic analysis system and then inserting them into the scattering chamber of this terminal to conduct experiments.

##### E. Other experiments

At present, we have already completed our first cooperative experiment with an outside unit at this terminal. This was a combined linear momentum transfer and light particle emission experiment conducted cooperatively by the Beijing University Technical Physics Department Experiment Group and the First Group of the Second Office at the Modern Physics Institute. The data are now being processed.

#### V. Conclusion

The construction and completion of this terminal is the outcome of substantial assistance from the First Conditions Office and Second Conditions Office of the Modern Physics Institute and various departments and offices under the jurisdiction of the 7611 Engineering Institute. Processing of the machinery in the main part of this terminal was done by the Minhang Branch of the Shanghai Municipality Machine-Building and Electronics Employees Technological Association. I would like to express my gratitude to the branch's Shanghai Boiler Plant Trade Union Employees Technological Association, Shanghai Heavy Machinery Plant Trade Union Employees Technological Association, Shanghai Machine-Building and Electronics Equipment Set Research Institute, Shanghai Electric Motor Plant Trade Union Employees Technological Association, and other units.

## References

- [1] A. D. Panagiotou et al., Phys. Rev. Lett., V52, 1984 p 496.
- [2] F. Guzman Martinez et al., Nucl. Phys., A436, 1985 p 294.
- [3] Zhu Yongtai et al., Nucl. Phys., A488, 1988 p 409c.
- [4] B. Borderie, XVII Masurian School on Nuclear Physics, "Trends in Nuclear Physics", Mikolajki, Sept. 2-14, 1985.
- [5] J. P. Bondorf, Nucl. Phys., A387, 1982 p 25c.
- [6] J. Gosset et al., Phys. Rev., C16, 1977 p 629.
- [7] E. Grosse, Int. Conf. on Nucl. Phys. Hvar, ed. N. Cindro, 1984.
- [8] N. Nerrman et al., G.S.I. Scientific Report, 1985 p 86.
- [9] Shen Wenqing [3088 2429 1987] et al., Gaoneng Wuli Yu He Wuli [High Energy Physics and Nuclear Physics], vol 7, 1983 p 500.
- [10] Shen Wenqing et al., Gaoneng Wuli Yu He Wuli, vol 9, 1985 p 332.
- [11] Zhu Yongtai [6175 3057 3141] et al., Gaoneng Wuli Yu He Wuli, vol 9, 1985 p 447.
- [12] Zhan Wenlong [6124 2429 7893] et al., Gaoneng Wuli Yu He Wuli, vol 10, 1986 p 63.
- [13] Yin Shuzhi [1438 3219 5347] et al., Gaoneng Wuli Yu He Wuli, vol 11, 1987 p 259.
- [14] Guo Zhongyan [6753 1813 6056] et al., Gaoneng Wuli Yu He Wuli, vol 11, 1987 p 496.
- [15] Liu Guanhua [0491 0385 5478] et al., Zhongguo Kexueyuan Jindai Wuli Yanjiusuo Nianbao [Annual Report of the Chinese Academy of Sciences Modern Physics Institute], 1989.
- [16] Zhan Wenlong et al., Gaoneng Wuli Yu He Wuli, vol 12, 1988 p 85.
- [17] Tan Jilian [6223 4949 1670] et al., "Large Area Multi-Parameter Ionization Chamber", Gaoneng Wuli Yu He Wuli, to be published.
- [18] Fan Enjie [5400 1869 2638] et al., "One-Dimensional Position Sensitive Eight-Element PPAC", Gaoneng Wuli Yu He Wuli, to be published.
- [19] Zhu Xiang [4376 5046] et al., "Multi-Parameter Large-Area Ionization Chamber", Master's thesis.
- [20] Tan Jilian et al., He Jishu [Nuclear Technology], vol 12, 1989 p 323.
- [21] Wang Bing [3769 0014] et al., "Optical Laminated Plastic Scintillator Detector Array", Gaoneng Wuli Yu He Wuli, to be published.
- [22] Wang Bing et al., He Wuli Dongtai [Nuclear Physics Trends], No 4, 1987 p 11.
- [23] Xi Hongfei [6741 3163 7378] et al., "A Light Charged Particle Detector Using a CsI(Tl) Crystal Coupled To an Optical Diode Readout", He Jishu, to be published.
- [24] Wang Bing et al., "A Scintillator Detector Telescope Fitted with an Ionization Chamber", He Jishu, to be published.

This project received some support as a Chinese Academy of Sciences Key Project and State Natural Sciences Foundation Key Project.

NTIS  
ATTN PROCESS 103

2

5285 PORT ROYAL RD  
SPRINGFIELD VA

22161

This is a U.S. Government publication. Its contents in no way represent the policies, views, or attitudes of the U.S. Government. Users of this publication may cite FBIS or JPRS provided they do so in a manner clearly identifying them as the secondary source.

Foreign Broadcast Information Service (FBIS) and Joint Publications Research Service (JPRS) publications contain political, military, economic, environmental, and sociological news, commentary, and other information, as well as scientific and technical data and reports. All information has been obtained from foreign radio and television broadcasts, news agency transmissions, newspapers, books, and periodicals. Items generally are processed from the first or best available sources. It should not be inferred that they have been disseminated only in the medium, in the language, or to the area indicated. Items from foreign language sources are translated; those from English-language sources are transcribed. Except for excluding certain diacritics, FBIS renders personal and place-names in accordance with the romanization systems approved for U.S. Government publications by the U.S. Board of Geographic Names.

Headlines, editorial reports, and material enclosed in brackets [ ] are supplied by FBIS/JPRS. Processing indicators such as [Text] or [Excerpts] in the first line of each item indicate how the information was processed from the original. Unfamiliar names rendered phonetically are enclosed in parentheses. Words or names preceded by a question mark and enclosed in parentheses were not clear from the original source but have been supplied as appropriate to the context. Other unattributed parenthetical notes within the body of an item originate with the source. Times within items are as given by the source. Passages in boldface or italics are as published.

#### SUBSCRIPTION/PROCUREMENT INFORMATION

The FBIS DAILY REPORT contains current news and information and is published Monday through Friday in eight volumes: China, East Europe, Soviet Union, East Asia, Near East & South Asia, Sub-Saharan Africa, Latin America, and West Europe. Supplements to the DAILY REPORTs may also be available periodically and will be distributed to regular DAILY REPORT subscribers. JPRS publications, which include approximately 50 regional, worldwide, and topical reports, generally contain less time-sensitive information and are published periodically.

Current DAILY REPORTs and JPRS publications are listed in *Government Reports Announcements* issued semimonthly by the National Technical Information Service (NTIS), 5285 Port Royal Road, Springfield, Virginia 22161 and the *Monthly Catalog of U.S. Government Publications* issued by the Superintendent of Documents, U.S. Government Printing Office, Washington, D.C. 20402.

The public may subscribe to either hardcover or microfiche versions of the DAILY REPORTs and JPRS publications through NTIS at the above address or by calling (703) 487-4630. Subscription rates will be

provided by NTIS upon request. Subscriptions are available outside the United States from NTIS or appointed foreign dealers. New subscribers should expect a 30-day delay in receipt of the first issue.

U.S. Government offices may obtain subscriptions to the DAILY REPORTs or JPRS publications (hardcover or microfiche) at no charge through their sponsoring organizations. For additional information or assistance, call FBIS, (202) 338-6735, or write to P.O. Box 2604, Washington, D.C. 20013. Department of Defense consumers are required to submit requests through appropriate command validation channels to DIA, RTS-2C, Washington, D.C. 20301. (Telephone: (202) 373-3771, Autovon: 243-3771.)

Back issues or single copies of the DAILY REPORTs and JPRS publications are not available. Both the DAILY REPORTs and the JPRS publications are on file for public reference at the Library of Congress and at many Federal Depository Libraries. Reference copies may also be seen at many public and university libraries throughout the United States.